Charles University in Prague
Faculty of Mathematics and Physics

DOCTORAL THESIS

Volodymyr Skoromets

Tunable materials and structures for terahertz spectral range

Institute of Physics
Academy of Sciences of the Czech Republic

Supervisor: RNDr. Petr Kužel, Dr.

Study programme: Physics
Specialization: Condensed Matter and Material Research

Prague 2013

Acknowledgment

There are many people to whom I wish to express my gratitude for their help and encouragements during the preparation of this thesis.

In the first place I would like to express my deepest gratitude to my supervisor Petr Kužel for his patient guidance, encouragement and brilliant ideas. Everything I know about the time-domain terahertz spectroscopy I have learnt from him. He also greatly contributed to my understanding of the ferroelectric phenomena. He has always been a driving force and a source of inspiration for me. Moreover, I am grateful to him for a critical reading of the present manuscript, which resulted in a great improvement of the thesis.

It is my pleasure to thank my consultant Stanislav Kamba who introduced me to the Fourier transform infrared spectroscopy and was always open for discussions. Also I appreciate the help of Veronica Goian with the infrared experiments lasting till midnight. I wish to thank Dmitry Nuzhnyy for the infrared measurements on $KTaO_3$ ceramics which are included in the thesis.

I am very grateful to Christelle and Filip Kadlec and Hynek Němec, who form the stem of Laboratory of Terahertz Spectroscopy. They have always been ready to help with everything I needed. I would like to thank all the colleagues from the Department of the Dielectrics for the friendly and cheerful atmosphere that make my stay in Prague more pleasant.

I am indebted to Jürgen Schubert (Jülich, Germany) for the preparation of the whole set of the thin film $SrTiO_3/DyScO_3$ heterostructures. I would like also to thank Gregor Panaitov (Jülich, Germany) who deposited the interdigitated metallic electrode structures onto these multilayered samples.

The investigation of an electric-field dielectric tunability of $SrTiO_3$ single crystals would not be complete without the nanocrystalline SnO_2 thin-film electrodes transparent for the THz radiation, therefore, I am indebted to Dina Fattakhova-Rohlfing (Munich, Germany) for this idea and for the help with the electrodes preparation. I would like also to thank Viktor Bovtun and Martin Kempa for the microwave measurements presented in the thesis.

I wish to thank my parents and my wife for their understanding of my intentions and for their emotional support. Many thanks also to my brother for his encouragement all the time since the moment I started to think about the PhD study in Prague and for his engineering ideas employed in the terahertz laboratory.

Finally, I would like to acknowledge financial support by the Czech Science Foundation (project 202/09/H041) and by Charles university in Prague (grant SVV-2011-263303).

I declare that I carried out this doctoral thesis independently, and only with the cited sources, literature and other professional sources.

I understand that my work relates to the rights and obligations under the Act No. 121/2000 Coll., the Copyright Act, as amended, in particular the fact that the Charles University in Prague has the right to conclude a license agreement on the use of this work as a school work pursuant to Section 60 paragraph 1 of the Copyright Act.

Prague, 25 March 2013 Volodymyr Skoromets

Název práce: Laditelné materiály a struktury pro terahertzovou spectrální oblast

Autor: Volodymyr Skoromets

Ústav: Fyzikální ústav Akademie věd České republiky

Vedoucí disertační práce: RNDr. Petr Kužel, PhD, Fyzikální ústav Akademie věd České republiky

Abstrakt: Práce se zabývá experimentálním studiem dielektrických vlastností incipientních feroelektrik. K měření spekter komplexní permitivity monokrystalů i napnutých tenkých vrstev jsme použili terahertzovou spektroskopii v časové oblasti. Stanovením závislostí spekter na teplotě a na přiloženém elektrickém poli jsme popsali dynamiku feroelektrického měkkého módu a jeho vazbu s centrálním módem.

Jako první jsme charakterizovali laditelnost dielektrických vlastností monokrystalů $SrTiO_3$ v elektrickém poli až k pokojové teplotě. Pozorované chování je způsobeno “tvrdnutím” měkkého módu ve vnějším elektrickém poli. Jako možnou aplikaci těchto vlastností jsme navrhli a vyzkoušeli laditelný jednodimenzionální fotonický krystal obsahující destičku $SrTiO_3$ jakožto defekt periodické struktury. Důležitost dynamiky měkkého módu byla také potvrzena studiem keramik $KTaO_3$ s vysokou hustotou.

Provedli jsme systematické studium tenké vrstvy $KTaO_3$ a zejména pak řady napnutých mnohovrstevných struktur složených z dvojvrstev $SrTiO_3/DyScO_3$ na podložce $DyScO_3$. V těchto vzorcích jsme pozorovali feroelektrický fázový přechod vyvolaný mechanickým napětím vrstev, který je řízen měkkým módem s vazbou na nízkofrekvenční relaxaci. Navrhli jsme obecný model, který velmi dobře popisuje dielektrické chování celé rodiny zkoumaných vzorků. V práci jsme též diskutovali vliv stechiometrie vrstev $SrTiO_3$ na jejich dielektrické vlastnosti.

Klíčová slova: terahertzová spektroskopie, feroelektrika, měkký mód, tenké vrstvy, dielektrické vlastnosti, laditelnost, fázový přechod

Title: Tunable materials and structures for terahertz spectral range

Author: Volodymyr Skoromets

Institute: Institute of Physics, Academy of Sciences of the Czech republic

Supervisor: RNDr. Petr Kužel, PhD, Institute of Physics, Academy of Sciences of the Czech republic

Abstract: This thesis is devoted to an experimental study of dielectric properties of incipient ferroelectrics. The terahertz time-domain spectroscopy was used to investigate the complex permittivity spectra in both single crystals and various strained thin film structures versus temperature and applied electric bias. Namely, it allowed characterizing the ferroelectric soft-mode dynamics and its coupling to a central mode.

An electric-field tunability of bulk single crystals of $SrTiO_3$ was determined up to room temperature for the first time. The phenomenon is governed by soft-mode stiffening under applied field. As an application we proposed and characterized a tunable one-dimensional photonic structure with a thin $SrTiO_3$ plate inserted as a defect layer. The importance of the soft-mode dynamics was stressed also in the study of bulk high density $KTaO_3$ ceramics.

A systematic study was performed of a $KTaO_3$ thin film and especially of a set of strained multilayers consisting of $SrTiO_3/DyScO_3$ bilayers grown on $DyScO_3$ substrate. Strain-induced ferroelectric transition was observed in these films governed by the soft mode coupled to a lower-frequency relaxation. A general model was developed describing the whole family of the studied samples. Effect of the composition stoichiometry of $SrTiO_3$ films grown on $DyScO_3$ was also investigated.

Keywords: terahertz spectroscopy, ferroelectrics, soft mode, thin films, dielectric properties, tunability, phase transition

Contents

1 **Overview** **1**

1.1 Ferroelectric materials 1
  1.1.1 Ferroelectric phase transition 2
  1.1.2 Critical dynamics near the ferroelectric phase transition 5
  1.1.3 Simple perovskite oxides 7

1.2 Tunability of dielectric properties 9
  1.2.1 Tunable properties of semiconductors 9
  1.2.2 Tunable properties of ferroelectrics 11
    Dielectric losses in ferroelectrics 13
    Materials for tunable applications 15
  1.2.3 Tunable properties of resonant structures 16
    Metamaterials 16
    Photonic crystals 21

2 **Experimental techniques** **25**

2.1 Time-domain terahertz spectroscopy 25
  2.1.1 Terahertz radiation 25
  2.1.2 Generation of terahertz radiation 27
    Photoconductive switch 28
  2.1.3 Detection principles 30
    Electro-optic sampling 31
  2.1.4 Time-domain THz spectroscopy 33
  2.1.5 Data analysis 36
    Plane-parallel slabs 37
    Thin films 39
    Thin films in electric field 39
    Experimental errors 39

2.2 Fourier transform infrared spectroscopy 41

2.2.1 Data analysis 43

3 Results on bulk materials **45**

Incipient ferroelectrics 45

KTaO$_3$ single crystals 45

3.1 KTaO$_3$ ceramics 46

3.1.1 Sample preparation 47

3.1.2 Results and discussion 47

3.1.3 Summary 50

3.2 Tunable dielectric properties of SrTiO$_3$ 51

3.2.1 SrTiO$_3$ single crystals 51

3.2.2 Theoretical background 52

3.2.3 Experimental details 56

3.2.4 Results and discussion 60

Perpendicular geometry 62

Parallel geometry 64

Nonlinear potential 65

3.2.5 Summary 66

3.3 Tunable photonic crystal 67

3.3.1 Structure specification 68

3.3.2 Characterization and discussion 68

3.3.3 Summary 72

3.4 Conclusions 72

4 Results on thin films **75**

Thin films of incipient ferroelectrics 75

4.1 SrTiO$_3$ films on DyScO$_3$: from single layer to heterostructures 76

4.1.1 Sample preparation and experimental issues 76

4.1.2 Experimental results 78

4.1.3 Complete analysis and discussion 82

Modeling of the dielectric response 82

Results of fits 84

Discussion 86

Repeatability of results in multilayer structures 92

Dynamic tunability 93

4.1.4 Summary 94

4.2 Impact of composition stoichiometry on the dielectric properties of $SrTiO_3$ films . . . 96
4.2.1 Samples . . . 96
4.2.2 Dielectric measurements and discussion . . . 97
4.2.3 Summary . . . 101

4.3 Ferroelectric phase transition in $KTaO_3$ film . . . 102
4.3.1 Film preparation . . . 102
4.3.2 Spectroscopic results and discussion . . . 103
4.3.3 Summary . . . 105

4.4 Tuning of hard polar phonons in $SrTiO_3$ films . . . 106
4.4.1 Experimental issues . . . 106
4.4.2 Results and discussion . . . 107
4.4.3 Summary . . . 111

4.5 Conclusions . . . 111

5 Conclusions and outlooks **113**

Bibliography **117**

List of acronyms **137**

Chapter 1

Overview

1.1 Ferroelectric materials

Dielectrics possessing a spontaneous electric dipole moment whose orientation can be switched between equivalent states by an external electric field form a group of ferroelectrics. The dependence of macroscopic polarization on the electric field is usually nonlinear and presents a hysteresis loop (Fig. 1.1) similar to the magnetic hysteresis loop for ferromagnetic materials. The loop is frequently assumed to be the characteristic feature of ferrolectricity. In addition, ferroelectrics are usually characterized by a large permittivity value [1, 2]. In fact the permittivity peaks at the so-called ferroelectric phase transition (PT). The high-temperature paraelectric phase exhibits a higher symmetry while below the PT temperature a symmetry break occurs which allows the ferroelectric order to set in.

Historically, the first ferroelectric material was discovered by Valasek in 1920 [3]; it was sodium potassium tartrate tetrahydrate ($NaKC_4H_4O_6{\cdot}4H_2O$), known as Rochelle salt. Subsequently, the first series of ferroelectric crystals was produced by Busch and Sherrer in 1935 [4] which included crystals with hydrogen bonds. Potassium dihydrogen phosphate KH_2PO_4 is probably the most studied representative of this series. At that time, it was thought that the presence of hydrogen bonds was a necessary condition for a material to show the ferroelectric properties. Aproximately ten years later barium titanate $BaTiO_3$ ceramic was revealed by Wul and Goldman [5] to exhibit the ferroelectric properties. This discovery launched a search for other similar oxide compounds with the ferroelectric properties and soon ferroelectricity was demonstrated in $KNbO_3$ and $KTaO_3$ [6], $LiNbO_3$ and $LiTaO_3$ [7], and in $PbTiO_3$ [8]. These ferroelectrics show more than one ferroelectric phase. A very frequent crystal structure of the paraelectric phase (typical for these oxide compounds) is cubic centrosymmetric perovskite with five atoms per unit cell. The relative simplicity of the unit cell favoured development of the theory of ferroelectric instability. In addition, such materials are chemically and mechanically very stable and they can be

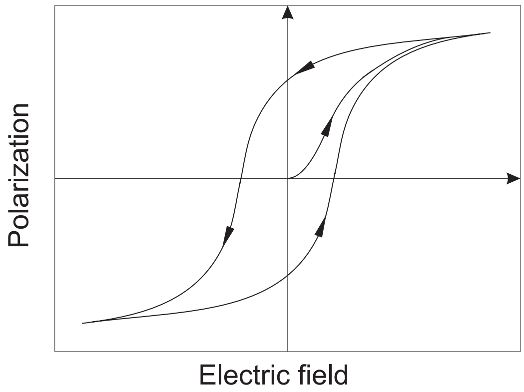

Figure 1.1: Typical hysteresis loop for ferroelectric materials

easily prepared in ceramic form. Taking into account all these properties one can conclude that the discovery of oxides with the ferroelectric phase was a significant breakthrough from the point of view of the fundamental science and applications. Therefore the scope of this thesis includes study of materials connected to a large extent with the perovskite ferroelectrics.

1.1.1 Ferroelectric phase transition

As already pointed out the ferroelectric state does not exist above temperature T_C which is called ferroelectric PT temperature or Curie point. At high temperatures, above T_C, one observes a high-symmetry (non-polar) phase of the material, while below T_C a low-symmetry (polar) phase sets in. Temperature dependence of the permittivity measured along the polar axis shows a peak at the Curie point and can reach values of up to $\sim 10^5$. Above T_C it usually obeys the Curie-Weiss law

$$\varepsilon = C/(T - T_0) + \varepsilon_\infty, \tag{1.1}$$

where C is the Curie-Weiss constant, T_0 is the extrapolated Curie-Weiss temperature ($T_0 \leq T_C$) and ε_∞ is the contribution to the permittivity of high-frequency phonons and electrons.

Some materials cannot achieve the non-polar phase because their melting temperature is higher than the Curie point. On the other hand there are materials obeying (1.1) and exhibiting only paraelectric phase in the whole temperature range. They are so-called incipient ferroelectrics ($SrTiO_3$, $KTaO_3$), and their extrapolated PT temperature occurs to be negative $T_0, T_C < 0$.

For better understanding of the PT process in the ferroelectric materials let us base its description on phenomenological Landau-Devonshire theory. Many of the physical properties of ferroelectrics in a temperature region near the PT can be interpreted and/or explained in terms of this theory. Despite the fact it gives a purely macroscopic picture, i.e. without any description of a physical mechanism responsible for the ferroelectric properties, it has a significant advantage of being independent of any particular microscopic model. Therefore Landau-Devonshire theory leads to quite general results. In the simplest ideal case where the paraelectric phase is non-piezoelectric and without taking into account stress effects one can write Helmholtz free energy potential as a power expansion of the macroscopic polarization

$$F(P) = \frac{\alpha}{2}P^2 + \frac{\beta}{4}P^4 + \frac{\zeta}{6}P^6 + \dots. \tag{1.2}$$

This expression is written under assumption that the polarization in the material is directed along only one crystallographic axis. In the centrosymmetric high-temperature phase the potential must be an even function of the polarization. Coefficients α, β and ζ, namely their signs and magnitudes, determine the class of the PT and, consequently, the behavior of the dielectric properties in the proximity of the Curie point.

Let us first discuss the harmonic coefficient α. Taking into account only the first term of Helmholtz potential (1.2) and using the dielectric equation of state one can get expression for an applied external electric field E

$$E = \frac{\partial F(P)}{\partial P} = \alpha P. \tag{1.3}$$

The constitutive relation for the polarization then allows us to understand the meaning of the coefficient α,

$$\frac{1}{\alpha} = \frac{\partial P}{\partial E} \equiv \varepsilon_0 \left(\varepsilon(T) - \varepsilon_\infty\right), \tag{1.4}$$

i.e. the coefficient α describes the contribution to the permittivity of the processes involved in the polarization P. As it was already mentioned, temperature dependence of the permittivity in the PE phase usually obeys the Curie-Weiss law (1.1); after its substitution into (1.4) the expression for α reads

$$\alpha = \frac{1}{\varepsilon_0 C}(T - T_0). \tag{1.5}$$

The harmonic coefficient α is linearly dependent on temperature and it acquires negative values below the Curie-Weiss temperature.

In the paraelectric phase coefficients α and ζ are found to be positive for all ferroelectric materials, while β can be either positive or negative. Let us shortly consider both cases in this introduction: (i) $\alpha, \zeta > 0$ and $\beta < 0$, and (ii) $\alpha, \beta, \zeta > 0$ in the paraelectric phase.

Case (i) Generally, stable states of a system are those for which the free energy has the minimum. In this case (where $\alpha, \zeta > 0$ and $\beta < 0$ in the paraelectric phase),

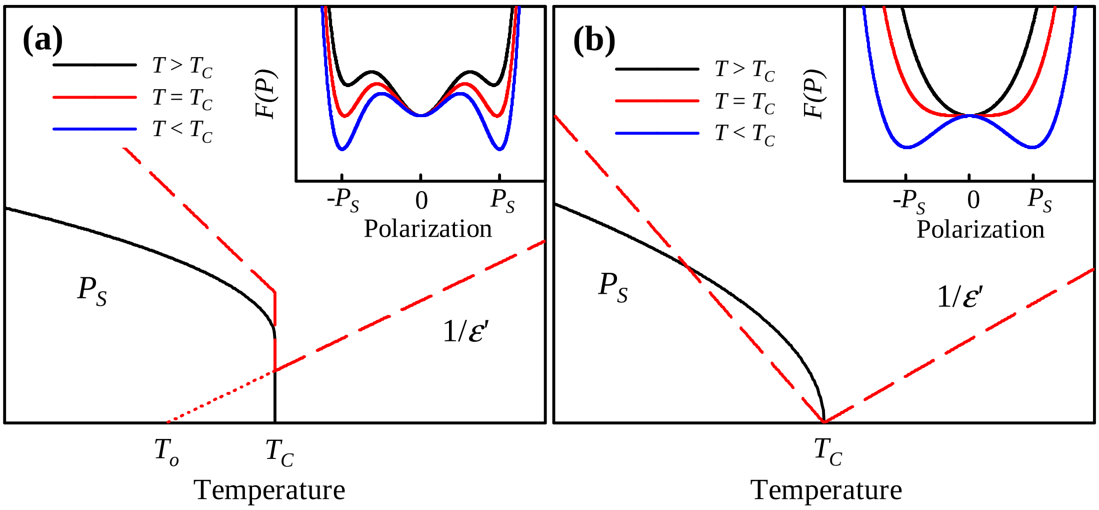

Figure 1.2: Schematic temperature dependence of the spontaneous polarization (solid curves) and reciprocal permittivity (dashed curves); insets: schematic illustration of Helmholtz free energy potential at different temperatures in the case of: (a) the first-order phase transition, and (b) the second-order phase transition.

the free-energy potential posses one minimum for $P = 0$ and two side minima for $P = \pm P_S \neq 0$. A thermodynamically stable state corresponds to the global minimum of the free energy (see inset of Fig. 1.2a). At high temperatures the global minimum corresponds to $P = 0$. At the PT temperature $T = T_C$, all minima become equal, and below T_C the stable states are with $P = \pm P_S$. In this way the polarization P exhibits a discontinuity at T_C (Fig. 1.2a), and this particular PT can be assigned to the first-order class. Evidently, this process is accompanied by a latent heat and discontinuous change of the entropy and volume. For this PT the extrapolated Curie-Weiss temperature is lower than the actual PT temperature ($T_0 < T_C$, see Fig. 1.2a). $BaTiO_3$ is the most studied example of ferroelectric experiencing the first-order phase transition.

Case (ii) As far as all the coefficients (α, β, ζ) are positive the only stable state is that corresponding to $P = 0$. It means that only the non-polar state is possible above the PT temperature where $\alpha > 0$. The harmonic coefficient α is temperature dependent (1.5) and the others are assumed here to be independent. As soon as α becomes negative, the shape of Helmholtz free energy changes such that $P = 0$ becomes a local maximum and two symmetrically positioned minima for $P \neq 0$ will appear (see inset of Fig. 1.2b). Therefore, the stable states of the structure correspond to $P = 0$ for $\alpha > 0$ (i.e. $T > T_0$) and to $P = \pm P_S$ for $\alpha < 0$ (i.e. $T < T_0$). The Curie-Weiss temperature coincides with the actual phase transition temperature ($T_0 = T_C$, see

Fig. 1.2b). In this case the change in polarization with temperature is continuous and the transition is of the second-order. The changes in the material structure are continuous, but the specific heat has a discontinuity. An example material is $LiNbO_3$.

1.1.2 Critical dynamics near the ferroelectric phase transition

Depending on mechanisms of microscopic proccesses taking place at temperatures near the Curie point the character of the PT can be divided in three main groups:

- Displacive,
- Order-disorder,
- Crossover.

The main characteristics of each group are discussed below. One of low-frequency phonon modes in ferroelectric crystals is usually called the soft mode (SM) due to softening (decreasing) of its frequency when the structural PT is approached upon changing an external thermodynamic force (temperature, field, pressure). At the PT the soft-mode frequency is very low and the crystal structure becomes unstable with respect to the atomic displacements corresponding to the eigenvector of the SM. This picture describes the *displacive* PTs which usually occur in well-ordered and relatively weakly anharmonic crystal lattices [9]. The thermodynamic Landau theory of PTs [10] together with the Lyddane-Sachs-Teller relationship [11] imply that the temperature dependence of the SM frequency should obey the Cochran law [1, 12]

$$\omega_{SM}^2 = A(T - T_0), \tag{1.6}$$

where A is a constant and T_0 is the already introduced Curie-Weiss temperature.

In a very ideal case, as it shown in Fig. 1.3a, B-type ion of the perovskite structure does not feel the weak bottom relief of the potential because an energy barrier ΔE is much lower than the energy of thermal oscillations kT_C. The oscillation of the ion is connected to the soft mode and its frequency is relatively low.

In reality this simple picture of the soft-mode behavior does not occur in all ferroelectric materials. Mainly this is because such materials are frequently partly structurally disordered and/or strongly anharmonic. In Fig. 1.3b we see a picture of the high-temperature phase where B-type ions occupy two or more equivalent positions close to the average one. Such a phase is disordered. Dynamical hoping of the ions among the available positions gives rise to a dielectric relaxation at frequencies usually below the phonon frequencies. The relaxation frequency ω_R corresponds to the maximum in the dielectric loss spectrum. Its decrease when the PT is approached is known as a critical slowing down and obeys

$$\omega_R = A_R(T - T_0), \tag{1.7}$$

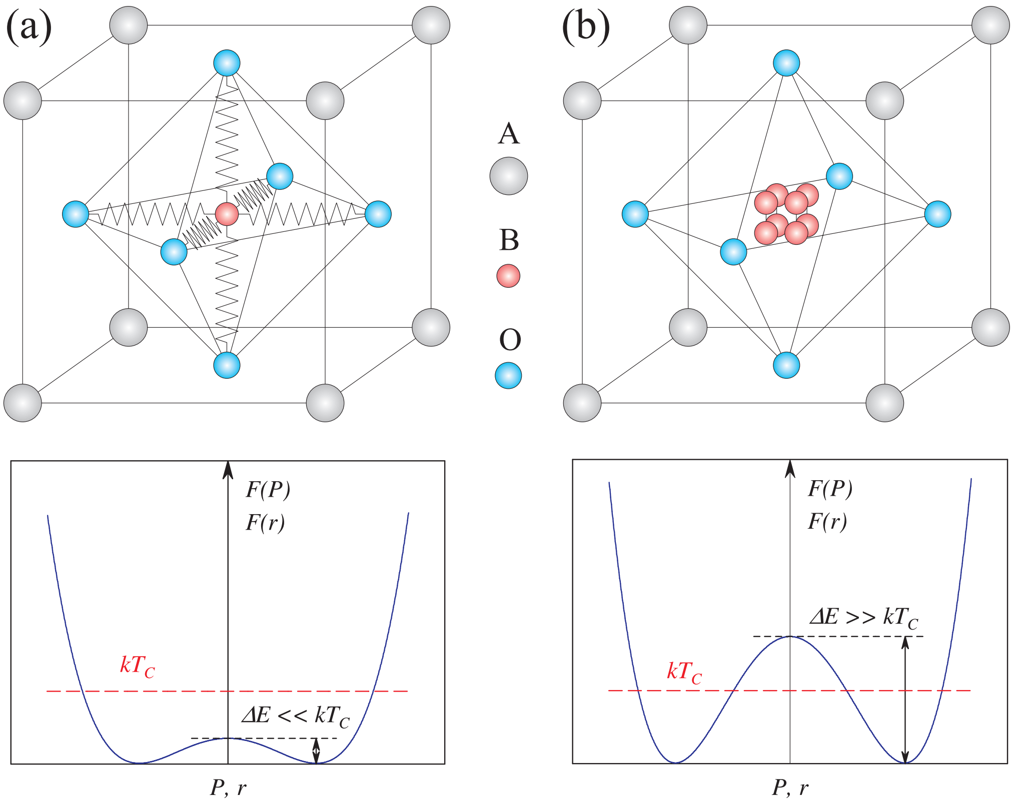

Figure 1.3: Schematic picture of perovskite crystal structures ABO_3 with possible positions of B ion together with a schematically illustrated bottom relief of the soft-mode potential: (a) displacive, and (b) order-disorder character of PT.

which, in the static limit, leads to the Curie-Weiss law (1.1) for the permittivity. This behavior is typical for the *order-disorder* PT [9].

The energy ΔE of the barrier at the bottom of the potential is much higher than the energy of thermal oscillations kT_C near the Curie point (Fig. 1.3b); as a result, between its jumps the ion oscillates within one minimum, its amplitude is small and, correspondingly, its frequency is high. It is, indeed, the microscopic mechanism of the central mode which drives the ferroelectric PT of order-disorder character. The higher-frequency oscillation mode plays here a secondary role unlike in the displacive PTs.

It should be mentioned that when a phonon mode becomes overdamped ($\Gamma_{SM} > 2\omega_{SM}$) it can be very hard to determine experimentally its frequency. It was shown in [13] that the response of an overdamped oscillator is quite similar to that of the Debye relaxation at frequencies of the dielectric-loss maxima and below. In this case the soft-mode frequency ω_{SM} and the soft-mode damping Γ_{SM} lose their separate physical meanings and it is impossible to determine them unambiguously. Therefore it is sometimes reasonable to describe even the displacive PT by a relaxation whose frequency exhibits the linear critical slowing down with $\omega_R = \omega_{SM}^2/\Gamma_{SM}$.

Some ferroelectric materials show more complicated dynamic anomalies in the vicinity of the PT which contain characteristics of both the displacive and the order-disorder behavior. Usually, in the high-temperature phase the softening of the soft mode is observed on cooling, but near the Curie point it stops and an additional relaxation appears. The latter has a substantial contribution to the permittivity and it is frequently called a central mode (CM). This character of the phase transition is naturally called *crossover* since it involves a transfer from the displacive to the order-disorder character.

Well-defined phase transitions which occur in perfectly homogeneous systems were considered up to now. In practice, the intention to prepare materials with on-demand dielectric properties results in nanoscopically and sometimes even macroscopically inhomogeneous systems, such as: doped crystals, ceramics, thin films, solid solutions, composites etc. The PT in these systems is not sharp and the permittivity shows a broad maximum in its temperature variation. Sometimes relaxor or dipolar glass behavior can be observed. Although the picture of critical processes becomes rather complicated the concept of the SM and the CM can be still used here for the interpretation [14, 15].

1.1.3 Simple perovskite oxides

Let us look more in details on the infrared-active vibrational modes of this structure. Most of the perovskite ferroelectrics under normal conditions in the high-temperature phase have a simple cubic ABO_3 perovskite structure; this is valid, for example, for classical ferroelectrics like $BaTiO_3$, $PbTiO_3$, $KNbO_3$ and also for incipient ferroelectrics such as $SrTiO_3$, $KTaO_3$. This structure has three triply degenerated zone-center infrared-active modes which possess the same symmetry $3F_{1u}$. Each eigenmode is represented by vibrations of atoms giving rise to a dipole moment. From now on, let us consider only one polarization component assumed to be parallel to a chosen Cartesian coordinate axis, e.g. z-axis. Complete set of the normal coordinates forming basis for these three modes, as suggested by J. Hlinka and coworkers [14], can be chosen as follows. Under the assumption that the skeleton of O_6 octahedra is a rigid unit of the structure, one mode can be described by relative oscillations of the B-atom and O_6 octahedron (Fig. 1.4a). This mode induces the ferroelectric instability in $BaTiO_3$ and $KNbO_3$ crystals and it is called after J.C. Slater (Slater mode) [16]. Oscillations of A-cations against the BO_6-octahedra framework (Fig. 1.4b) correspond to the so-called Last mode [17]. In the case of light A-site ions this mode can be considered to some extent as an “external” mode with respect to the BO_6 rigid structural unit. Completely different situation occurs when A-sites are occupied by heavy cations, e.g., in $PbTiO_3$. Here, in contrast to many other perovskites, the eigenvector of the lead titanate ferroelectric soft mode corresponds primarily to the Last mode. The third polar degree of freedom connected with the distortion of the O_6 octahedra is shown in Fig. 1.4c. It is denoted after J.D. Axe (Axe mode) who demonstrated that its

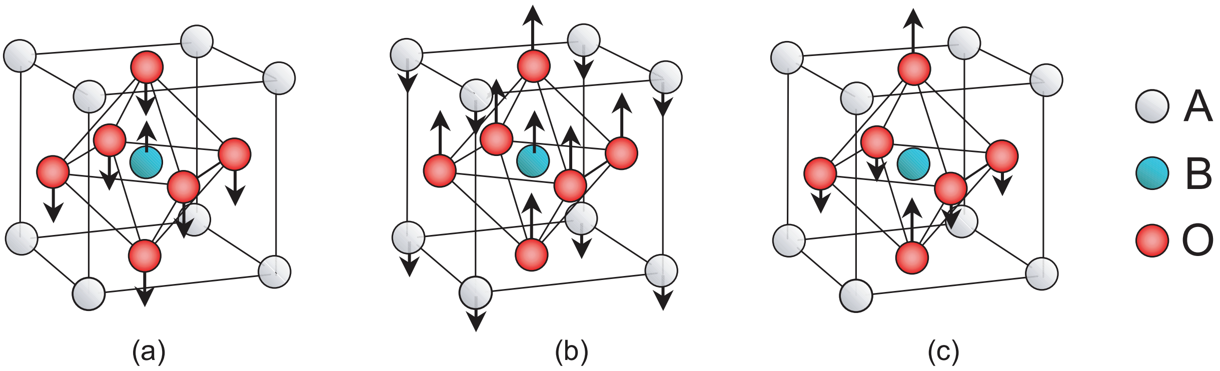

(a) (b) (c)

Figure 1.4: Relative displacements of ions of (a) Slater, (b) Last and (c) Axe modes of oxide perovskites (ABO_3) in normal coordinates. After [14].

eigenvector closely corresponds to the highest-frequency infrared mode [18].

Historically, Last suggested that the oscillation of A-cations against the BO_6-octahedra framework should be attributed to the lowest-frequency mode. However Spitzer et al. [19] concluded after comparing the infrared spectra of $SrTiO_3$ and $BaTiO_3$ with that of TiO_2 that the eigenvector of the Last mode could be assigned to the intermediate-frequency mode. On the other hand, Perry and co-authors [20] preferred Last's suggestion because in a comparative study of several titanium perovskites the frequency of the lowest mode was the most sensitive to changes in A-site cation. In turn, in a theoretical analysis of $SrTiO_3$ Joseph and Silverman [21] were unable to distinguish between a set of solutions for the soft mode. They found two possible sets: one corresponding to the description of the ferroelectric mode as discussed by Slater [16], and the other to an eigenmode as proposed by Last. Obviously there was a broad scientific debate about which mechanism corresponds to the soft mode. In 1967 J.D. Axe [18] made a relatively clear conclusion based on assignment of so-called apparent ionic charges concerning the type of the soft-mode vibrations. He stated that at least for the perovskite oxides studied in his work ($BaTiO_3$, $SrTiO_3$, $KTaO_3$) reasonable assignments of the apparent charges can only be made when the lowest-frequency mode behaves like the Slater mode, and, consequently, the intermediate-frequency mode is closely related to the Last mode, as Spitzer et al. [19] previously suggested.

1.2 Tunability of dielectric properties

Rapid development of high-frequency electronic and optical technologies needs new materials and/or structures with precisely defined dielectric properties. On the one hand, instability of these properties is a serious problem for components being developed, and ways to overcome this drawback should be found. The main driving forces causing the instabilities are changes of operational conditions to which the components are exposed. Mainly changes of temperature, but also external electric or magnetic fields, mechanical stress and even the device illumination should be taken into account during an engineering process. Additionally, some irreversible processes can gradually change the properties of materials and, consequently, operational characteristics of the device. On the other hand, some devices are intended for tunable applications. Usually, one or several components of a device have tunable intrinsic properties controlled by extrinsic parameters. Naturally, the tunability of dielectric properties is of great interest for the material science community [22–26]; research and development of new tunable materials and/or structures are in progress.

This section of the thesis is intended to provide a general insight into tunable properties and capabilities of semiconductors, ferroelectrics, and resonant structures in the terahertz (THz) frequency range.

1.2.1 Tunable properties of semiconductors

High-resistivity semiconductors are especially interesting for the THz technology. Their ground state, where all electrons are in the valence band, implies complete transparency and absence of dispersion for the THz radiation. Photoexcitation of electrons from the valence band to the conduction band switches on a strong interaction of the semiconductor with the THz radiation mediated by free charge carriers. In fact, free carriers lead to a significant increase of the imaginary part and decrease of the real part of the permittivity below the plasma frequency. Therefore, undoped semiconductors have a big potential to be used as THz modulators or switches controllable by the intensity of optical excitation [27,28]. Evidently, for an efficient control, the photon energy of the excitation light should be higher than the band gap energy. An example of optically tunable reflectance and phase shift of a THz wave in a single crystalline GaAs plate is shown in Fig. 1.5. In this work [28] the authors presented light-controllable reflectivity of an internal reflection of the THz pulse, in GaAs: the THz pulse propagating inside the plate is reflected on a GaAs-air interface which may be photoexcited or not by an optical pump. A delay time between the THz pulse and the pump pulse was chosen that the GaAs surface is excited few ps before the THz pulse arrival, see Fig. 1.5a. Depending on the optical pump fluence two regimes can be achieved. Under moderate pump fluences ($\sim$5 μJ/cm^2) the excited layer is rather thin, and its effective refractive and absorptive indices are small and have comparable values (in the vicinity of the plasma frequency which falls into the THz range).

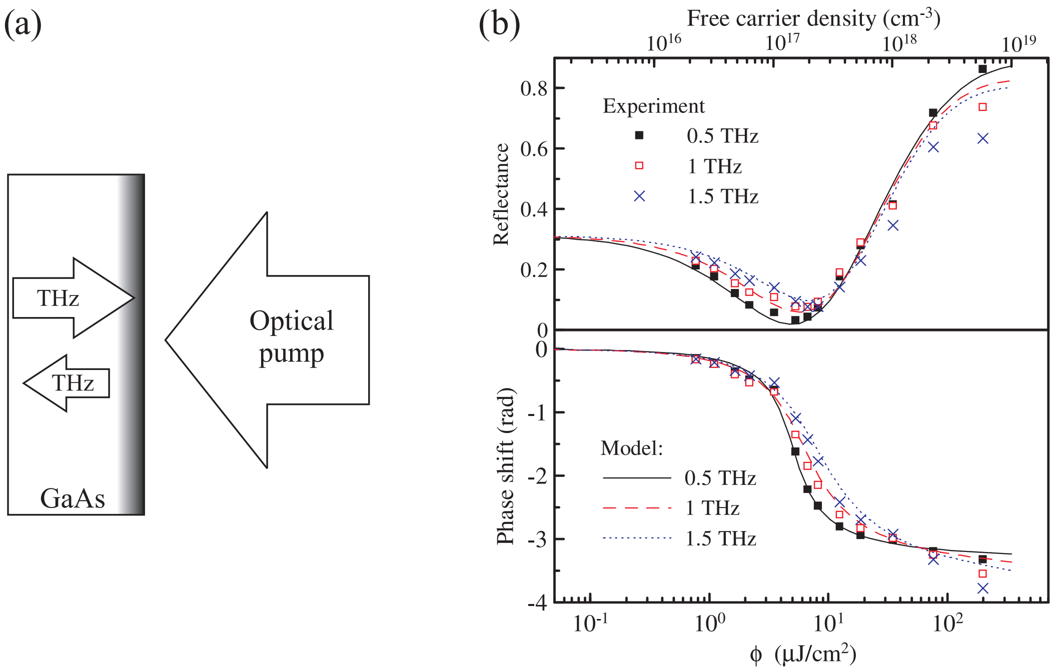

Figure 1.5: (a) Schematic picture of the GaAs plate with the optical pump pulse and the THz pulse interacting with the excited free carriers whose concentration is shown by the gray color. (b) Power reflectance and phase shift of the internally reflected THz wave versus incident optical pump fluence ϕ and the corresponding free carrier density for optical wavelengths of 810 nm. After [28].

These conditions lead to an antireflective regime (reflectance $<$ 10 %, see Fig. 1.5b), i.e. the excited layer plays the role of an antireflective coating on the interface between non-excited GaAs and air. At higher optical fluences ($>$ 200 μJ/cm^2) the thickness of the excited layer is larger and the concentration of carriers is high which imply quite high values of the refractive and absorptive indices. As a result, a highly reflective regime sets in, where the reflectance of up to 85 % is observed for the radiation at 0.5 THz (see Fig. 1.5b). The layer with high concentration of the free carriers can be considered as a metallic mirror in this case. These phenomena are accompanied by an appropriate phase change during the reflection (Fig. 1.5b).

The lifetime of free carriers in the semiconductor is a very important parameter. Depending on it, two regimes can be marked out for applications: a pulsed one and a continuous one. In the case of pulsed regime, the carrier lifetime determines the maximum switching rate; for example, GaAs with a sub-nanosecond lifetime is suitable for applications with a fast response [29]. Semiconductors with a long lifetime of free carriers are suitable for a low rate modulation or attenuation of continuous-wave sources. Several works have been reported about this phenomenon [30, 31] where silicon was typically used as the material with a long carrier lifetime.

Another interesting possibility of modulation consists in changing the carrier concentration by electronic injection or by electric-field gating. In the work of T. Kleine-Ostmann [32] the room temperature modulation of THz signal was achieved by reducing the electron density in a gated two-dimensional electron gas.

1.2.2 Tunable properties of ferroelectrics

The idea of using ferroelectric materials as functional tunable components in devices is not new, it dates more than four decades back [33]. Despite this fact, quite intense investigation and developments in this area were made only in the last two decades. The potential of substantial miniaturization of microwave components and their integration into microelectronic circuits due to the development of thin and thick ferroelectric film preparation technology is the main reason for the increased interest. In this subsection the main properties of tunable ferroelectric materials are provided which can be found in numerous review papers published recently on this topic [22, 23, 34–36].

Intuitively, the required material properties are a high tunability and low dielectric losses. But, in reality, the development of appropriate material is not an easy task and many questions and problems can arise.

A high value of the permittivity in the paraelectric phase of ferroelectrics is due to a delicate compensation of microscopic forces which keeps the material in a non-poled state. Therefore, the restoring force which is opposite to the poling action of the applied electric field is weak. This is the origin of the high permittivity of the material. It can be further increased in the ferroelectric phase due to the contribution of ferroelectric domains. However, this contribution is expected to be in the microwave and lower frequency ranges which are below the frequency range of our interest here.

Of course, one of the main reasons of interest devoted to the ferroelectrics (besides their high value of the permittivity and domain switching) is a strong dependence of their permittivity ε on the applied bias electric field. Such dependence is called tunability τ and it is defined in the literature as the ratio of the permittivity of the material at zero electric field to its permittivity under applied field E:

$$\tau = \frac{\varepsilon(0)}{\varepsilon(E)}. \tag{1.8}$$

Sometimes it is more convenient to use the relative tunability τ_r which is defined as follows:

$$\tau_r = \frac{\varepsilon(0) - \varepsilon(E)}{\varepsilon(0)}. \tag{1.9}$$

An example of electric-field dependence of the dielectric constant for a bulk ferroelectric material $Ba_{0.6}Sr_{0.4}TiO_3$ in the ferroelectric phase is presented in Fig. 1.6. In comparison with common microwave materials the ferroelectrics have rather high dielectric losses which should be taken into consideration in the device design.

It is thought that the displacive type of ferroelectrics is better for the tunable applications since the material may exhibit a high tunability and relatively low dielectric losses. In turn, order-disorder materials usually have much smaller permittivity especially at microwave frequencies [33]; as a result they show a smaller tunability. The performace of the materials should be estimated regarding their applications [23, 38, 39].

Temperature dependence of the permittivity is another important issue which should be considered discussing ferroelectrics. The permittivity changes drastically with temperature and it has a maximum in the PT point. Since the best tunability is achieved for high values of the dielectric constant it is better to use ferroelectric materials in the vicinity of their Curie temperature. However, in this regime the material exhibits a strong temperature dependence of the permittivity, which is frequently a drawback for real-life applications. At the same time, increasing the dielectric constant usually leads to an increase of the dielectric losses. Altogether it means that the material intended for application in tunable devices should have optimal choice of parameters for the best device performance.

Ferroelectrics in many forms including bulk single crystals and ceramics, thin and thick films can be used as tunable components. Actually the ferroelectric materials were used in a large number of tunable devices, such as: tunable dielectric resonators and tunable filters [40–43], antennas [39], varactors [22, 44], microwave phase shifters [45–47], voltage controlled oscillators [48], frequency modulators [49] and tunable power dividers [50].

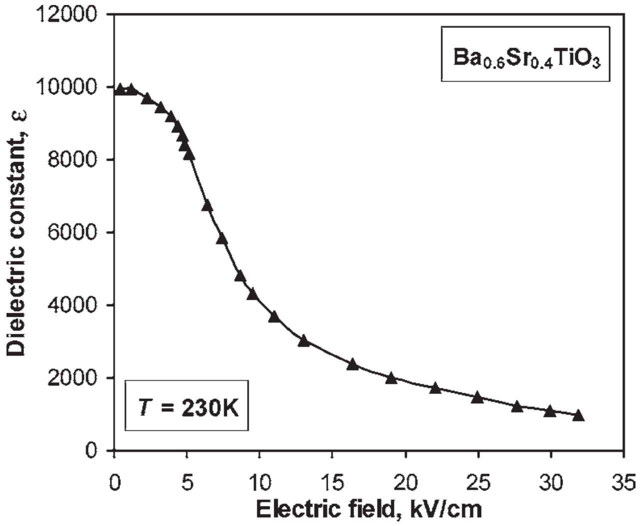

Figure 1.6: Typical field dependence of the dielectric permittivity of a tunable ferroelectric material $Ba_{0.6}Sr_{0.4}TiO_3$ slightly below the PT temperature [37].

Dielectric losses in ferroelectrics

As already mentioned, one of the most important properties of ferroelectrics for applications is the dielectric loss. As we discuss later more in details, the best choice for tunable applications are incipient or regular ferroelectrics of displacive type in the paraelectric phase. Generally, the dielectric losses of these materials consist of a sum of intrinsic and extrinsic losses [23, 51].

The origin of the intrinsic (sometimes called fundamental) losses is the interaction of the ac field with phonons of the material. The theory of the losses in the microwave frequency range coming from this interaction has been developed by Gurevich and Tagantsev [52] for crystalline materials with a well defined phonon spectrum. Considering the frequency range up to IR we can distinguish four most efficient mechanisms of the intrinsic losses:

- **Resonance single-phonon loss**. It is the strongest contribution associated with a resonant absorption of photon creating a phonon with the same energy and wave vector. This mechanism is responsible for the absorption in the vicinity of polar optical phonon eigenfrequencies at the Brillouin zone center. Therefore, this process is frequently dominating in the THz, far-IR and IR frequency ranges near phonon absorption lines, but not in the microwave range and lower frequencies.

- **Three-quantum loss**. This mechanism corresponds to a photon absorption processes involving two phonons: difference frequency absorption. Such process involves an annihilation of one phonon with frequency ω_1 and the creation of another phonon with the same vector and frequency ω_2 such that $\omega_{photon} = \omega_2 - \omega_1$. It can take place near the regions of degeneracy of the phonon branches in the Brillouin zone, where the difference between the frequencies of two different phonon branches is small. Another process when the photon generates two low-frequency phonons with opposite wave vectors is also possible. However, this process cannot contribute significantly in the microwave range.

- **Four-quantum loss**. Here the photon absorption process involves three phonons. The wave vector of the third phonon acting in the process adds an additional degree of freedom and makes possible not only vertical transitions between the phonon branches, but also transitions within one branch. It means that not only the degeneracy regions but the whole thermally excited part of the Brillouin zone contributes to the loss.

- **Quasi-Debye loss**. This mechanism, observed by Coombs and Cowley [53], stems from the changes in the phonon distribution function of the crystal due to the interaction with the electromagnetic field. It is allowed only in non-centrosymmetric crystals where the phonon frequencies are linear functions of a small electric field applied to the crystal [54]. Ac field oscillations cause time modulation of the phonon frequencies and in such a way they induce a deviation of the phonon distribution function from its equilibrium value. This relaxation of the phonon distribution function contributes to the dielectric loss, like in the case of a relaxation of the distribution function of the dipoles in the Debye theory [55]. Actually, the latter is at the origin of the name of this mechanism.

It should be mentioned that, when the quasi-Debye mechanism is allowed by the crystal symmetry, its contribution to the dielectric losses can be a few orders of magnitude higher than that of three- or four-quantum mechanisms in microwave frequency range [23]. Moreover, in materials for tunable applications, which are typically centrosymmetric in the paraelectric phase, this mechanism is not active. However, under a dc bias field, which breaks the crystal symmetry, the quasi-Debye mechanism becomes active. Consequently, one have to bear in mind that a dc-field-induced quasi-Debye mechanism may contribute and even become dominant in initially centrosymmetric crystals. Especially this type of losses should be taken into account in the case of thin films where high dc bias field is easily achievable.

The intrinsic losses define the lowest possible losses in each particular material with an ideal crystal structure. The main mechanisms of the extrinsic losses, which appear in the material due to the coupling of an ac field with lattice defects, can be roughly divided in the following groups:

- **Loss due to charged defects**. Ac electric field triggers off the charged defects in a material. Motion of the defects results in a generation of acoustic waves at the frequency of the applied ac field. This mechanism of extrinsic loss was proposed by Schlöman [56].

- **Loss due to local polar regions**. Various defects and structure imperfections may induce appearance of local polar regions even in typically centrosymmetric materials. For instance, it is the case of $SrTiO_3$ ceramics where infrared reflectivity investigations showed a clear presence of polar phase inclusions induced by grain boundaries [57]. Random field defects can also be responsible for the appearance of local polar regions. All these polar regions give rise to the quasi-Debye mechanism of the dielectric losses. Despite the typically small volume fraction of the polar phase this loss mechanism can be dominant due to its large contribution per unit volume in comparison with the other intrinsic loss mechanisms.

- **Loss due to anharmonic motion of charged defects**. This mechanism produces broad relaxation-like loss maxima with thermally activated relaxation times.

- **Loss due to phonon scattering on defects**. Here the phonon lifetime is reduced and the damping is increased because of the scattering on defects.

In the high-frequency range (THz and far-IR) the contribution of the extrinsic losses is small in comparison with the intrinsic losses. The extrinsic mechanism connected to local polar regions can only significantly contribute to the dielectric losses in this frequency range. It means that, in the case of high quality ferroelectric crystals, THz spectroscopy together with Fourier transform infrared (FTIR) spectroscopy give access to the intrinsic dielectric losses.

Materials for tunable applications

Finally, which materials are appropriate for the tunable applications? The tunability is practically achievable in materials with relatively high dielectric constant. For a bulk material, a reasonable value of the permittivity should exceed 1000, whereas, for a thin film, the dielectric constant exceeding 300 can be adequate due to possibility of higher field application. This restriction together with the requirement of low losses bring us to the displacive type of ferroelectrics. In addition, in order to avoid complications with a response from the domain structure, it is better to use incipient ferroelectrics or ferroelectrics in the paraelectric phase. Many materials have been pointed out as possible candidates for tunable applications. Incipient ferroelectric $SrTiO_3$ and its solid solution with $BaTiO_3$ ($Ba_xSr_{1-x}TiO_3$) attracted a lot of attention.

High quality single crystals of $SrTiO_3$ (STO) posses a high value of the permittivity (up to tens of thousands at low temperatures) and low losses. Another promising incipient ferroelectric is $KTaO_3$ (KTO) whose properties are very similar to those of STO. However, its tunability is somewhat inferior to that of STO.

The solid solution $Ba_xSr_{1-x}TiO_3$ (BST) materials are very appropriate candidates for tunable components. The permittivity maxima can be shifted in the temperature range from 0 K to 390 K depending on the barium concentration [58]. Lots of works on modification of BST ceramics by adding non-ferroelectric oxides have been published as well [59–61]. By adding a small amount of a linear dielectric material to a tunable ferroelectric one gains another degree of freedom for the control of the dielectric properties: they can be modified due to several effects. At low concentrations of the linear dielectric material the ferroelectric response is modified mainly because of doping of the ferroelectric lattice by substitution ions of the host material. In the case of high concentrations, effects of redistribution of the electric field in the material are expected due to inclusions of the linear dielectrics either at the grain boundaries or in the bulk of the material. Among oxides MgO is frequently used as a linear dielectric for the modification of BST ceramics.

Many other materials with high dielectric permittivity were investigated in terms of their possible tunable application. The compounds $Cd_2Nb_2O_7$ [62] and $(Cd_xPb_{1-x})_2Nb_2O_7$ [63] with pyrochlore structure exhibit a very high permittivty below a diffuse dielectric anomaly at 180 K. Relatively high tunability was observed in double substituted $BaTiO_3$, namely $Ba_{1-x}Ln_xTi_{1-y}M_yO_3$ with donor doping at A-site and acceptor doping at B-site [64]. The solid solution $KTa_xNb_{1-x}O_3$ (KTN) is another suitable material for tunable components. Its solubility in the full range of concentrations and the dielectric properties of $KTaO_3$ and $KNbO_3$ make this material the closest analog of BST [65].

Special attention should be devoted to ferroelectric films. They attracted a lot of interest during the last two decades generally owing to the constantly improving thin film preparation techniques. This direction for development of new tunable materials is very promising due to an opportunity of miniaturization of components and lowering of bias voltage at the same time. Best materials for the thin film preparation are mostly those of choice for bulk tunable ferroelectrics. However, properties of the bulk materials and of the films with the same composition may be rather different. The films typically show a lower dielectric permittivity and a higher dielectric loss. For the thin films (thickness less than a few micrometers) this difference is always substantial, especially when the permittivity of a bulk material is high. Additional effects must be taken into account in order to understand the dielectric properties of the film. Firstly, there are differences in processing conditions for bulk and thin film materials. In fact, it is very difficult to control precisely the stoichiometry of the film during the deposition process due to specialties of the technology. Small deviations from a desirable stoichiometry may significantly change the dielectric properties of the film. Secondly, when the film and bulk materials are chemically identical, additional effects stemming from passive layers, depletion layers, and strain may to a large degree influence the dielectric response.

The quality of the films strongly depends on the deposition technique and on the substrates used for deposition. The most typical substrates, for example for STO and BST thin films, are single crystal sapphire (Al_2O_3), lanthanum aluminate ($LaAlO_3$), magnesium oxide (MgO), dysprosium scandate ($DyScO_3$), and $(LaAlO_3)_{0.29}\times(SrAl_{0.5}Ta_{0.5}O_3)_{0.71}$ (LSAT). The last two substrates allow to grow epitaxial films of STO. Despite the thin film tunability is lower and their dielectric losses is higher than those of the bulk material the epitaxial deposition provides an additional degree of freedom. As has been shown by Haeni et al. [66], the epitaxial tensile strain in STO film coming from the substrate of $DyScO_3$ (DSO), namely from its (110) surface, induces the ferroelectric phase transition in the incipient ferroelectric. Moreover, the Curie point of the STO thin film is close to room temperature. Thus, by the proper choice of the substrate for the epitaxial deposition one can tune the phase transition temperature of the thin film material. Properties of some thin films and structures will be discussed in detail based on results obtained within the framework of this thesis.

1.2.3 Tunable properties of resonant structures

Metamaterials

The term “electromagnetic metamaterial” denotes man-made structures exhibiting specific electric and/or magnetic response which is not found in natural materials. Such structures were observed less than fifteen years ago and since then they have attracted considerable attention of researchers from microwaves up to the optical spectral band. Metamaterials are usually periodic structures with the motive much smaller than the wavelength ($< \lambda/10$) of electromagnetic radiation in the targeted spectral range. Under such condition, the response of metamaterials is mainly due to individual resonances of the structural components within the unit cell. Usually, it can be described by effective material parameters: the effective permittivity ε and the effective permeability μ [26]. Most frequently, metamaterials are associated with the property of simultaneously negative ε and μ (so called negative refraction media), but more generally their name is a synonym for structures showing artificial (sometimes tunable or switchable) resonances related to their fine structure.

Historically, Veselago was the first [67] who in 1968 discussed and analyzed wave propagation in media with simultaneously negative ε and μ. However, the broad interest of the scientific community in the materials exhibiting negative refractive index was attracted nearly thirty years later by Pendry who used the matematerial concept in order to decrease the plasma frequency of metals down to MW and THz frequency range [68, 69]. He also demonstrated a way how to get the negative effective permeability at microwaves [70] and the principle of a superlens [71]. Smith et al. introduced the term “metamaterial” in the paper reporting on the first structure with simultaneously negative permittivity and permeability in the MW range [72]. Since that time, the research in this area have being carried out very intensely, and this resulted in a huge number of publications. Concerning the THz range, Yen et al. made the first breakthrough by presenting a planar structure characterized by a negative effective permeability [73]. Then, an important paper showing new perspectives for the metamaterial applications in the THz technology has been published by Chen et al. [74]. Here the authors pointed out the possibility of spectral tuning or on/off switching of the metamaterial response which promised tremendous potential for the manipulation of THz radiation.

During the last decade a number of books or separate chapters and review papers has been devoted to the metamaterial science [25, 26, 75–77]. In this work, technological aspects of sample preparation and physical description of the near-field interactions leading to the resonant electromagnetic behavior will be omitted and an introduction into tunable applications of the metamaterials will be provided.

The electromagnetic field is inhomogeneously distributed within the unit cell depending on the fine details of the metamaterial structure. Scattering of the incident radiation on the pattern gives rise to resonances connected to this local field. Each scattering unit is individually resonant and no coupling between the neighboring units needs to be considered in order to obtain an effective resonant behavior. Usually, one deals with dielectric or metallic inclusions (scattering elements) forming a motive of the periodic structure characterized by a high permittivity or conductivity. More formally for dielectric inclusions, it means that the absolute value of the permittivity of scatterers $|\varepsilon_1|$ must be much larger than that of surrounding medium $|\varepsilon_2|$, i.e., $|\varepsilon_1| \gg |\varepsilon_2|$. The size of scattering elements much smaller than the probing wavelength enables a homogenization of the sample properties; it means that one can use an effective permittivity and permeability to evaluate the response of the structure in the far field (i.e., in transmission and reflection experiments).

For a broadband characterization of metamaterials in the THz spectral range, two experimental methods are most frequently employed: Fourier-transform infrared spectroscopy (FTIR), and time-domain THz spectroscopy (TDTS). Both methods allow recording of transmittance and reflectance spectra. However, FTIR typically provides the power (intensity) spectra while TDTS is a phase sensitive technique, which sometimes could be preferable.

Metamaterial devices are considered to be useful for the THz technology, namely the tunable applications of metamaterials are very promising. Control over radiation can be realized using either passive components (waveguides, splitters) or active components (modulators, switches, tunable filters) tunable by an external parameter. The majority of reported works used a change of the characteristic capacitance of a resonant structure to achieve the tuning or switching of the metamaterial properties. This was done by changing the conductivity of a semiconductor which forms the capacitor pads or which fills the space between the capacitor pads [74]. Another possibility consists in the tuning of the permittivity of a material filling the capacitor or of a material forming the entire metamaterial structure. In these cases, the external control parameter modifies the strength of the resonance and/or its spectral position [78]. A completely new approach of achieving the tunable response was proposed by Tao et al. [79]. Here, the authors presented a reconfigurable anisotropic metamaterial where the tuning of the resonant response is owing to a reorientation of the scattering units of the structure with respect to the electric or magnetic field vector of the incoming radiation.

The first active planar metamaterial device with a real-time control of an electrical resonant response by a low applied voltage was demonstrated by Chen et al. [74]. The device consisted of an array of gold resonator elements with symmetry not allowing the magnetic response. The metallic pattern was deposited on a 1-μm-thick n-type GaAs layer grown on a semi-insulating gallium arsenide (SI-GaAs) wafer. The metal and n-GaAs form a Schottky junction and the conductively connected metamaterial resonators serve as a metallic gate (Fig. 1.7a,b). Without an applied voltage the split-gap capacitors are short circuited by the conductive substrate and the device is not expected to display a resonant behavior associated with the electric resonators. Upon application of a voltage, a resonant transmission appears due to a restored capacitance of the split-gap. This is because an electrostatic potential applied to the metallic pattern displaces the carriers within the substrate and creates a depleted layer, i.e. the conductive connection mediated by the carriers is broken. The transmission function of such a planar device strongly depends on the resonance at 0.72 THz which is controlled by an applied reverse gate bias 0-16 V and a power of modulation of up to 50 % has been observed (Fig. 1.7c,d). A multipixel spatial modulator of THz beams based on the above described split-ring arrays assembled into a 4×4 pixel matrix has been proposed by Chan et al. in 2009 [80].

The surface current density and the local field distribution close to the resonance of

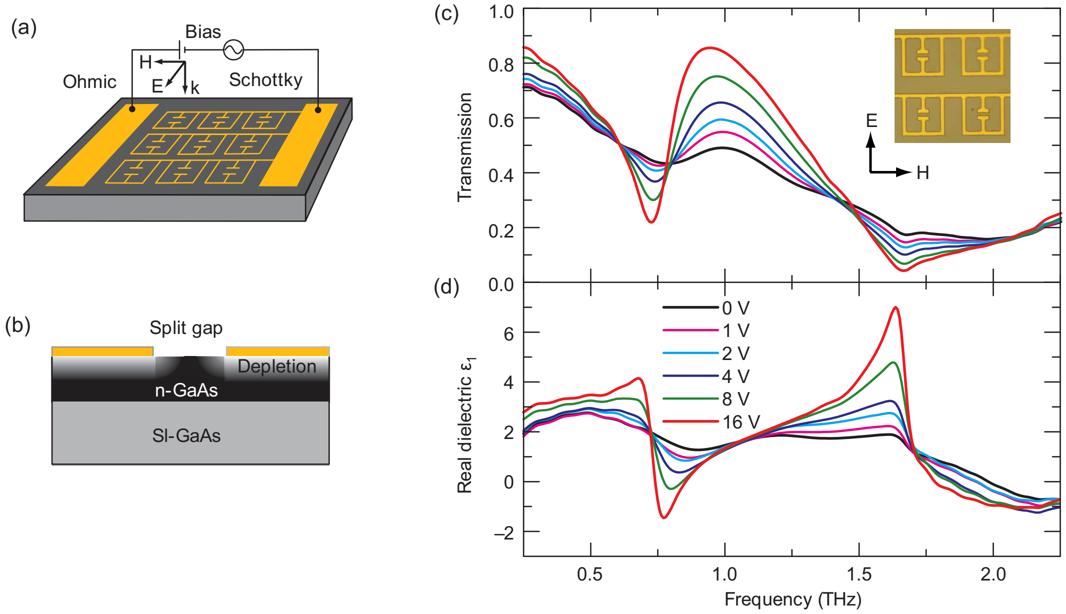

Figure 1.7: Planar electrically resonant metamaterial for THz light modulation. (a) Scheme of the structure: the metamaterial elements are patterned with a period of 50 µm to form a planar array of 5×5 mm^2. A voltage bias applied between the Schottky and ohmic contacts controls the substrate charge carrier density near the split gaps. (b) Diagram of the substrate and the depletion region near the split gap, where the grey scale indicates the free charge carrier density. (c) Frequency-dependent transmitted intensity of THz radiation and (d) the corresponding permittivity for various gate biases. After [74].

the nonmagnetic split-ring based planar materials of various symmetries have been studied by the same group [81–83]. They also recently demonstrated the possibility of phase modulation of the THz radiation by using a similar principle and similar structures [84].

Modified designs of the metamaterial patterns but the same operational principle based on Schottky contact and depletion layer as described above were proposed by Paul et al. [85] and by Chen et al. [86]. The first group deposited onto n-doped GaAs a gold structure in the form of crosses in order to obtain a polarization independent response. The second one investigated an electric control of extraordinary transmission of THz radiation through subwavelength metal hole arrays.

A completely new approach for the tuning of THz metamaterial response has been first proposed by Padilla et al. [87]. It was optically controlled switching of the response; later on it was demonstrated on a picosecond time scale [88]. In these works a nonmagnetic metallic pattern like that shown in Fig. 1.7a is deposited on an undoped semiconductor. When the semiconductor is in its ground state the structure shows a resonance due to the capacitance of the split-gap leading to a low transmittance of the structure close to the resonance frequency. Using the substrates exhibiting ultrashort carrier lifetime makes it possible to get an ultrafast response of the deposited structure [88]. A sample consisting of ErAs/GaAs superlattices grown by molecular beam epitaxy on top of a semi-insulating GaAs substrate was demonstrated to be an appropriate material for the deposition of metamaterial pattern because its free carrier lifetime is ultrashort (in the picosecond and sub-picosecond range) and it can be controlled by changing the period of the superlattice [89]. Femtosecond optical pulse at 800 nm injects electrons into the conduction band of GaAs leading to a large increase of the conductivity of the semiconductor structure. Free carriers shunt the capacitive regions of the metamaterial structure eliminating the resonance. The THz transmittance is increased under illumination by about 50 % at resonance frequency. Similar experiments were reported with double-ring resonator structures deposited on a high-resistivity silicon substrate [90] and experiments without the time resolution were carried out with classical double split-ring resonators deposited on high-resistivity GaAs [91].

Tuning of the metamaterial resonant frequency by means of optical excitation was reported in a few experimental works. In one of them, the authors deposited gold split-rings on sapphire, but the capacitor plates of the split ring were partly made of a high-resistivity silicon film [92]. This allowed controlling the capacitance of the split-rings by interband optical excitation of silicon and, in a such a way, the metamaterial resonance could be dynamically tuned. As a result, an optical switching of the metamaterial resonance between 0.85 and 1.05 THz has been achieved. Slightly different approach of tuning of the metamaterial resonant response was proposed by another group [93]. An electrically resonant split-ring structure deposited on a dielectric substrate had three capacitor gaps and two of them were filled with a suitable semiconductor layer which was then optically excited. In the simulations made for silicon the resonant frequency displacement from 0.7 to 1 THz was presented. Similar idea of dual electrically resonant metamaterial structure unit with two different split-gaps has been experimentally demonstrated in THz range [94].

Several papers were devoted to the temperature tuning of the metamaterial resonance. The frequency range with the negative permeability and its tunability between 0.2 and 0.4 THz were shown for a dielectric metamaterial composed of an array of $SrTiO_3$ rods [78]. The tunable effect was achieved due to a strongly temperature dependent permittivity of $SrTiO_3$. Although its permittivity is in principle tunable by the electric field in the THz spectral range (as it will be shown in this thesis), the electric-field tuning of the effective permeability in this structure has not been experimentally shown, yet. Tunable ferroelectrics can be also used as a substrate for metallic metamaterial resonant elements; it can be either a bulk material or a ferroelectric layered structure. The tuning of the resonant frequency is achieved by means of modification of the substrate permittivity within the capacitor active area of the metamaterial resonator. Recently, Singh et al. demonstrated thermally tunable resonant response of a planar metamaterial deposited on a single crystal of $SrTiO_3$ [95]. A thermal tuning of the response of the metamaterial based on niobium nitride (NbN) superconductor was observed by Wu et al. [96]. Here the driving force of the tuning was the dramatic change of the inductance and resistance of the material close to the conductor-to-superconductor phase transition. An interesting idea of thermal triggering of the insulator-to-metal phase transition in VO_2 which leads to an increase in its conductivity have been employed in order to achieve tunable response in a VO_2 cut-wire metamaterial structure [97]. The authors reported 65 % change of the metamaterial THz transmittance by temperature change between 300 and 340 K.

He et al. [98] showed magnetically tunable negative refractive index of a metamaterial composed of ferrite-dielectric and metallic mesh in the microwave range. The tunability by external magnetic field is obtained due to the magnetic properties of a ferrite. Electrically resonant THz metamaterial controlled by an external magnetic field has been proposed recently [99]. In this work an array of the parallel plate capacitors having one capacitor plate sustained by a flexible cantilever coated with a magnetic thin film was prepared. As a result, the tunability of resonant frequency of the structure was realized by bending the cantilever in an external magnetic field.

Photonic crystals

Photonic crystals (PCs) usually consist of a periodic pattern of low-loss dielectric media with a high contrast of the permittivity. These structures exhibit a forbidden band of frequencies where they are completely opaque for transmission [100–102]. PCs can have one-, two- or three-dimensional translational periodicity.

Unlike in the metamaterials, where the periodicity is not a primary concern and each structure element resonants individually, the PCs must possess the structural periodicity with the length scale comparable to the wavelength. The characteristic response of the PC is due to interferences between partially reflected and diffracted waves on the structure elements. The condition $\lambda \approx \sqrt{\varepsilon} l$, where ε is the dielectric constant of one of the structure elements and l is the PC period, ensures that constructive and destructive interference phenomena may occur in the frequency range near λ for some propagation and scattering directions [26]. These interferences lead to a formation of the photonic band structure.

Breaking of the periodicity, e.g. by inserting a defect, can result in a very narrow allowed transmission spectral line in the forbidden frequency band. This line is called a defect mode. The PC turns out to be quite transparent for electromagnetic radiation at the defect mode frequency [103]. The structure defect confines a large part of electromagnetic radiation in its vicinity [104]. Therefore, a strong enhancement of optical nonlinearity can be expected in the defect made of material with a suitable nonlinear response. A number of functional photonic structures in various modifications and spectral ranges which can serve as resonators, beamsplitters, switches, coupling structures, tunable frequency filters have been recently reported in the literature, e.g. [105–109]. It should be mentioned that the PCs open great possibilities for tunable applications and many works in this direction have already been done. Usually, tunable resonant response of the PCs is closely connected with the tunability of the dielectric properties of the defect.

One-dimensional (1D) PC can be constructed by periodic stacking of layers with a high impedance contrast, low dielectric losses and good temperature stability of their electromagnetic properties. Appropriate materials for THz frequency range can be chosen among technologically available dielectric materials. In addition to the relatively simple construction, 1D PCs give us a deeper understanding of the defect mode formation due to a possible analytical theoretical description of the structure [110, 111]. A defective 1D PC can be fabricated by inserting a defect layer in a periodic stack of layers. This structure can be understood as a Fabry-Pérot resonator with periodic Bragg reflectors enclosing the defect layer.

Recently, temperature tunability of the defect mode frequency in 1D PC have been observed in two structures [24, 112, 113]. The first one was made of two Bragg mirrors fabricated using three (0001)-oriented wafers of crystalline quartz separated by air layers and $KTaO_3$ as a defect layer [112]. The tunability of the PC originated from a strongly temperature dependent dielectric constant of the defect layer material. In such structures a high tunability is achieved when a low-index material (represented here by air) surrounds the defect layer [24]. The authors experienced a problem connected with the fragility of very thin potassium tantalate crystals, and, as a result, they did not succeed to build the structure where the defect is surrounded by air gaps. Therefore five defect modes were present in the forbidden band gap and the tuning was inhibited due to the predicted pinning of some of the spectral lines to the center of the band gap. Nevertheless, the relative tunability of 20 % and the peak transmission of the tunable defect modes of -6 dB in temperature range from 100 to 300 K have been reported. The second structure was shown to have a better performance. Here, the Bragg mirrors were fabricated using three (0001)-oriented quartz disks separated by two disks of undoped CeO_2 ceramics as high-index layers. Another improvement was done by a choice of $SrTiO_3$ single crystal as the defect layer [113]. Its temperature tunability of the dielectric constant is higher than that of $KTaO_3$ and it is mechanically more stable. The obtained structure was shown to have a single defect mode within the band gap. It was tuned from 185 GHz down to 100 GHz by cooling the PC from room temperature down to 100 K (see Fig. 1.8). In this structure the relative temperature tunability of 60 % of the defect mode frequency was reported. In addition, the peak transmission was exceeding -9 dB. The small discrepancy between the measured and numerically calculated data was ascribed to the errors in the determination of structural parameters of the PC.

An example of optically tunable response of the 1D PC crystal was reported by Fekete et al. [114, 115]. The authors prepared structures consisting of two Bragg mirrors and a thin GaAs wafer enclosed between them. Alternating layers of crystalline SiO_2 and MgO which are transparent for the visible light were used for the Bragg mirrors fabrication. The concept of the optical switching lies in an excitation of carriers in the GaAs layer from the valence to the conduction band by optical pulses. In the ground state the high-resistivity GaAs is very well transparent for the THz radiation. A relatively weak excitation leads to a substantial decrease of the transmittance at the defect frequency due to a strong

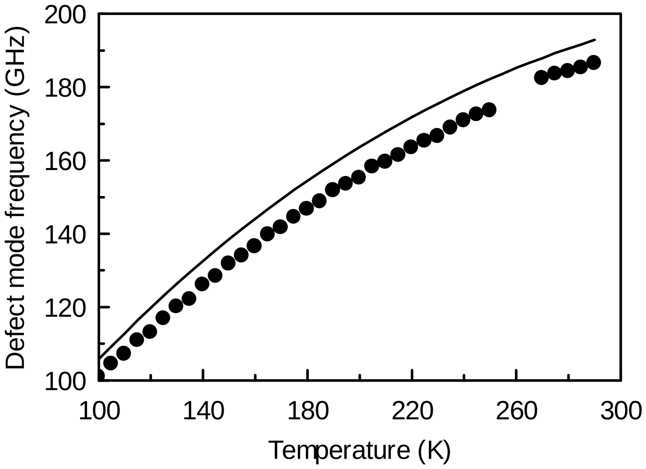

Figure 1.8: Tuning curve of the defect mode of a structure with $SrTiO_3$ defect layer. Filled circles: measured defect frequency; solid line: results of a numerical simulation. After [113].

enhancement of the electric field inside the defect. The structures were designed in order to have the defect mode in the center of the first forbidden band (cca 600 GHz). 1 μm-thick photoexcited layer with 10^{15}-10^{16} cm^{-3} free carrier concentration was shown to induce a 50 % modulation of the THz transmission of these structures. Furthermore, the maximum switching rate up to 5 GHz was possible due to a rather short lifetime (cca 170 ps) of free electrons in GaAs sample.

Chapter 2

Experimental techniques

2.1 Time-domain terahertz spectroscopy

2.1.1 Terahertz radiation

Terahertz (THz) radiation belongs to the part of the electromagnetic spectrum which is often called "THz gap" and which covers frequencies from 10^{11} to 10^{13} Hz. This band lies between the microwave range at the low-frequency side and the infrared region at the high-frequency side (see Fig. 2.1). THz radiation is invisible to the naked eye and is not dangerous to the human body as the corresponding photon energy is low (4 meV); consequently, it is non-destructive and non-ionizing radiation.

The majority of non-conductive materials, e.g., paper, plastics, wood, ceramics and clothing, are quite transparent in this spectral region. But THz light strongly interacts with free and weakly-bounded charge carriers. The fact that many chemical substances have unique fingerprints in this spectral range increases the interest of industry in commercial and security applications.

The THz region of the electromagnetic radiation is extremely important in the spectroscopy of condensed matter systems. In the past, this range was hidden to scientists and engineers due to the lack of efficient and affordable THz sources and detectors. On the one hand, generation of THz radiation by means of electronic synthesizers is not very efficient [116,117]. On the other hand, it is a hardly accessible region using optical sources because their brightness strongly decreases towards lower frequencies, according to the Planck's law. Only less than three decades ago the invention of ultrafast laser systems and of the photoconductive Auston switch [118] made the THz gap accessible. Research activities in this spectral range have risen dramatically since that time namely due to a new spectroscopic technique called time-domain THz spectroscopy (TDTS) [119,120] which is based on a coherent generation and detection of electromagnetic transients with the help of femtosecond laser pulses. These transients represent quasi-single-cycle oscillation of electromagnetic field of a few picoseconds or shorter duration. The spectral bandwidth of

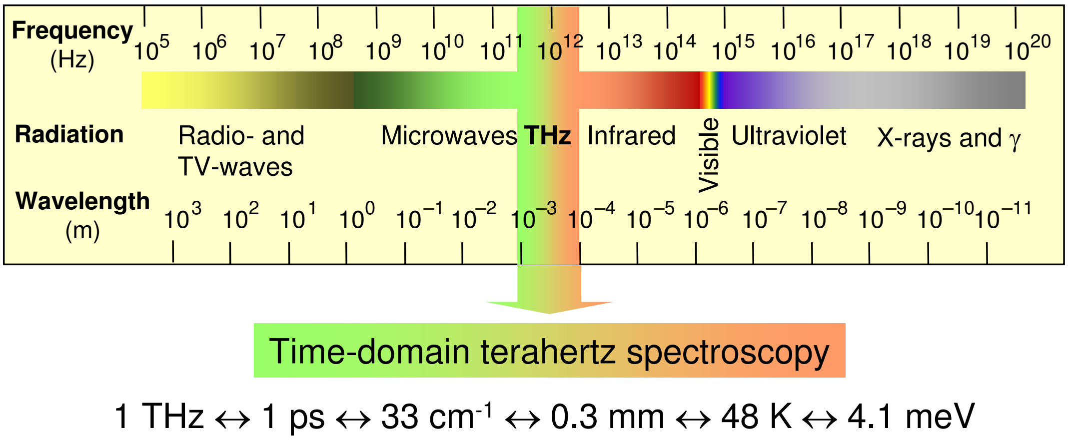

Figure 2.1: Spectrum of electromagnetic radiation. The last line shows the correspondence of 1 THz to other characteristic units: period, wavenumber, wavelength, Boltzmann equivalent temperature, photon energy. The picture is kindly granted by H. Němec.

these pulses covers one decade or slightly more typically between 100 GHz and a few tens of THz. A nice review of THz optoelectronics, which emphasizes also historical aspects, can be found in the book edited by Sakai [121].

Despite the fact that spectroscopy in the THz frequency region is a very young discipline a number of applications has already appeared. This spectroscopy is not limited to condensed matter systems, it provides novel information in chemistry and biochemistry as well. A lot of useful information about the interstellar space can be decoded from the THz spectra recorded by submillimeter observatories. Art historians can also have benefits from the THz radiation due to its ability to display murals hidden beneath coats of a plaster or paint in ancient buildings. The idea of employing the THz radiation in a high-altitude communication technique is very promising. At high altitudes, where the atmosphere is greatly rarefied, this radiation gets free from absorption caused by water vapor and gases. Therefore, communication between satellites and spacecrafts can be established using THz carrier frequency. Quality control monitoring during manufacturing of goods is an example of applications of the THz sensing and imaging potential. A closely related application deals with the THz detection of weapons and explosives and aims increasing of the public security level. A few such surveillance systems operating in the THz spectral range have been already proposed. Finally, THz radiation can serve in medicine. THz imaging allows the detection of skin tissues affected by cancer at early stages and it may also help in incipience of dental caries. The THz science and technology are very prospective, and a great number of further developments and investigations are currently in progress.

2.1.2 Generation of terahertz radiation

Historically, the first bright sources of radiation in the THz spectral range were backward-wave oscillators developed already in the 1960s. They provide coherent monochromatic radiation with a frequency limit at about 1.4 THz because of the electronic nature of the device, which is actually a variation of vacuum triodes [122, 123].

Photoconduction in ultrafast semiconductors and optical rectification [124] are two basic processes serving for generation of the THz transients. The former one will be discussed in a separate paragraph since it was used for generation of the THz pulses during this work. Optical rectification is a second-order nonlinear effect which can be observed in noncentrosymmetric materials. Here, ultrashort ($\lesssim$ 100 fs) laser pulses of a high intensity are used in order to induce the second-order effect. Therefore a broad frequency spectrum is involved in the non-linear interaction which results in a generation of difference-frequencies spectrum lying in the THz region.

Several nonlinear materials were shown to be suitable for an efficient THz generation. For example, ZnTe crystals [125], GaSe and $LiNbO_3$ crystals [126, 127] are used for the optical rectification originating from a non-resonant optical transition, when only bonded carriers are present in the material. In this case, the non-linear susceptibility is weak, and THz radiation of reasonable intensity can be generated only when the non-linear interaction takes place over a long distance. In other words, the phase matching condition [125] between the optical and THz pulses must be satisfied. The maximum possible interaction length is equal to the coherence length defined as [125]

$$L_{coh} = \frac{\lambda}{2} \cdot \frac{1}{|N_g - n_{THz}(\lambda)|}, \tag{2.1}$$

where N_g is the group refractive index of the optical pulse and n_{THz} is the refractive index of the THz component with wavelength λ. Therefore, materials with N_g close to n_{THz} are required. However, some organic crystals like dimethyl amino 4-N-methylstilbazolium (DAST) or 2-methyl-4-nitroaniline (MNA) [128,129] possess high non-linear coefficients as compared to those of anorganic crystals. This is due to a presence of molecules with very high electronic polarizabilities in the composition of crystals. Although the coherence length in these crystals can be rather short at some wavelengths (e.g. at 800 nm) an intense THz radiation can be still generated under these conditions.

The notion of the coherence length L_{coh} is meaningless in GaAs crystals at 800 nm pump wavelength [130], for which the photon energy is sufficient to cause resonant optical transitions and, as a result, the excitation beam is absorbed within a 1-µm-thick layer. In this case, the appropriate non-linear coefficient is resonantly enhanced (due to created free charge carriers) to produce intense THz pulses.

Another way of fulfillment the phase matching condition is the creation of a polarization shock-wave. The propagation of femtosecond-duration optical pulses in electro-optic materials is demonstrated to produce a Cherenkov cone (shock-wave) of pulsed radiation in the THz spectral range [131]. This phenomenon was observed in $LiTaO_3$ crystals [131], where $n_{THz} > N_g$, i.e., the phase velocity of the THz radiation is smaller than the group velocity of the incident optical pulse.

Vector network analyzers based on Schottky generators and operating in the sub-THz range appeared on the market about two decades ago [132]. Photomixing devices are shown to be very promising for the THz radiation generation: two monochromatic laser beams with close wavelengths focused to a semiconductor with a short lifetime of charge carriers induce a coherent THz radiation due to a difference-frequency generation process [133]. Recently, deposition techniques were greatly improved and allowed one to build THz quantum cascade lasers based on electrically-pumped semiconductor heterostructures [134]. Parametric generators based on a phase-matched THz generation in nonlinear crystals present another group of sources. In these generators, usually an intense near infrared laser (e.g. Q-switched Nd:YAG) with a high spatial coherence pumps the nonlinear medium. A tunable diode laser is then used as a seed. The idler of the parametric interaction then constitutes the THz output. These devices can operate at room temperature and their output is tunable [135, 136]. A pair of rather new mechanisms of the THz radiation generation was reported in 2007. One of them is the generation of the coherent THz radiation in stacks of Josephson junctions under an externally applied dc voltage [137]. The structure makes use of the Josephson effect, namely, an alternating current is flowing back and forth in these junctions at a frequency proportional to the applied voltage and lying in the THz range. The second mechanism is a theoretically predicted narrow-band coherent electromagnetic emission in the THz frequency range from crystalline polarizable materials like NaCl, when they are subjected to a compressive shock wave producing a small strain [138].

So-called large scale facilities like synchrotrons and free electron lasers should be also mentioned. They are sources of a high power coherent electromagnetic radiation emitted by relativistic electron beams traveling through a magnetic structure. Although these sophisticated devices were first aimed for the generation of a higher-frequency radiation and the THz emission was observed as an accompanying effect, they are now intensely used due to their high emitted power in comparison with other sources [139, 140].

Photoconductive switch

Photoconductive switches or photoconductive antennae introduced by Auston et al. [118] were historically the first sources of THz pulses. In this so called Auston switch free carriers are generated in the conduction band of a semiconductor by a femtosecond laser pulse with a photon energy higher than the band gap. The carriers are accelerated under applied electric field and finally they are trapped or they recombine. Such a rapid variation of the current density leads to an emission of a pulse of the THz radiation into the substrate. Far from the emitter the field is proportional to the time derivative of the current density (see Fig. 2.2a). The properties of the semiconductor and geometry of the antenna determine

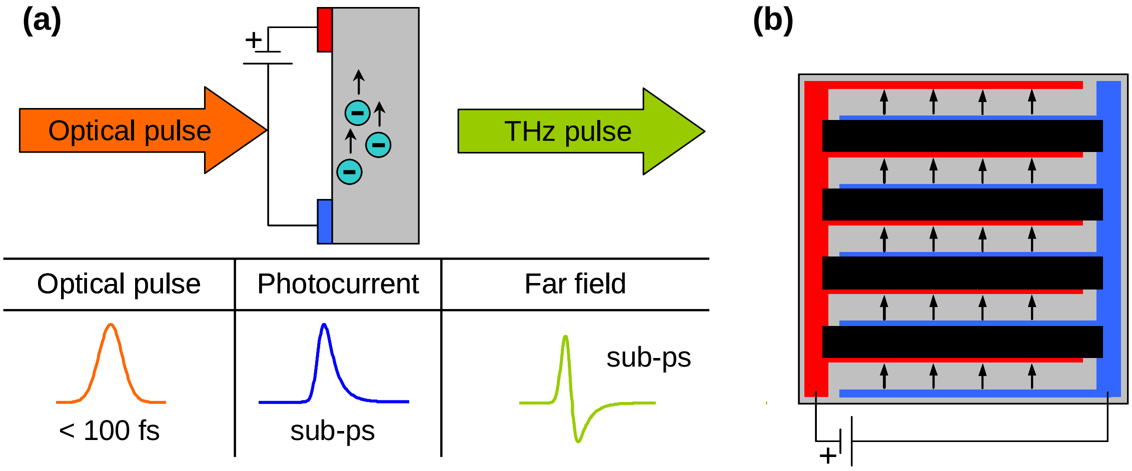

Figure 2.2: **(a)** Schematic illustration of THz pulse generation in a photoconductive switch pumped by femtosecond optical pulses. Semiconductor is shown by gray color, deposited electrodes – by red and blue colors. **(b)** Schematic sketch of THz emitting MSM structure. Opaque metallic shields are shown by black color. The bias electric field direction is indicated by arrows.

the resulting shape of the electromagnetic transients.

The lifetime of free carriers in a semiconductor is very important parameter for this application because the emitter has to reach an initial high-resistivity steady state before the next laser pulse excitation. Therefore semiconductors with an ultrashort carrier lifetime and a high carrier mobility are preferable. Shorter lifetime and higher mobility lead to stronger changes of the current density, and, as a result, the emitted THz pulse is more intense. Moreover, shorter carrier lifetime enhances the output at the high-frequency spectral edge of the emitted radiation. Simultaneously, a dark resistivity of the semiconductor should be as large as possible in order to prevent heating of the emitter. These required properties can be found in specially prepared semiconductor materials like radiation-damaged silicon on sapphire (RD-SOS) [141], low-temperature-grown GaAs [142], Be-doped low-temperature-grown GaAs [143], etc.

Auston switch has a small active area compared to the wavelength of the generated radiation. This source behaves like a point dipole and, consequently, the divergence of the emitted radiation is very large. The first idea of improving the directionality was proposed by van Exter et al. [144] and consisted in attaching lenses to photoswitches in order to collimate the emitted radiation. Later on, a large-aperture emitter scheme was proposed [145, 146]. Here, the active area of the antenna is larger or comparable to the wavelength of the emitted radiation and can be approximated by a superposition of elementary dipoles. Therefore, in this scheme the divergence of THz radiation is significantly reduced. In addition, the emitted power can be increased because a collimated optical beam can be used for the emitter photoexcitation and, in turn, a larger power can be used without damaging the semiconductor and without saturation effects. Under these conditions, electric field of the THz radiation generated by the large-aperture emitter scales linearly with the optical pump fluence [147].

More advanced construction of photoconductive antennae was proposed by Dreyhaupt et al. in 2005 [148]. They presented a large-area emitter consisting of an interdigitated electrode metal-semiconductor-metal (MSM) structure. Every second period of the MSM structure is blocked by an additional electrically isolated metallic layer which prevents the optical excitation of the semiconductor in these parts (Fig. 2.2b). Free carriers are generated only in periods experiencing unidirectional bias electric field. In this case, the whole active area of the device can be understood as a large number of small emitters simultaneously radiating THz light in phase. Therefore, the THz radiation constructively interferes in far field leading to a high THz electric field output. The authors reported THz electric field amplitude up to 85 V/cm under excitation by femtosecond optical pulses with an average power of 100 mW and at a bias voltage of 65 V. An emitter of the same type was used in TDTS setup in the frame of this thesis.

We considered biased photoconductive antennae where photo carriers are accelerated by an externally applied electric field. It has been shown that the surface depletion field in semiconductors can be also exploited for carrier acceleration instead of an external field source [149, 150]. The main difference is that the surface depletion field is normal to the surface of the semiconductor. Hence, arrangements with oblique incidence of the optical excitation beam are required. These emitters are often put to a magnetic field for the enhancement of the radiated power. Typical semiconductors used in this type of emitters are InAs crystals [151] or semi-insulating GaAs crystals [150].

2.1.3 Detection principles

All available detectors of THz radiation can be divided in two groups. The first one is based on sensing the absorbed energy of the THz electromagnetic field. The radiation heats the detector and the change of its temperature is subsequently measured, for example, as a change of the voltage in pyroelectric detectors. Bolometers operating at liquid-helium temperatures show the highest sensitivity. However, their drawback is a rather slow response together with the necessity of their cooling. Acousto-optical Golay cells and some pyroelectrics are able to operate at room temperature. All these devices measure the THz power averaged over many periods of the electromagnetic field. It means that they have an access only to the spectral intensity $I = |E(f)|^2$ but not to the phase of the radiation. The information about the phase can be obtained only when the sample is placed into one arm of an interferometer [152]. In this case, the interferometer records the optical thickness of the sample with frequency and the phase can be extracted.

The second group of detectors is used in the spectroscopic technique implying coherent generation and detection of ultrashort THz pulses. Their huge advantage is the possibility of phase sensing. They allow measuring the amplitude and the phase of any spectral component within a broad THz pulse bandwidth. Therefore, a complex broadband response function can be obtained without using the Kramers-Kronig relations. Photoconductive gating, electro-optic or magneto-optic sampling and THz-induced lensing are the detection schemes allowing to record the complex data. All of them have a common strategy for the reconstruction of the THz wave form (time profile of the pulse). It is a sampling technique triggered by gating optical pulses which are split from the output laser pulse train generating the THz pulses in the emitter. In this way, the emission and detection processes are naturally synchronized. The detected signal depends on a temporal overlap of the THz pulse with the gating optical pulse. By a variation of the optical path length of the gating pulse one can change its arrival time to the sensor and, correspondingly, an instantaneous overlap with the THz pulse. Thereby, the field of the entire THz wave form can be sampled in time.

Detection of THz radiation by a photoconductive antenna implies, in fact, an inverse process to the generation of the THz pulses. The sampling laser pulses generate free carriers in a semiconductor wafer forming the switch. The THz electric field plays the role of an external bias (time dependent accelerating field). The accelerated free carriers produce a current providing a measure of the instantaneous THz field. The photoconductive response of the semiconductor should be ultrafast in order to reproduce the time-domain shape of the THz pulse.

Electro-optic sampling

An electro-optic sampling is a detection technique making use of the linear electro-optic Pockels effect [153], where an externally applied electric voltage induces birefringence of an electro-optic crystal. In this detection method, the THz electric field E_{THz} acts as an external applied voltage in the classical Pockels effect (Fig. 2.3). The presence of the THz electric field in the electro-optic crystal induces the optical birefringence which depends linearly on the field amplitude:

$$\Delta n \propto E_{THz}. \tag{2.2}$$

When the phase matching condition for the THz and optical pulses is fulfilled in the electro-optic crystal, the polarization state of the femtosecond optical pulse is changed correspondingly. The instantaneous THz field can be evaluated from a change of the sampling pulse polarization. The phase shift between the ordinary and extraordinary beams in the electro-optic crystal with thickness L is the following:

$$\Delta\varphi = \frac{\omega}{c}\Delta n L. \tag{2.3}$$

Having passed through the crystal, initial circular polarization of the optical pulse is changed to an elliptical (slightly distorted circular). Subsequently, the beams with horizontal and vertical polarizations are separated by a Wollaston prism and the difference

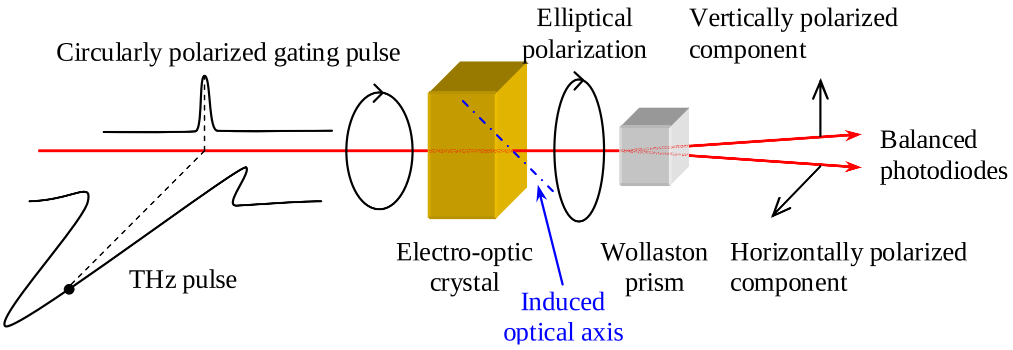

Figure 2.3: Scheme of the electro-optic sampling of the THz pulses with a pair of balanced diodes. After [154]

between their intensities is measured by a pair of balanced photodiodes. Analytically it is written as follows:

$$\Delta I = I_0 \sin \Delta\varphi, \tag{2.4}$$

where I_0 is the intensity of the sampling beam. For small values of $\Delta\varphi$, which are usually met in practice, sin is proportional to its argument with a good precision. Following (2.2), (2.3) and (2.4) one can see that the measured signal is directly proportional to the THz electric field E_{THz}. As the difference signal is modulated by the modulation frequency of the THz radiation it can be reliably detected using a lock-in amplifier. The whole THz wave form can be scanned step by step by changing the time delay between the THz and sampling optical pulses.

Substantial nonlinear response of a material is needed for the electro-optic sampling, and this brings us to the materials which are used as emitters generating the THz pulses by the optical rectification. The most often used crystals in the electro-optic detection scheme are ZnTe, GaP, DAST, $LiTaO_3$, $LiNbO_3$ and GaAs single crystals [155–158].

The magneto-optic sampling and THz induced lensing are methods related to some extent to the electro-optic sampling. The first one has completely analogical scheme to the above discussed technique. The only difference is that for the detection of the THz radiation a magneto-optic property of the sensors is used. The principle of this detection is based on Faraday rotation effect induced by a transient magnetic THz field. Appropriate materials are those having a high magneto-optic coefficient; for example, Bi-substituted yttrium-iron-garnet films and SF-59 amorphous glasses were previously used as sensors [159, 160]. The induced lensing mechanism of the THz radiation detection was proposed by Schneider et al. [161]. It consists in a THz-field-induced focusing or defocusing of the gating laser pulses in an electro-optic crystal. Organic DAST crystals are shown to be of the best choice for this detection mechanism due to their large diagonal electro-optic coefficient.

2.1.4 Time-domain THz spectroscopy

Time-domain THz spectroscopy (TDTS) as a conventional steady-state spectroscopy is used to determine the dielectric or conductive properties of materials. Steady-state THz spectrometers are usually set up for operation in transmission or reflection geometries. We devote a separate discussion to the transmission geometry as it has been used as the main experimental tool throughout this thesis.

The dielectric and conductive contrasts of objects or parts of objects are investigated by terahertz-ray imaging technique which is now driven towards applications in quality control, security and medicine. This is a very promising imaging method owing to the high signal-to-noise ratio and the phase sensitivity of TDTS. Let us also mention the time-resolved application of the THz spectroscopy, so called optical pump-THz probe (OPTP) technique allowing investigation of the transient dynamics in materials.

Schematic layout of the time-domain THz transmission spectrometer used in this thesis is shown in Fig. 2.4. The horizontally polarized beam of femtosecond laser pulses produced by Mira Seed laser system (67 fs long pulses, 76 MHz repetition rate, 8 nJ per pulse, 800 nm, 650 mW average output) is divided by a beam-splitter into pump and sampling beams with corresponding intensities of 96 % and 4 % of the initial beam. The pump beam goes to an emitter and generates the THz radiation. Subsequently, an ellipsoidal mirror focuses this radiation on an investigated sample fixed to a diaphragm and covering the whole aperture. Afterwards, the transmitted THz radiation is focused on the electro-optic sensor by another ellipsoidal mirror. At the same time, the sampling beam passes through an optical delay line and half-wave plate ($\lambda/2$) changing its polarization to vertical. Then it is directed to a sensor: after its reflection on a pellicle beam-splitter (PBS), which is fully transparent for the THz radiation, it propagates colinearly with the THz beam through the sensor crystal. Thereafter, the sampling beam is split in two beams. One of them is going to a reference photodiode (RPD), and the second one propagates through a Soleil-Babinet compensator (SBC), which is, actually, an adjustable quarter-wave plate. In the next step, the circularly polarized sampling beam is spatially separated into the horizontally and vertically polarized beams by a Wollaston prism (WP). The difference between their intensities is measured by two balanced photodiodes. The difference signal, which is, as already discussed, linearly proportional to the THz field, is transferred to a lock-in amplifier synchronized with the frequency of a step-like bias field applied to the emitter. The lock-in amplifier output is normalized by the signal from the reference photodiode. Such electronic normalization minimizes changes of measured wave forms under moderate variations of the laser power. An additional way of increasing the stability of the experiment is realized using an active beam-pointing stabilization, which is not shown in the scheme. The horizontal and vertical offsets of the laser beam position are compensated by tilting of a motorized mirror controlled by signals from a quadrant-photodiode detector.

The part of the experimental setup where the THz pulses propagate is enclosed in a vacuum box. During the experiments the pressure inside the box is maintained below

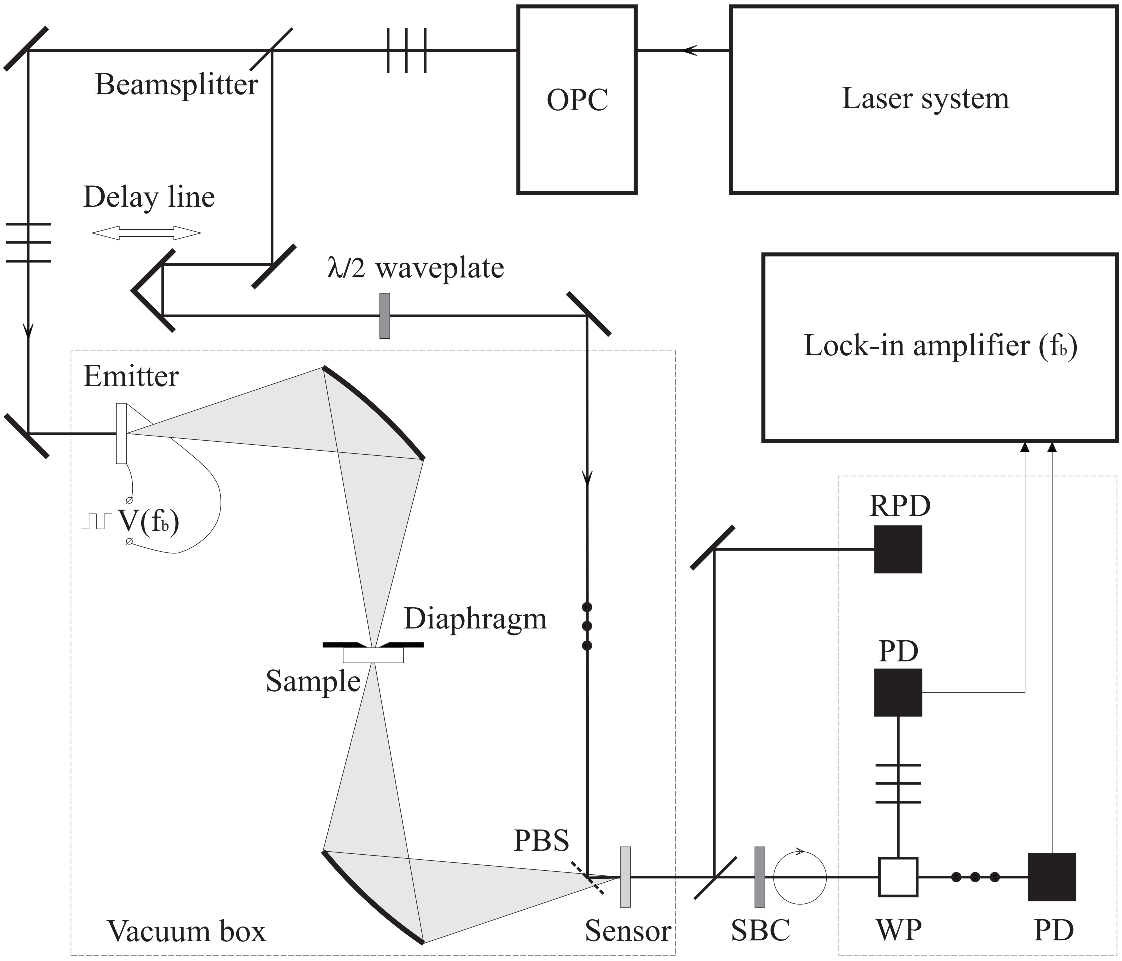

Figure 2.4: Scheme of time-domain THz transmission spectroscopy setup: OPC stands for optical pulses compressor, RPD – reference photodiode, PD – photodiode, WP – Wollaston prism, PBS – pellicle beam-splitter, SBC – Soleil-Babinet compensator.

1 mbar in order to prevent interaction of the THz radiation with water vapor. For the purpose of minimizing the effects of a parasitic light coming to the detection photodiodes they are placed in an optically opaque box. The spectrometer is equipped with liquid He-cooled continuous flow cryostat with thin mylar windows which are well transparent for the THz radiation. Additionally, high-temperature experiments can be carried out using a furnace. Thereby, a very broad temperature range from 10 K to 900 K is accessible in our setup.

The position of the optical delay line is controlled by a computer. Time profile of the THz electric field can be scanned step by step by changing the delay. However, the measured wave form $E_{meas}(t)$ always differs from the true time-profile of the THz field $E_{THz}(t)$. In the case of an ideal dispersion-free electro-optic crystal $E_{meas}(t)$ is a convolution of $E_{THz}(t)$ and the intensity profile of the optical sampling pulse. In reality, the walk-off of THz and optical sampling pulses in the sensor material complicates the situation. In crystals with polar phonon modes substantial difference between the group velocity of the optical pulse and the phase velocity of the THz pulse can be observed. It results in a time walk-off of the pulses propagating through the electro-optic crystal. For example, in (011)-oriented ZnTe crystal with the optical group index $N_g = 3.22$ at $\lambda = 810$ nm and the THz refractive index $n_{THz} \simeq 3.17$ at 1 THz [162] the walk-off t_w is $\sim$161 fs/mm. It means that measurement with a 1 mm-thick sensor will average the value of the THz electric field over $\tau \approx \sqrt{t_p^2 + t_w^2}$, where t_p is the length of the sampling pulse. The THz refractive index in ZnTe increases towards higher frequencies due to a contribution of the first transverse optical (TO) phonon mode lying at 5.3 THz [163], and at some frequency of the THz radiation the group velocity of the optical radiation and the phase velocity of the THz radiation are equal. However, at higher frequencies the THz index increases very steeply and, what is more crucial, the absorption of the THz radiation becomes substantial. Practically, ZnTe sensors are used for the detection of frequencies below 3.5 THz [164]. For higher frequencies, materials such as GaAs [165] or thin plates of GaP [155] offer more suitable properties. Let us consider a GaP crystal to compare it with ZnTe. First of all, its TO phonon mode is at 11 THz: (110)-oriented GaP crystal has the optical group index $N_g = 3.7$ at $\lambda = 800$ nm and the THz refractive index $n_{THz} \simeq 3.35$ at 1 THz [155]. Such values of the indices produce the walk-off as huge as 1.17 ps/mm. However, at 7.5 THz the THz phase velocity is equal to the optical group one for 800-nm light. Thus, in order to get a broadband response using GaP sensor one has to reduce its thickness. On the other hand, reducing the thickness leads to a linear reduction of the signal amplitude according to (2.3) and (2.4). Moreover, the electro-optic coefficient of GaP is lower than that of ZnTe. Therefore one has to find a trade-off between the broadband response and the signal amplitude.

During my thesis we modified the experimental setup in order to achieve a broader spectral range. Just behind the laser oscillator we installed a compressor of the optical laser pulses (OPC). It compresses the optical pulses using multiple reflections on a pair of mirrors with negative dispersion (NDM). In our case, an internal geometry of the compressor was adjusted to obtain 16 reflections of the optical pulse on NDMs. Having passed through the compressor the initial 67-fs-long optical pulses are compressed to 35-fs-long pulses. In this case, the chirp of the output of the OPC is slightly “overcompensated” (i.e., the optical pulses possess negative chirp, the short-wavelength part of the pulse is ahead of the long-wavelength part). As a result, the optical pulse length was minimized to 32 fs near the THz emitter due to some positive contributions to the chirp in the optical components directing the beam to the emitter.

Afterwards we compared 1-mm-thick (011)-oriented ZnTe crystal as a sensor with 150-µm-thick (110)-oriented GaP layer in optical contact with a 1-mm-thick (100)-oriented GaP crystal. In the case of GaP sensor only (110)-oriented part of the material has a

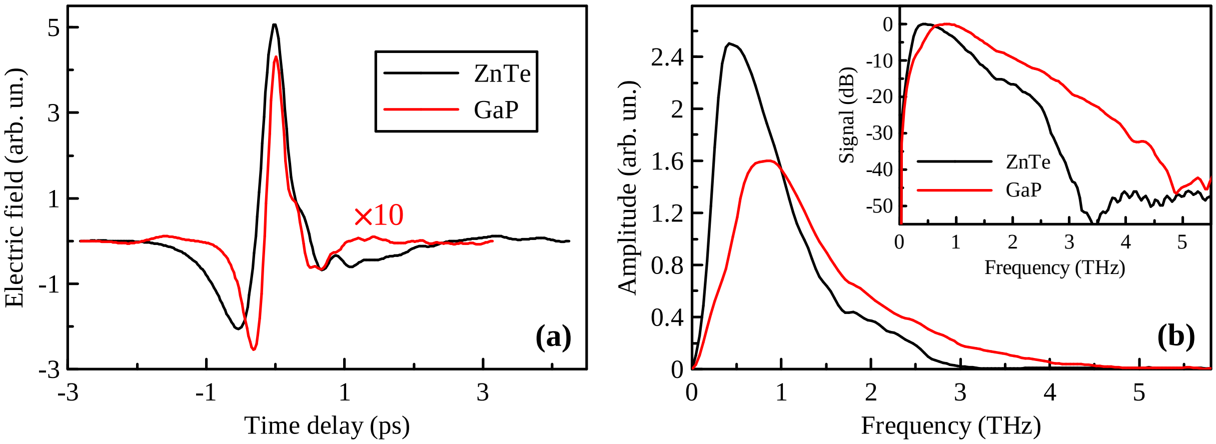

Figure 2.5: **(a)** THz wave forms generated by the same emitter and detected using ZnTe and GaP electro-optic sensors. **(b)** Amplitude spectra corresponding to the wave forms shown in Figure **(a)**. Inset: Spectra in dB.

non-zero electro-optic response and the other part does not sense the transverse THz field and plays the role of an inactive substrate. The THz wave forms generated by the same emitter under the same conditions and detected using the two sensors are shown in Fig. 2.5a. One can see that the wave form detected by the GaP crystal is shorter in time which implies a broader frequency band. Indeed, a direct comparison of amplitudes (see Fig. 2.5b) obtained by Fourier transformation confirms the broader spectral band of the signal detected by GaP, however, it is for the price of a lower signal. Attenuation of both signals shown in the inset of Fig. 2.5b makes it clear that in our setup the ZnTe electro-optic sensor is efficient up to 3 THz while the GaP sensor allows detection up to 4.8 THz.

2.1.5 Data analysis

The spectroscopic method in the transmission geometry involves measurement of a reference wave form $E^{ref}_{meas}(t)$ without any sample or with a known reference sample and a signal wave form $E^{sign}_{meas}(t)$ with the investigated sample. As already mentioned, these measured wave forms $E_{meas}(t)$ are related to the emitted THz transients $E_{emitt}(t)$ by a convolution with some instrumental function $\Psi(t)$:

$$E_{meas}(t) = E_{emitt}(t) * \Psi(t). \tag{2.5}$$

This is strictly true if we can neglect the scattering on inhomogeneities of the sample, on irregularities of its surface and the diffraction on aperture edges. As far as we are considering a steady-state (or equilibrium) experiment, when the sample properties are time independent, the convolution transforms to a simple product in the Fourier (frequency) space:

$$E_{meas}(f) = E_{emitt}(f)\Psi(f). \tag{2.6}$$

$\Psi(f)$ includes propagation of the THz transients before the sample $\Psi_0(f)$, through the sample $T(f)$, after the sample $\Psi_1(f)$ and a sensor response $\Psi_2(f)$:

$$\Psi(f) = \Psi_0(f)T(f)\Psi_1(f)\Psi_2(f). \tag{2.7}$$

Actually, $\Psi_0(f)$, $\Psi_1(f)$, $\Psi_2(f)$ are instrumental functions acquiring the same values in the measurements of the reference and signal wave forms. Therefore, they cancel out when the complex transmission function of the sample $t(f)$ is calculated:

$$\frac{E_{meas}^{sign}(f)}{E_{meas}^{ref}(f)} = \frac{E_{emitt}(t)\Psi_0(f)T(f)\Psi_1(f)\Psi_2(f)}{E_{emitt}(t)\Psi_0(f)T_0(f)\Psi_1(f)\Psi_2(f)} = \frac{T(f)}{T_0(f)} = t(f), \tag{2.8}$$

where $T_0(f)$ is a reference transmission function and its form depends on how the reference is measured.

The complex transmission function $t(f)$ provides an access to the dielectric properties of the sample via the complex refraction index $N(f) = n(f) + ik(f)$.

Plane-parallel slabs

Let us consider a homogeneous sample in a form of a plane-parallel dielectric slab. The reference measurement is then usually performed with the sample removed from the beam path $[T_0(f) = \exp(2\pi i f d/c)]$. In this case the complex transmission function can be written analytically:

$$t(f) = \sum_{j=0}^{m} t_j(f) = \frac{4N\exp\left[2\pi i f(N-1)d/c\right]}{(N+1)^2} \sum_{j=0}^{m} \left\{ \left(\frac{N-1}{N+1}\right) \exp\left[2\pi i f N d/c\right] \right\}^{2j}, \tag{2.9}$$

where d is the sample thickness, c is the speed of light in vacuum, m is the number of internal double reflections (echoes) in the sample and $t_j(f)$ are individual contributions of the internal reflections ($j \neq 0$) or of a direct pass ($j = 0$). For optically thick samples ($nd > 0.6$ mm) these internal reflections are experimentally resolved in time. They present separate delayed pulses in the measured signal and the value of the coefficient m in expression (2.9) can be easily determined. One can also apply a time-windowing procedure consisting in a calculation of the Fourier spectra of individual echoes which can be then identified with $t_j(f)$. An example of measured reference and signal wave forms is shown in Fig. 2.6. In this case a plane-parallel slab of $DyScO_3$ single crystal with a thickness of 949 µm was measured. The direct pass of the THz signal and the internal echoes are nicely resolved in time. The first echo is delayed by approximately 28 ps more than the directly transmitted signal.

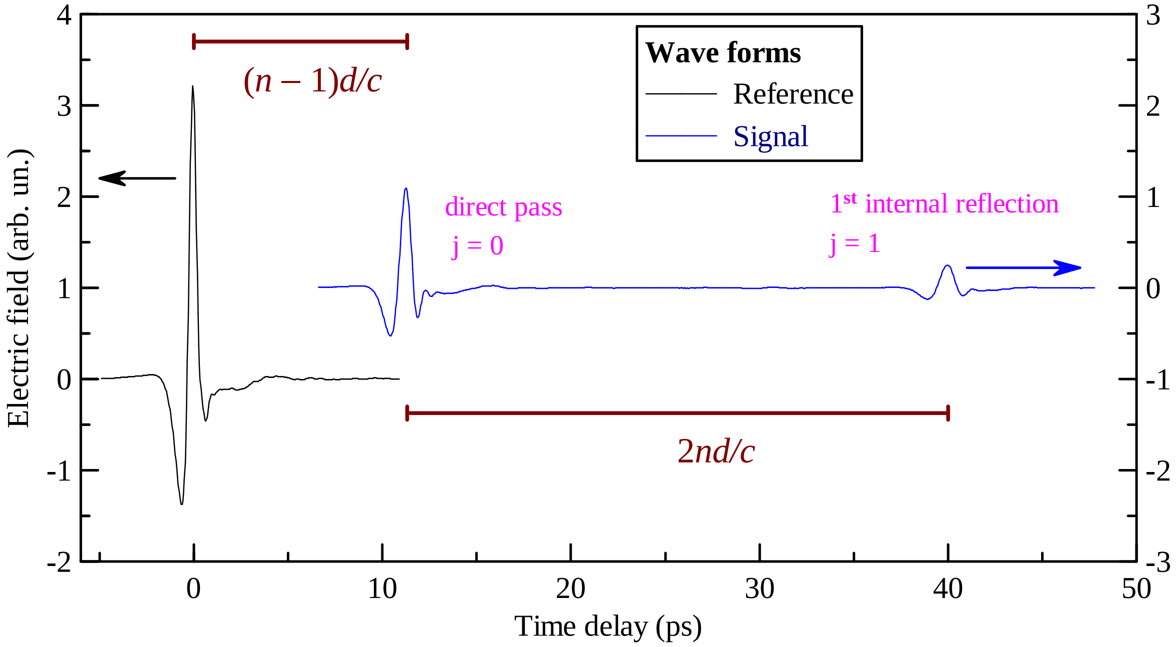

Figure 2.6: Example of measured reference and signal wave forms. The signal wave form is measured with a plane-parallel slab of 949-µm-thick $DyScO_3$ single crystal.

If the sample is optically thin there is no possibility to resolve the internal reflections and the summation in expression (2.9) should go to infinity:

$$t(f) = \frac{4N}{(N+1)^2} \cdot \frac{\exp\left[2\pi i f (N-1) d/c\right]}{1 - \left(\frac{N-1}{N+1} \exp\left[2\pi i f N d/c\right]\right)^2}. \tag{2.10}$$

Equations (2.9) and (2.10) both constitute two real equations for real parameters n and k. In the case of an optically thick sample, the time-windowing is frequently applied, because extracting of $N(f)$ from $t_j(f)$ is much simpler and less sensitive to measurement errors than from $t(f)$. In any case the equations have to be numerically solved. A fast and reliable method of the numerical solution has been described for example in [166].

The presence of a complex exponential function in the equations (2.9) and (2.10) leads to an ambiguity in the phase by $2m\pi$. Multiple mathematical solutions then can be found. Often the physically correct solution can be found from the time delay between the signal and reference pulses (see Fig. 2.6). Sometimes, in spectral ranges with low transmittance and for samples exhibiting sharp resonance, the selection can be problematic. Then, a measurement of two samples with different thickness or employment of Kramers-Kronig relations [167, 168] can help to recognize the correct branch of the solution.

Thin films

THz transmission spectroscopy allows studying the dielectric properties of thin films on transparent substrates. One has to proceed in a similar way as in the case of a dielectric slab with the only difference that the reference measurement should be performed with a bare substrate. Analytically a thin film on a substrate has to be treated as a two-layer system. One of the layers is the thin film and all internal double reflections should be taken into account in the expression for the transmission function. The other layer is the substrate with the optical thickness usually chosen in a way to have the directly passed signal well separated from the first echo. The complex refractive index of the film N_f can be calculated by numerically solving an equation for the complex transmission of the two-layer system which in this case reads:

$$t_f(f) = \frac{2N_f(N_s+1)\exp\left[2\pi i f(N_s-1)(d_s-d_s^r)/c\right]\exp\left[2\pi i f(N_f-1)d_f/c\right]}{(N_f+1)(N_f+N_s)-(N_f-1)(N_f-N_s)\exp\left[4\pi i N_f d_f/c\right]}, \tag{2.11}$$

where d_f is the film thickness, N_s is a complex refractive index of the substrate, d_s and d_s^r are thicknesses of the substrate with and without the thin film, respectively. Usually the film is optically very thin, it means that $2\pi N_f d_f/c \ll 1$. Using this approximation one can simplify equation (2.11) and obtain explicit analytical expression for the complex refractive index of the film [169]:

$$N_f^2 = \frac{ic(N_s+1)}{2\pi f d_f}\left[\frac{1}{t_f(f)}\frac{\exp\left[2\pi i f(N_s-1)(d_s-d_s^r)/c\right]}{1+2\pi i f d_f/c}-1\right]-N_s. \tag{2.12}$$

Thin films in electric field

Investigation of electric-field-induced changes of the dielectric function of thin films is also possible using the THz transmission spectroscopy. In this case, the reference signal $E^{ref}(t)$ is a wave form measured with a thin film sample and with an electric field off, and the signal wave form $E^{sign}(t)$ is measured with the electric field on. The field-induced refractive index N_f^E of the thin film is then calculated by inverting the following expression for the transmission function:

$$\begin{aligned} t_f^E(f) = {} & \frac{N_f^E}{N_f} \\ & \times \frac{(N_f+1)(N_f+N_s)\exp\left[-2\pi i f N_f d_f/c\right]+(1-N_f)(N_f-N_s)\exp\left[2\pi i f N_f d_f/c\right]}{(N_f^E+1)(N_f^E+N_s)\exp\left[-2\pi i N_f^E d_f/c\right]+(1-N_f^E)(N_f^E-N_s)\exp\left[2\pi i N_f^E d_f/c\right]}. \end{aligned} \tag{2.13}$$

Experimental errors

The precision of the output data critically depends on the determination of the film and substrate thicknesses. The film thickness d_f appears in the denominator of (2.12). It nearly directly scales the value of the dielectric constant. An error in the d_f determination distorts the soft-mode strength. However, the value of the soft-mode frequency and of its damping are not influenced by this error.

The phase change of the THz signal due to its propagation through the substrate is much larger than that due to the propagation through the thin film. Therefore, the uncertainty in the phase of $t_f(f)$ coming from the substrate should be minimized; from equation (2.11) one can obtain:

$$\frac{\Delta N_f}{N_f} > \frac{N_s}{N_f}\frac{\Delta d_s}{d_f} + \frac{|d_s - d_s^r|}{d_f}\frac{\Delta N_s}{N_f}, \tag{2.14}$$

where Δd_s is an error in the substrate thickness determination and ΔN_s is the uncertainty in the substrate refractive index. From this inequality we can conclude that the dielectric properties of the thin films are determined with a better precision in the regions where N_f is large (e.g. near a resonance or below a strongly polar resonance with a very high contribution to the permittivity like ferroelectric soft mode) than in the regions with a small N_f (e.g. regions of transparency in non-ferroelectric films). The precision also increases when the film thickness increases. A special care should be devoted to the substrate preparation: it should be a highly plane-parallel slab and its thickness should be accurately determined.

There are two ways of minimizing of this error. The first one consists in a deposition of the film onto a part of the substrate plate while another part (uncoated) serves as a reference substrate.

The second possibility of the error minimization is a terahertz thickness optimization. It is usually done before the deposition of a film during the measuring of the substrate refractive index. One can determine arrival time of the transmitted THz pulse for a set of substrates. This can be done with a precision of 1-2 ps. As these substrates have identical refractive index N_s, the difference between the arrival times among substrates originates from the differences in their thicknesses: $\Delta t = n_s \Delta d_s / c$. In this way we can determine the thickness differences with a precision of $\Delta d_s \approx 200$ nm.

Let us consider a 100-nm-thick $SrTiO_3$ film deposited on $DyScO_3$ single crystal. If the thickness of the substrate is determined mechanically with an error of 1 μm the relative error $\Delta N_f / N_f$ of the film index determination is about 130 %. However, the THz thickness optimization yielding an error of 0.2 μm gives 26 % error in the determination of the film index. In the case of the film thickness of 200 nm the resulting relative error reduces down to 13 % only.

In some cases the experimentalist is supplied with a thin film sample and none of the above procedures can be applied. In this situation the phase uncertainty of $t_f(f)$ is usually too large, but the qualitative shape of $N_f(f)$ remains correct. In such situation it may be useful to disregard the phase and to fit the amplitude of $t_f(f)$ by a model, e.g., together with the Fourier transform infrared transmission or reflection data [169].

A time-domain THz spectrometer arranged in the phase-sensitive reflection geometry [170] can be also suitable for the characterization of thin films as it overcomes the phase problem in the substrate. The THz transients reflected from the sample probe mainly the dielectric properties of the film and they are completely insensitive to the uncertainty in the substrate thickness.

2.2 Fourier transform infrared spectroscopy

Fourier transform infrared (FTIR) spectroscopy is an experimental technique able to acquire spectra in a very broad frequency range from near to far infrared (IR) (10000-20 cm^{-1}). In contrast to dispersive instruments like grating- or prism-based spectrometers the FTIR technique detects the signal at all frequencies simultaneously. It is so-called Fellgett advantage of FTIR spectrometers. This is possible because the method implies the recording of an interferogram from which the power spectrum is calculated by performing Fourier transformation [51,152,171]. High achievable spectral resolution ($0.05-0.1$ cm^{-1}), short time of spectra acquisition and high signal-to-noise ratio make FTIR spectroscopy one of the main tools for IR spectroscopic investigations of solids.

A lot of different FTIR spectrometers are commercially available but all of them operate according to the same principles. FTIR spectrometers are typically based on a Michelson interferometer Fig. 2.7a. It consists of an IR radiation source, a beam splitter, a fixed mirror and a moving mirror. Some spectrometers are set up in a way where the two branches of the Michelson interferometer are ended with a common moving mirror which is an optical element with the mirror surface on both sides as depicted in Fig. 2.7b. The

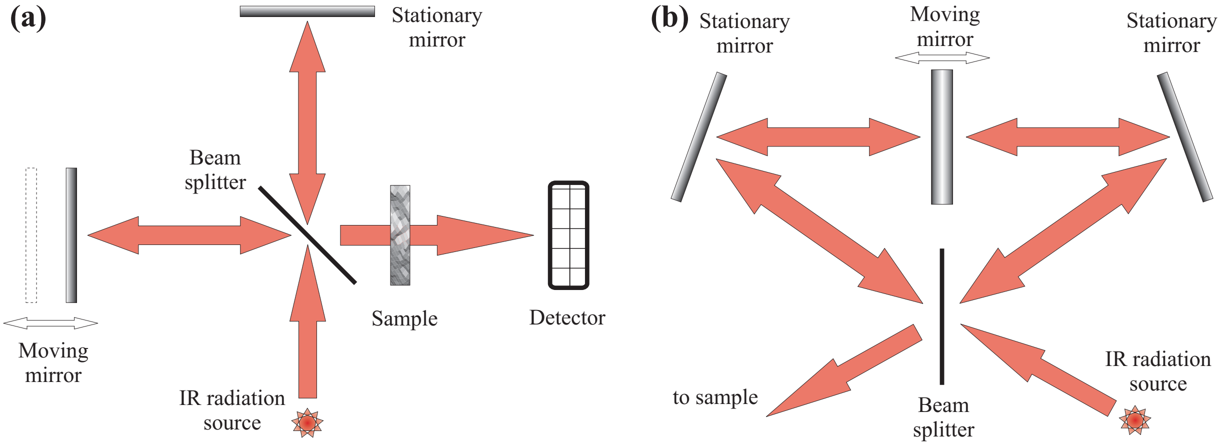

Figure 2.7: Schematic layouts of FTIR spectrometers based on a Michelson interferometer **(a)** and on a Genzel interferometer **(b)**

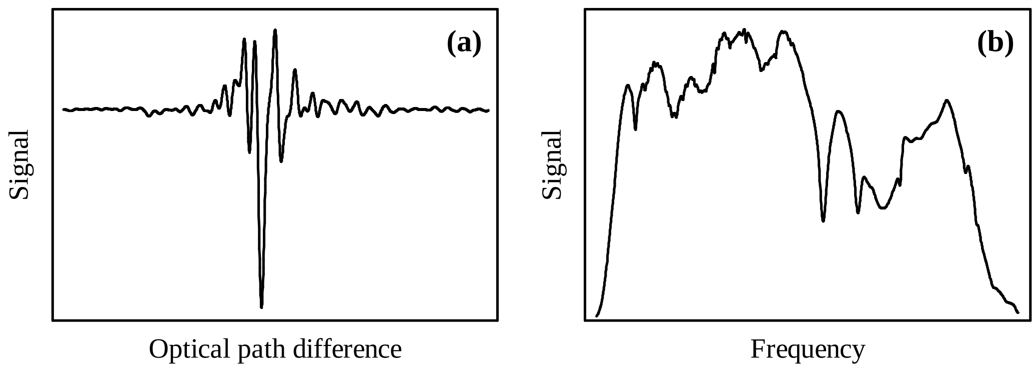

Figure 2.8: Example of an interferogram (a) and a corresponding reflectivity spectrum (b) measured by a FTIR spectrometer with a mirror as a sample. The data are kindly provided by D. Nuzhnyy.

mercury arc lamp or the SiC (globar) rod play the role of the radiation source. The beam splitter is made of a special material in a way to have one half of initial radiation intensity transmitted and the other half reflected. Different materials such as coated mylar and metal grids are used for different parts of IR band. At the output of the interferometer the two beams recombine and propagate colinearly through the sample towards the detector. Deuterated triglycine sulfate (DTGS) pyroelectric detectors and helium-cooled silicon bolometers are widely used as detectors in FTIR spectrometers.

The spectroscopic method consists in detecting the IR radiation power versus the optical path difference (position of the movable mirror). This dependence is called interferogram. Usually, it has a complex form (see Fig. 2.8a) since it involves a lot of different wavelengths transmitted with different amplitudes. The recorded interferogram has to be transformed into a spectrum using the fast Fourier transformation (FFT) algorithm. An example of the power reflection spectrum obtained by a FTIR spectrometer with a metallic mirror as a sample and the corresponding interferogram are shown in Fig. 2.8. The spectral content of the interferogram depends on the power spectrum of the source, on the properties of the beam splitter and on the step and length of the interferogram scan. The high-frequency limit of the spectrum may be increased by decreasing the step of the scan. The spectral resolution is simply an inverse of the achievable optical path difference. For example, an instrument with a 2 cm scan length can achieve 0.5 cm^{-1} spectral resolution. Transmission and/or reflection functions then can be obtained as the ratio of sample and reference spectra like in the case of TDTS. Nevertheless, typical FTIR spectrometer provides only power spectra in contrast to TDTS. FTIR spectroscopy can be made phase-sensitive if the sample is placed in the interferometer arm with the fixed mirror. However, spectrometers with such arrangement are not available commercially owing to numerous technical difficulties.

2.2.1 Data analysis

Two most common ways of extracting the information about the complex refractive index of the sample are used. Since the output data of a typical FTIR measurement are power spectra without the information about the phase one has to find an approach with additional assumptions. The first way is based on an assumption that the measured spectrum is broad enough to perform the Kramers-Kronig analysis with the permittivity $\varepsilon(\omega) = \varepsilon'(\omega) + i\varepsilon''(\omega)$ [171]:

$$\varepsilon'(\omega) - \varepsilon_\infty = \frac{2}{\pi} P \int_0^\infty \frac{\omega' \varepsilon''(\omega')}{\omega'^2 - \omega^2} \, \mathrm{d}\omega', \tag{2.15}$$

$$\varepsilon''(\omega) = -\frac{2\omega}{\pi} P \int_0^\infty \frac{\varepsilon'(\omega') - \varepsilon_\infty}{\omega'^2 - \omega^2} \, \mathrm{d}\omega', \tag{2.16}$$

where P means the principal value of the integral and ε_∞ is a contribution to the permittivity due to higher frequency polarization processes. The phase $\phi(\omega)$ of the reflectivity $R(\omega)$ can be calculated using the following equation

$$\phi(\omega) = \frac{\omega}{\pi} P \int_0^\infty \frac{\ln R(\omega') - \ln R(\omega)}{\omega^2 - \omega'^2} \, \mathrm{d}\omega'. \tag{2.17}$$

Using the phase one can now compute the complex refractive index $N(\omega) = n(\omega) + ik(\omega)$ of the sample

$$n(\omega) = \frac{1 - R(\omega)}{1 + R(\omega) - 2R(\omega)^{1/2} \cos\phi(\omega)}, \tag{2.18}$$

$$k(\omega) = \frac{2R(\omega)^{1/2} \sin\phi(\omega)}{1 + R(\omega) - 2R(\omega)^{1/2} \cos\phi(\omega)}. \tag{2.19}$$

In practice, however, $R(\omega)$ is known only in a limited frequency interval $\omega_1 \leq \omega \leq \omega_2$, and a suitable extrapolation must be introduced outside this range.

The second way consists in modeling the dielectric response of the sample by analytical models. The power reflectance under normal incidence expressed through the permittivity reads

$$R(\omega) = \left| \frac{\sqrt{\varepsilon(\omega)} - 1}{\sqrt{\varepsilon(\omega)} + 1} \right|^2. \tag{2.20}$$

The most common model used for the description of the dielectric contribution of polar phonon modes has the form of a sum of m classical harmonic oscillators

$$\varepsilon(\omega) = \sum_{j=1}^{m} \frac{\Delta\varepsilon_j \omega_{TO_j}^2}{\omega_{TO_j}^2 - \omega^2 - i\omega\gamma_{TO_j}} + \varepsilon_\infty; \tag{2.21}$$

a more general so-called factorized form reads [172]

$$\varepsilon(\omega) = \varepsilon_\infty \prod_{j=1}^{m} \frac{\omega_{LO_j}^2 - \omega^2 - i\omega\gamma_{LO_j}}{\omega_{TO_j}^2 - \omega^2 - i\omega\gamma_{TO_j}}, \tag{2.22}$$

where ω_{TO_j} and ω_{LO_j} are the transverse and longitudinal frequencies of j^{th} polar phonon mode, respectively, γ_{TO_j} and γ_{LO_j} are their respective damping constants and $\Delta\varepsilon_j$ is the j^{th} mode contribution to the static permittivity. The values of these parameters are found from the fit of measured reflection or transmission functions by expressions (2.21) or (2.22).

The classical oscillator model (2.21) includes three fitting parameters for each harmonic oscillator. It clearly separates the contribution to the permittivity of each polar process. However, this model is not general and in some cases it fails to describe the spectra correctly. It happens namely in the case of a large LO-TO splitting ($\omega_{LO_j} \gg \omega_{TO_j}$) where the damping constants γ_{LO_j} and γ_{TO_j} can possess different values leading to asymmetric resonances in the spectra. In this case the factorized (four-parameter) model (2.22) usually gives a better fit. The model (2.22) provides the most general expression for a linear dielectric response with the given number of transverse [poles of (2.22)] and longitudinal [zeros of (2.22)] resonances. On the other hand, using the four-parameter model one has to keep in mind that the fit can sometimes result in a combination of parameter values giving unphysical properties like negative losses. Therefore, the model is accompanied by necessary conditions imposed on its parameters

$$\omega_{LO_j} > \omega_{TO_j}, \qquad \gamma_{LO_j} \geq \gamma_{TO_j}, \qquad \frac{\omega_{LO_j}^2}{\omega_{TO_j}^2} \geq \frac{\gamma_{LO_j}}{\gamma_{TO_j}}. \tag{2.23}$$

The fitting method for extraction of the dielectric properties is more advantageous than the Kramers-Kronig analysis because the resulting parameters of polar phonon modes can be directly compared with the data obtained by other spectroscopic techniques. In addition, the fit quality can be improved by including into the data to be fit a directly measured complex permittivity in THz and/or GHz range.

Far-infrared reflectivity measurements presented in this thesis were performed using a Fourier transform spectrometer Bruker 113v with a He-cooled silicon bolometer or DTGS detectors. The spectrometer is equipped with a continuous-flow-helium cryostat allowing low-temperature measurements down to 5 K.

Chapter 3

Results on bulk materials

Incipient ferroelectrics

The presence of a ferroelectric phase transition (PT) in dielectrics is determined by a competition between cooperative long-range forces trying to order the system and fluctuations tending to break the order. In the case when the transition occurs at high temperature, i.e., in the classical regime, thermal fluctuations play the role of a disruptive force. However, on cooling the fluctuations decrease and eventually the ordering forces become dominating. If the transition occurs at sufficiently low temperatures, quantum fluctuations (or zero point motions) can strongly influence the response of the system [2].

The early evidence for some quantum effects was seen in two perovskites $SrTiO_3$ and $KTaO_3$ which have been considered for microwave applications. These two crystals actually do not undergo the ferroelectric phase transition but are just barely stable against their ferroelectric soft mode near 0 K. Therefore, they are referred to as incipient ferroelectrics. The permittivity of these crystals deviates markedly from the Curie-Weiss law (1.1) and saturates at low temperatures. Barrett [173] described this deviation in terms of a model based on a mean-field quantum-statistical ensemble of anharmonic oscillators. According to this model the permittivity reads

$$\varepsilon = \varepsilon_b + \frac{C}{\frac{T_1}{2}\coth\frac{T_1}{2T} - T_0}, \tag{3.1}$$

where, T_1 denotes the temperature at which the quantum fluctuations start to play a role and ε_b is the temperature-independent part of the permittivity. This equation turns out to be the Curie-Weiss law in the $T \gg T_1$ limit.

$KTaO_3$ single crystals

Potassium tantalate (KTO) stays in the cubic structure with the space group $Pm\bar{3}m$ at all temperatures. The dielectric constant rises to large values on cooling but appears to saturate at a value of about 4500 [174] at liquid helium temperatures. Below about 30 K the permittivity follows the Barrett equation (3.1) quite well with $\varepsilon_b = 47.5, C = 4.45 \times 10^4$ K, $T_1 = 56.9$ K, and $T_0 = 13.1$ K [2]. The low-temperature paraelectric phase is rather unstable and the ferroelectric phase transition can be induced in different ways, for example, by doping [23, 175], by uniaxial stress [176] or by biaxial strain [66].

The temperature dependence of KTO permittivity is mainly governed by a contribution of the lowest-frequency polar phonon (soft mode) whose eigenfrequency softening is at the origin of the observed permittivity increase. Below the soft-mode frequency which is in the THz range, no dielectric relaxation is observed [177]. In the case there are no defects in the crystal structure, the dielectric losses in the microwave (MW) range are due to the intrinsic phonon absorption. All these properties make KTO a good candidate for tunable microwave applications.

3.1 $KTaO_3$ ceramics

Despite the fact that KTO single crystals have been intensely investigated since 1960s, the study of the ceramics has started only recently [178–180]. This delay was caused by challenges in the preparation of KTO ceramic samples. The main difficulties are a hygroscopic nature of starting compounds, a sublimation of potassium species upon heating, and a strongly covalent character of the Ta-O bond inhibiting the diffusion process. As a consequence, the exact stoichiometry of samples, their chemical and structural homogeneity as well as high density are hardly achievable. Nevertheless, good quality ceramics have been prepared recently [179, 180]. Their grain size is in the micrometer range, and their radio-frequency (RF) permittivity has a low-temperature plateau with the dielectric constant value of ∼4000, which is very close to that in KTO single crystals.

The effect of the grain size on the dielectric properties was investigated in several other high-permittivity perovskites [181]. The most interesting previously studied compound is high-density $SrTiO_3$ ceramics. Its low-temperature permittivity has never exceeded ∼10000, which is less than one half of the averaged value of anisotropic $SrTiO_3$ single crystals (∼25000) [57, 182, 183]. Moreover, it was found that the low-temperature permittivity value strongly decreases with the grain size decrease. For example, the value of only 700 is reached in the case of the spark plasma sintered ceramics with the grain size of ∼80 nm. Petzelt and co-workers [57, 182] concluded that the permittivity drop is directly related to a stiffening of the soft-mode frequency. This dielectric grain size effect was microscopically attributed to the presence of low-permittivity polar grain boundaries, whose permittivity is reduced due to the O-deficiency. In other words, this is an effect of the effective medium response. The high values of the permittivity observed in KTO ceramics imply a much smaller or negligible grain size effect.

In this part of the work we performed a broadband dielectric characterization of KTO ceramics. The results were obtained in a collaboration with colleagues from Slovenia (Jožef

Stefan institute in Ljubljana) who prepared the samples and provided their structural and chemical analysis [184]. The dielectric characterization of the ceramics was performed in the Department of Dielectrics in the Institute of Physics in Prague. IR measurements were done by D. Nuzhnyy, and MW measurements were done by M. Kempa and V. Bovtun. Though my contribution to this study consists of the dielectric characterization of the material in the THz spectral range, this investigation is included in the thesis because the ceramics seem to be very interesting from a point of view of a possible tunability of their dielectric properties.

3.1.1 Sample preparation

KTO ceramics were prepared from mechanochemically activated stoichiometric K_2CO_3-Ta_2O_5 powder mixtures. A double heating at 800 °C for 4 h was performed to obtain perovskite powders with good structural homogeneity. Afterwards, the powder compacts were packed in a coarse MgO powder in an alumina die and hot-pressed at 1250 °C for 2 h [179]. The XRD analysis indicated that the obtained ceramics were phase-pure perovskite. The compound contained 900 ppm and 71 ppm of W and Co impurities, respectively, both originating from the wear of the milling vial and balls. The density of the sintered pellets was 6.87 g/cm^3 corresponding to a relative density of 98 %.

Fractured surface of the obtained ceramics was investigated using a field-emission electron scanning microscope. It showed a bimodal distribution of the grain size, with small grains occupying the regions between large grains. The size of the small grains is ranging from ∼100 nm to ∼500 nm, while the larger grains can exceed 3 µm in size. Cylindrical samples with the diameter of ∼6 mm were mechanically polished in order to obtain thicknesses appropriate for individual experimental techniques (∼70 µm for the MW and THz and ∼300 µm for the IR measurements).

3.1.2 Results and discussion

The IR reflectivity spectrum of KTO ceramics together with the reflectivity spectrum calculated using the measured THz transmission data is shown in Fig. 3.1a. A simultaneous fit of the IR reflectivity spectra and the complex THz permittivity spectra was performed. The measured reflectivity with normal incidence on a sample is related to the complex dielectric function by equation (2.20), where, for the modeling of the complex permittivity the generalized four-parameter model (2.22) was used. The temperature independent value of 4.3 [185] was taken for the high-frequency electronic polarization.

A good agreement between the experimental data and the fits is seen in Fig. 3.1b. The obtained values of the fit parameters were then used to calculate ε' and ε'' spectra which are presented in Figs. 3.1c,d, along with the directly calculated THz permittivity spectra. The three polar phonons (TO1, TO2 and TO4) allowed in the cubic $Pm\bar{3}m$ structure are observed as distinct resonances in the complex permittivity spectra (Figs. 3.1c,d) and correspond to the three most pronounced reflection bands (Figs. 3.1a,b). An additional band is present in the reflectivity spectrum at 761 cm^{-1}. It is a combination band of the TO2 + TO4 modes, and it does not correspond to any fundamental vibration mode. The position of all modes are in agreement with the IR literature data on KTO single crystals [185,186]. The resonance corresponding to the TO1 mode is the most pronounced

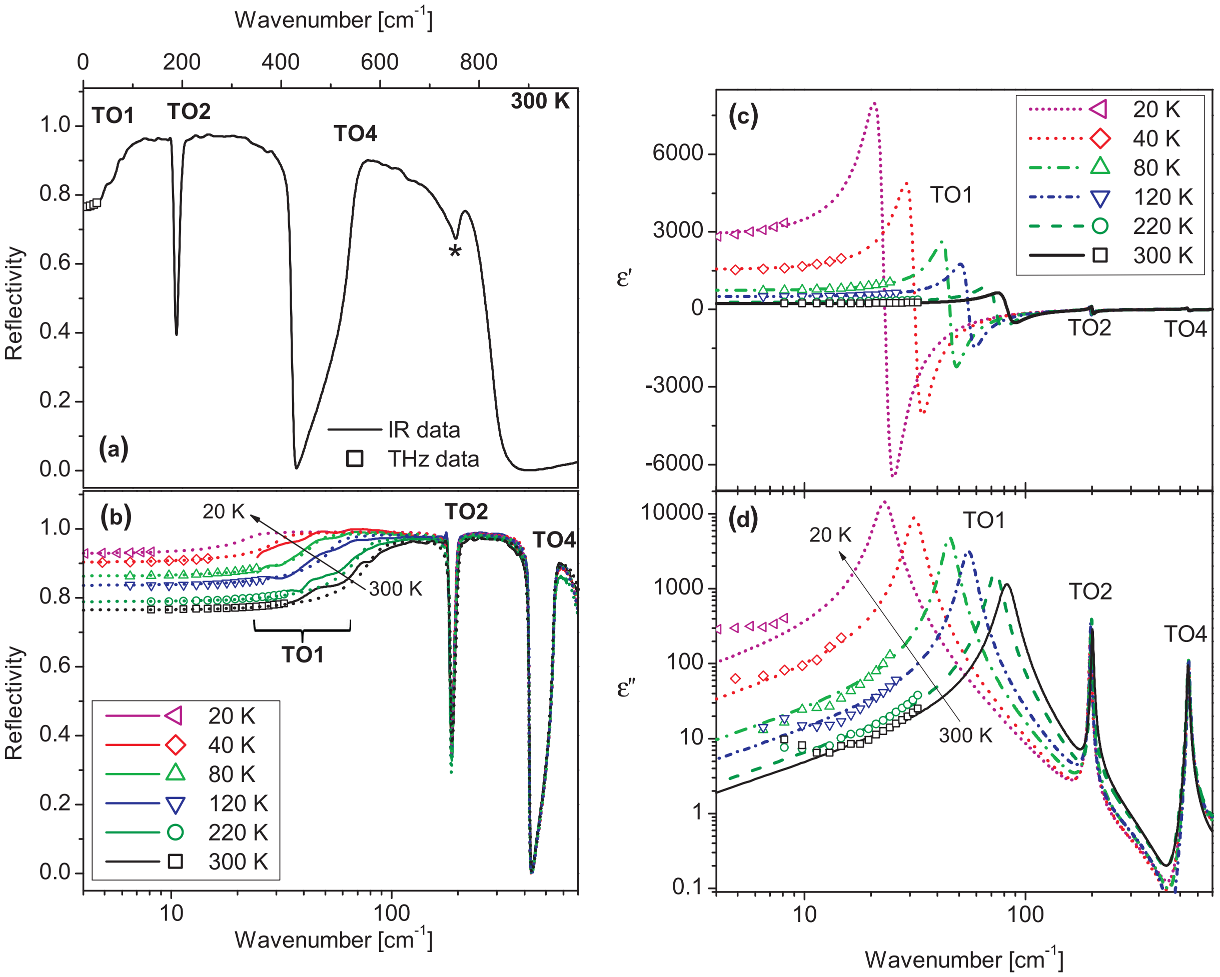

Figure 3.1: **(a,b)** IR reflectivity spectra (solid lines) together with the reflectivity calculated from THz transmission data (symbols) of KTO ceramics measured at 300 K **(a)** and at selected temperatures in the 20−300 K range **(b)**. Approximate positions of the TO1, TO2, and TO4 polar modes are marked. In **(b)** the experimental data are compared to the fits (dashed lines). Two phonon combination band is marked by $*$. **(c,d)** Real ε' and imaginary ε'' parts of the complex dielectric function of KTO ceramics calculated from the simultaneous fits of IR and THz data (symbols).

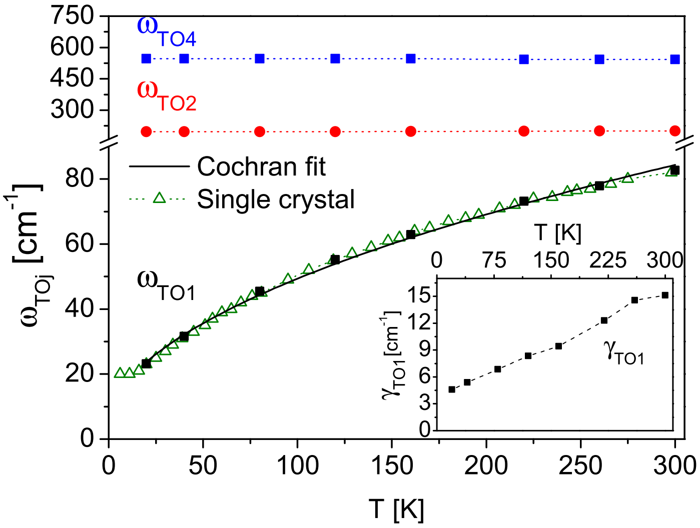

Figure 3.2: Temperature dependences of the $\omega_{\mathrm{TO1}}, \omega_{\mathrm{TO2}}$, and ω_{TO3} polar phonon frequencies. The solid black line represents a fit of ω_{TO1} data by the Cochran law (1.6); the dotted lines are guides to the eye. The single crystal ω_{TO1} data from the hyper-Raman studies [187] are shown for comparison. Inset: temperature dependence of the TO1 mode damping constant γ_{TO1}.

one in the spectra and its dielectric strength strongly increases on cooling.

The temperature dependence of the phonon eigenfrequencies $\omega_{\mathrm{TO}j}$ obtained from fitting is presented in Fig. 3.2. The TO1 mode strongly softens with decreasing temperature. In the measured temperature range the soft-mode frequency obeys the Cochran law (1.6). The roughly extrapolated critical temperature is -4 ± 2 K which is slightly lower than 13.1 K obtained in single crystals by a fit of the permittivity with the Barrett expression [2]. The temperature dependence of the soft-mode frequency ω_{TO1} is in a good agreement with that obtained for single crystals by hyper-Raman scattering [187]. The damping constant γ_{TO1} of the soft mode is shown in the inset of Fig. 3.2. It is almost linearly decreasing from a room temperature value of 15.1 cm^{-1} to 4.6 cm^{-1} at 20 K, and it qualitatively corresponds to the hyper-Raman data.

Ichikawa et al. [177] reported slightly lower values of ω_{TO1} and γ_{TO1} obtained for single crystals above 100 K than those of our results and of the hyper-Raman scattering data.

The temperature dependence of the dielectric constant measured in the MW range together with the loss tangent (red symbols) is shown in Fig. 3.3. The loss tangent reaches the values 9.5×10^{-3} and 5.2×10^{-3} at 300 and 20 K, respectively, which are higher then those in single crystals reported for 3 GHz: 1.4×10^{-4} and 4.2×10^{-5} at 300 and 5.4 K, respectively [174]. There are two loss peaks observed at ~145 and 32 K. The first one corresponds to the relaxation observed in KTO ceramics [179] and single crystals [175]

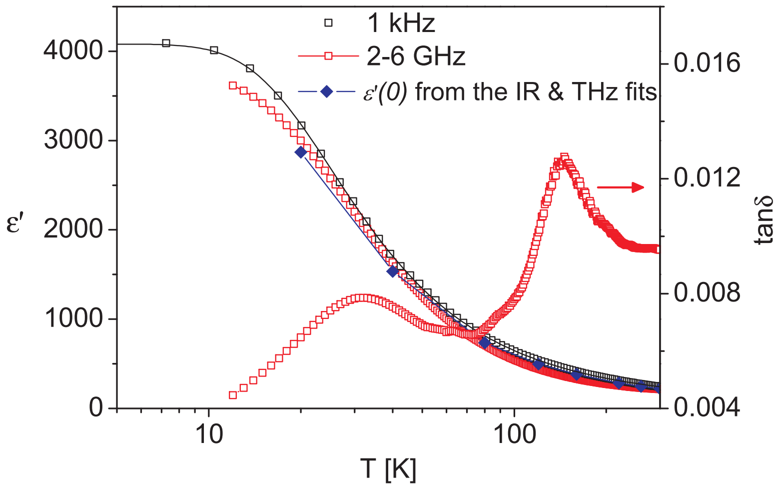

Figure 3.3: Temperature dependences of the RF (1 kHz) and MW (2-6 GHz) dielectric permittivity ε' compared to the phonon contribution calculated from the IR and THz data. The MW loss tangent is also shown. The RF measurement is taken from Ref. [179], the black solid line is a fit by the Barrett expression (3.1). Other lines are guides to the eye.

near 45 K at 1 kHz. Probably, it is related to lattice defects and/or impurities, however, its origin remains unclear. The second peak (32 K) appears in the same temperature range as that reported previously for single crystals; it is ascribed to the interaction between the transverse optic and longitudinal acoustic modes partially driven by defects [188, 189].

The phonon contribution to the permittivity obtained from the IR and THz fits (blue symbols) and the RF measurements at 1 kHz (black symbols), taken from Ref [179], are also shown in Fig. 3.3. The temperature dependence of the dielectric constant measured in RF range has been fitted by the Barrett expression (3.1). The obtained values of the fit parameters are as following: $C = 5.1 \times 10^4$ K, $T_1 = 56$ K, $T_0 = 15$ K, and $\varepsilon_b = 64$. These values are in a good agreement with those previously found for single crystals [2, 190], only a slightly lower value of C is found for our ceramics.

The data obtained from the IR and THz fits correspond well to those obtained in the MW and radio frequency ranges (see Fig. 3.3). The small differences at low temperatures are within the accuracy of the MW experiment and of the IR fit. Minor differences in the microstructures of individual samples can also contribute to this discrepancy.

3.1.3 Summary

The observed temperature dependence of the broadband permittivity and the soft-mode frequency in the KTO ceramics are typical for incipient ferroelectrics. Their values are comparable to those of single crystals. Moreover, the low-frequency permittivity in the ceramics is mainly of intrinsic origin, i.e., stemming from the polar phonons. All these results indicate rather small influence of grain boundaries on the macroscopic dielectric response. However, higher MW losses (compared to single crystals), their temperature dependence and the presence of first-order peaks in Raman spectra [184] indicate an existence of defects in the KTO ceramics.

To estimate the possible dielectric grain size effect on KTO ceramics further investigations of smaller grain size ceramics using broadband dielectric spectroscopy including RF, MW, THz and IR techniques are needed.

3.2 Tunable dielectric properties of $SrTiO_3$

3.2.1 $SrTiO_3$ single crystals

Strontium titanate ($SrTiO_3$, STO) is an incipient ferroelectric with a low-temperature behavior very similar to that of KTO. However, STO shows a ferroelastic (non-ferroelectric) structural phase transition involving oxygen octahedra tilting. This phase transition occurs at about 105 K at atmospheric pressure and involves the condensation of a zone-boundary mode [191]. It is an example of the simplest anti-distortive structural transition called a cell-doubling transition.

The high-temperature dielectric response obeys the Curie-Weiss law (1.1) suggesting a ferroelectric phase transition at about 35−40 K. However, at low temperatures, Barret-like deviations (3.1) from the Curie-Weiss law (linearity) occur, and the dielectric constant continuously increases down to helium temperatures at atmospheric pressure. Finally, the permittivity attains value of 3×10^4 [192]. The fit of the dielectric constant to Barrett's expression (3.1) is less good than for $KTaO_3$. Possibly, this reflects a greater importance of the lattice-mode dispersion in the somewhat less stable titanate [1]. Deviations from the Curie-Weiss behavior of the dielectric constant temperature dependence are observed below ∼100 K for STO while for KTO they occur below ∼60 K [2].

A single-domain dielectric response of STO is more complicated than that of KTO and it shows an anisotropy and hysteresis due to the tetragonal symmetry of the ferroelastic phase [1]. STO crystals can be prepared in a single-domain form by means of cooling under an applied stress. The single-domain form is retained when the stress is removed until the temperature is raised again above the phase transition point. Careful single-crystal measurements of the dielectric constant have been performed by Sakudo and Unoki [183]. They observed a distinct tetragonal anisotropy of the response below about 110 K.

The electric-field tuning of the dielectric properties of STO single crystals and unstrained films was previously extensively studied in a view of their applications in microwave tunable devices. Nevertheless, these investigations have been mostly limited to low temperatures (20−90 K) and to low frequencies (GHz range and below) [193–195]. It was commonly accepted that the dielectric behavior of STO single crystals are not tunable above ∼100 K.

Preliminary results about the soft-mode behavior in a bulk STO biased by the electric field obtained using the THz spectroscopy [24] induced further detailed investigation of bulk STO. In this work we used TDTS to characterize the electric-field-tuning capabilities of STO single crystals within a broad temperature interval (90−300 K).

3.2.2 Theoretical background

Our theoretical background is based on the Landau-Devonshire theory, which provides a direct evaluation of the dielectric response of ferroelectrics. STO is characterized by a strong transverse soft phonon mode which accounts for more than 95 % of its dc permittivity value. The Helmholtz free-energy density F is here expanded in a power series with respect to the components P_j of the macroscopic polarization vector. We introduce here explicitly the components of the polarization vector P_x, P_y, P_z in order to describe the possible anisotropy of the soft-mode potential. These polarization components are associated with the soft-mode eigenvector characterized by a relative displacement of the oxygen octahedron with respect to the central Ti ion. However, in the paraelectric state the spontaneous part of the polarization vanishes. One is left then with a bias-field-induced dc or low-frequency term ΔP_j and with a small dynamic term $P_{j,dyn}$ driven by a weak probing (THz) field: $P_j = \Delta P_j + P_{j,dyn}$. The weakness of the THz field ensures that nonlinear effects may arise only from the bias field ($\Delta P_j \gg P_{j,dyn}$). The allowed terms in the Helmholtz free-energy density up to the fourth order of the power series in the cubic paraelectric phase of STO read [23, 191]:

$$F(T) = \frac{1}{2}\alpha \left(P_x^2 + P_y^2 + P_z^2\right) + \frac{1}{4}\beta_{\parallel} \left(P_x^4 + P_y^4 + P_z^4\right) + \frac{1}{2}\beta_{\perp} \left(P_x^2 P_y^2 + P_y^2 P_z^2 + P_z^2 P_x^2\right), \quad (3.2)$$

where $\beta_{\parallel}$ and $\beta_{\perp}$ characterize the anharmonicity and anisotropy of the soft-mode potential. They describe the tetragonal symmetry of the structure induced by the applied bias. Note that for $\beta_{\parallel} = \beta_{\perp} \equiv \beta$ one obtains

$$F(T) = \frac{1}{2}\alpha \left(P_x^2 + P_y^2 + P_z^2\right) + \frac{1}{4}\beta \left(P_x^2 + P_y^2 + P_z^2\right)^2 \quad (3.3)$$

which is equivalent to the expression (1.2) up to the fourth order. The coefficient describing the harmonic part of the potential can be written as [196]

$$\alpha = \frac{\omega_0^2}{f_{osc}\varepsilon_{vac}}, \quad (3.4)$$

where ω_0 is the soft-mode bare frequency, f_{osc} is its oscillator strength, and ε_{vac} is the vacuum permittivity. The relation between an external electric field with components E_j and the induced polarization is given by a dielectric equation of state

$$E_j = \frac{\partial F}{\partial P_j}, \quad (3.5)$$

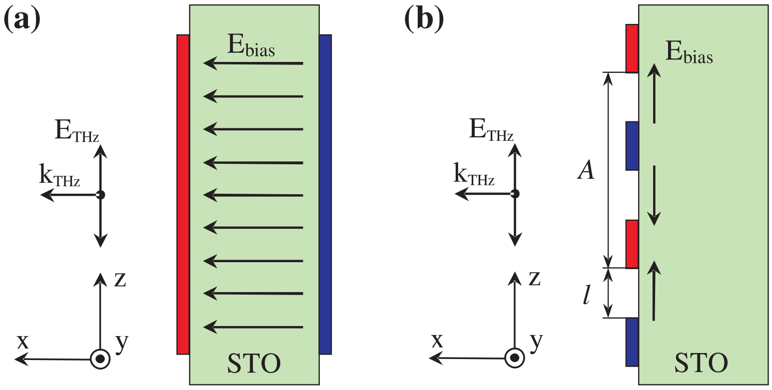

Figure 3.4: Schematic illustration of the two experimental geometries used: **(a)** Perpendicular geometry; nanocrystalline tin oxide electrodes; and **(b)** parallel geometry; the bias is applied by using interdigitated metallic electrodes. $A = 40$ µm: period of the electrode structure; $l = 15$ µm: distance between the electrode fingers.

e.g., for the z component

$$E_z = \alpha P_z + \beta_{\|} P_z^3 + \beta_{\perp} P_z \left(P_x^2 + P_y^2\right). \tag{3.6}$$

For the other two components of the field analogous equations are found.

Within the linear approximation the polarization P_j related to the soft mode is equal to $\varepsilon_{vac}\delta\varepsilon E_j$, where $\delta\varepsilon$ is the harmonic contribution of the soft mode to the permittivity:

$$\delta\varepsilon = \frac{1}{\alpha\varepsilon_{vac}} = \frac{f_{osc}}{\omega_0^2}. \tag{3.7}$$

The oscillator strength f_{osc} is usually temperature independent, and the permittivity value in the sub-THz range then crucially depends on the soft-mode frequency. However, the electric-field tunability is related to the anharmonicity of the Helmholtz potential, as will be shown later.

In the coordinate system we use (shown in Fig. 3.4), the probing THz electric field is parallel to the z direction, therefore, we are going to evaluate the component ε_{zz} of the dielectric permittivity as a function of a perpendicular E_x (Fig. 3.4a) and of a parallel E_z (Fig. 3.4b) bias electric field. In these configurations P_y vanishes and one finds

$$\varepsilon_{zz} = \frac{1}{\varepsilon_{vac}}\frac{\partial P_z}{\partial E_z} + \varepsilon_\infty \approx \left[\frac{1}{\delta\varepsilon} + 3\beta_{\|}\varepsilon_{vac}\left(\Delta P_z\right)^2 + \beta_{\perp}\varepsilon_{vac}\left(\Delta P_x\right)^2\right]^{-1} + \varepsilon_\infty; \tag{3.8}$$

where ε_∞ is a cumulative contribution to the permittivity caused by higher-frequency excitations such as hard phonons and electrons. The polarization ΔP_j vanishes in the absence of the bias field, and $\varepsilon_{zz}(T) = \delta\varepsilon(T) + \varepsilon_\infty \equiv \varepsilon_0(T)$; in this case the temperature dependence of the permittivity is essentially given by the temperature dependence of the soft-mode frequency. An applied external bias induces polarizations ΔP_x and ΔP_z. In order to evaluate them we use the lowest-order terms of the power expansion of (3.6):

$$P_z \approx \frac{1}{\alpha}E_z - \frac{\beta_\parallel}{\alpha^4}E_z^3 - \frac{\beta_\perp}{\alpha^4}E_z E_x^2, \tag{3.9}$$

$$P_x \approx \frac{1}{\alpha}E_x - \frac{\beta_\parallel}{\alpha^4}E_x^3 - \frac{\beta_\perp}{\alpha^4}E_x E_z^2. \tag{3.10}$$

We now discuss the two geometries depicted in Fig. 3.4. (*i*) In the perpendicular geometry (Fig. 3.4a) $E_x = E_{bias}$ and $E_z = E_{THz}$. The linear response to the THz field then reads

$$P_{z,dyn} \approx \left(\frac{1}{\alpha} - \frac{\beta_\perp}{\alpha^4}E_{bias}^2\right)E_{THz} \tag{3.11}$$

and

$$\varepsilon_{zz}\left(E_{bias} \parallel x\right) = \left[\frac{1}{\delta\varepsilon} + \frac{\beta_\perp f_{osc}^2 \varepsilon_{vac}^3 E_{bias}^2}{\omega_0^4} + \cdots\right]^{-1} + \varepsilon_\infty. \tag{3.12}$$

Thereby, application of an external bias $E_{bias} \parallel x$ leads to a change of the soft-mode potential due to its anharmonic character and we observe a field-induced hardening of the soft mode, which can be analytically expressed by using equations (3.7) and (3.8) or (3.12):

$$\omega_0^2\left(E_{bias} \parallel x\right) = \omega_0^2\left[1 + \frac{\beta_\perp \varepsilon_{vac} f_{osc}}{\omega_0^2}\left(\Delta P_x\right)^2\right] \approx \omega_0^2\left[1 + \beta_\perp\left(\frac{\varepsilon_{vac} f_{osc}}{\omega_0^2}\right)^3 E_{bias}^2\right]. \tag{3.13}$$

(*ii*) In the parallel geometry, as a first approximation (Fig. 3.4b), we assume that $E_x = 0$ and $E_z = E_{bias} + E_{THz}$ and

$$P_{z,dyn} \approx \left(\frac{1}{\alpha} - 3\frac{\beta_\parallel}{\alpha^4}E_{bias}^2\right)E_{THz}. \tag{3.14}$$

The expression for the permitiivity then reads

$$\varepsilon_{zz}\left(E_{bias} \parallel z\right) = \left[\frac{1}{\delta\varepsilon} + \frac{3\beta_\parallel f_{osc}^2 \varepsilon_{vac}^3 E_{bias}^2}{\omega_0^4} + \cdots\right]^{-1} + \varepsilon_\infty \tag{3.15}$$

and the soft-mode hardening is analytically expressed:

$$\omega_0^2\left(E_{bias} \parallel z\right) = \omega_0^2\left[1 + \frac{3\beta_\parallel \varepsilon_{vac} f_{osc}}{\omega_0^2}\left(\Delta P_x\right)^2\right] \approx \omega_0^2\left[1 + 3\beta_\parallel\left(\frac{\varepsilon_{vac} f_{osc}}{\omega_0^2}\right)^3 E_{bias}^2\right]. \tag{3.16}$$

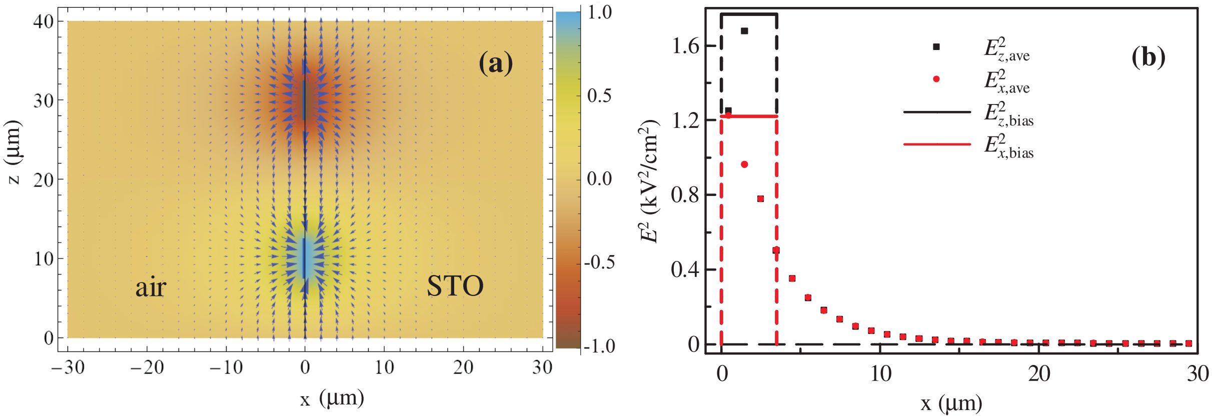

Figure 3.5: Electrostatic simulation of the electric-field distribution near the air-STO interface ($x = 0$). **(a)** Arrows: electric-field distribution; colors: electrostatic potential distribution. **(b)** Squared value of the bias field components $E_{z,avg}$ and $E_{x,avg}$ averaged over 1-μm-thick slices in the x direction parallel to the surface. The simulation is done for an electrostatic potential of ±1 V on the electrodes.

However in reality, the bias field in the parallel geometry is highly inhomogeneous and it rapidly decays along x inside STO. Consequently, only a thin layer of STO is influenced by the applied field. In order to evaluate the transmission data we need to determine an effective thickness d_E of this layer and an effective value of the applied electric field E_{bias}. The latter would then be assumed homogeneous within the layer with thickness d_E. We performed electrostatic simulations [197] to determine the distribution of the bias field close to the interdigitated electrode structure for this geometry (Fig. 3.5a). Both the z and x components of the field are nonzero and highly inhomogeneous along x and z [$E_z(x,z)$ and $E_x(x,z)$]. The variation along x of their averaged squared values $(E_{x,avg})^2$ and $(E_{z,avg})^2$ is shown in Fig. 3.5b. Here each plotted value is averaged over a 1-μm-thick layer parallel to the interface, i.e., the first plotted values are each obtained as an average value of the appropriate component over one period of the electrode structure along z and between 0 and 1 μm depth along x.

A natural choice for the z component of the effective field would be $E_{z,bias} = U_{bias}/l$, where U_{bias} is the applied bias voltage and $l = 15$ μm is the distance between the electrode fingers. For this component we found

$$\int_0^\infty (E_{z,avg})^2 \mathrm{d}x = (E_{z,bias})^2 d_E \approx (E_{z,max})^2 d_E, \tag{3.17}$$

and similarly for the x component we obtain

$$\int_0^\infty (E_{x,avg})^2 \mathrm{d}x \approx (E_{x,max})^2 d_E, \tag{3.18}$$

where $(E_{j,max})^2$ $[j = x, z]$ is the maximum averaged squared-field value (see Fig. 3.5b) and the penetration depth $d_E \approx 3.5$ μm is the same for both components. Therefore, we define $E_{x,bias} = E_{x,max}$ for the purposes of evaluating of our experimental data.

Obviously, the soft-mode frequency in the parallel geometry depends on both the x and z components of the bias field, and combining (3.13) and (3.16) we obtain

$$\omega_0^2 \left(E_{x,bias}, E_{z,bias}\right) \approx \omega_0^2 \left[1 + 3\beta_{\|} \left(\frac{\varepsilon_{vac} f_{osc}}{\omega_0^2}\right)^3 E_{z,bias}^2 + \beta_{\perp} \left(\frac{\varepsilon_{vac} f_{osc}}{\omega_0^2}\right)^3 E_{x,bias}^2\right]. \tag{3.19}$$

We can conclude that in the parallel geometry both the z and x components of the bias field influence the soft-mode potential. Nevertheless, the z component of the field is dominant and the x component induces only a small correction of the soft-mode frequency. There is no a multiplication factor of 3 in the $\beta_{\perp}$ term in (3.19), and in addition, as can be seen in Fig. 3.5b, the value of x component of the bias field is smaller than that of the z component.

It should be mentioned that measurements in the two experimental geometries allow us to evaluate the two different anharmonic coefficients of the soft-mode potential $\beta_{\|}$ and $\beta_{\perp}$. Fleury and Worlock [191] found similar values of the order of 10^{10} JC^{-4}m^5 for both coefficients at low temperatures.

The dynamical response in the THz range of the samples measured in both geometries can be simply described by a harmonic oscillator formula, where the soft-mode frequency is tunable by the external bias:

$$\varepsilon_{zz} \left(\omega; T, E_{bias}\right) = \frac{f_{osc}}{\omega_0^2 \left(T, E_{bias}\right) - \omega^2 - i\omega\Gamma(T)} + \varepsilon_{\infty}. \tag{3.20}$$

The soft-mode damping Γ is slightly temperature dependent [198] and, in principle, it can be also weakly electric-field dependent.

3.2.3 Experimental details

Several series of experiments were done and numerous spectra were acquired and analyzed to characterize the tunability of bulk single crystal STO. All the experimental spectra were measured using our custom-made time-domain THz spectrometer described in the previous chapter.

The investigated STO crystals were purchased from Crystal GmbH and thinned down by mechanical polishing to the thickness of 50 or 100 μm. The dimensions of the studied samples were 10 × 10 × 0.1 and 10 × 10 × 0.05 mm^3. Relatively large single crystals possess residual stress due to the mechanical treatment during sample preparation. Plastic deformation occurs at and near the surface of a crystal, and an elastic deformation spans over significant distances below the surface. One of the possible ways to remove the residual stress is etching of the surface layer as described in reference [193]. However, previous experience of our group with the etching of the bulk STO in H_3PO_4 [78] showed that the surface becomes rather rough and does not meet the criterion of optical quality. Such a surface roughness is a serious obstacle for the preparation of a fine interdigitated electrode structure (discussed below). Therefore, chemical etching, which is known to produce no residual stress, could not be used because it leads to a corrugated surface [78].

We suppose that both sides polished STO crystals we used show some residual stress which is to a large extent homogeneous over the central part near the surface of the slab. To confirm this we investigated one of the 50-μm-thick single crystals using an optical microscope equipped with crossed polarizers. The sample was completely dark with the exception of less than 1 mm wide areas along the edges. Our experience is that thin STO samples (∼50 μm) sometimes tend to bend due to the residual stress; in the experiments we used samples which do not bend. The central part of the sample probably has a slightly distorted lattice parameter compared to a stress-free material, but we believe that it does not significantly affect the dielectric behavior of STO.

To realize experimentally both parallel and perpendicular geometries (Fig. 3.4), we deposited two different electrode structures on the samples. In the first series of samples an interdigitated electrode structure was deposited on a single side (Fig. 3.4b). This structure was prepared in Jülich (by G. Panaitov) by magnetron sputtering deposition of an intermediate 20-nm Nb adhesion layer and of a 300-nm-thick Au layer; subsequently, the electrodes were formed using a standard lift-off photolithography. The resulting electrodes consisted of 5-μm-wide metal stripes separated by 15-μm-wide gaps. The total area covered by the electrode structure was $\sim 6\times 6$ mm^2. These electrodes allow application of an in-plane bias field, i.e., enable experiments in the parallel geometry. They are transparent for the THz radiation when the electric-field vector is perpendicular to the metallic stripes.

Measurements in the perpendicular geometry require deposition of electrodes on both sides of the plates (Fig. 3.4a). We used nanocrystalline antimony-doped tin oxide films which combine a sufficient electric conductivity and transparency in the THz range. The synthesis of Sb-doped tin oxide nanoparticles is described in details in reference [199]. We deposited these electrodes on STO samples at the Ludwig Maximilian University of Munich in collaboration with Dina Fattakhova-Rohlfing. For these deposition, the dried nanoparticles (0.2 mg) were dispersed in tetrahydrofuran (4 mL) containing one drop of concentrated HCl. The obtained transparent colloidal solutions were deposited on the substrates by spin coating and calcined afterward at 500 °C. The area covered with the electrodes was $\sim 8\times 8$ mm^2 in this case. Finally, an additional sample was prepared with an interdigitated electrode structure on one side and a nanocrystalline tin oxide thin film deposited on the other side. This served to check the consistency of the experimental results obtained in both geometries using the same STO crystal.

The investigated samples were placed into an optical cryostat equipped with electrical connections for applying the bias field. The experiments were carried out using the transmission arrangement of the THz spectrometer. The area on the sample probed by THz beam was defined by a metallic aperture of 5−8 mm in diameter. Usually, the sample is

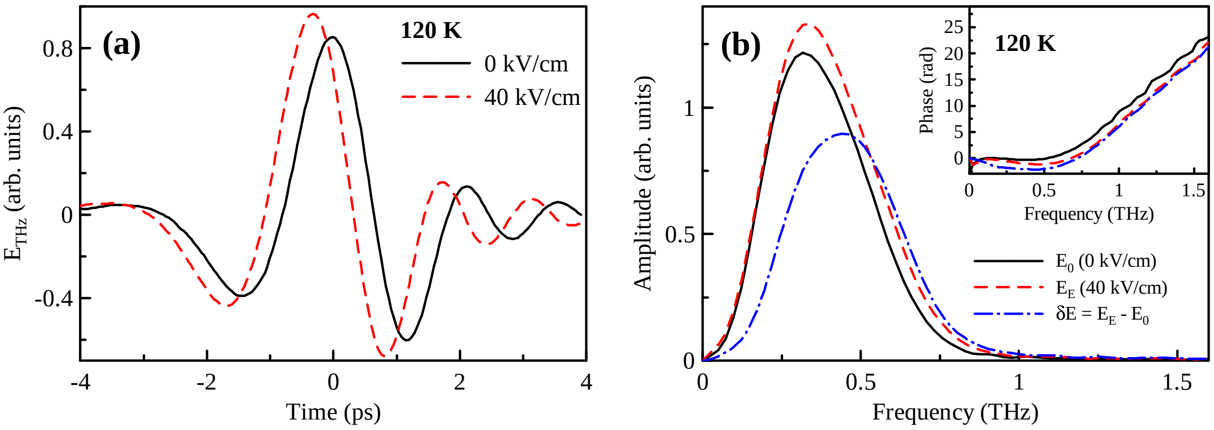

Figure 3.6: Experimental time-domain wave forms **(a)** and spectra **(b)** obtained with a 100-μm-thick STO crystal in the perpendicular geometry at 120 K. Here the field-induced tuning is represented by the signal displacement to shorter time delays with applied voltage which corresponds to a field-induced reduction of the permittivity.

attached to the aperture, but, in the perpendicular geometry, it was not possible due to the presence of the electrodes on both sides of the plates. An additional dielectric spacer had to be inserted between the metallic aperture and the sample in order to achieve good electrical insulation of the sample from the cryostat. Unfortunately, such configuration produced artifacts in the measured signal. These were caused by a partial reflection of the THz pulse on the front sample surface which was subsequently diffracted on the edges of the aperture. Extreme experimental care was taken to avoid this parasitic signal tunable by the applied electric bias and coming to the detector as a slightly delayed weak pulse echo stretched in time.

A high-voltage source with the possibility of monitoring the flowing current was used in order to keep the samples far from the dielectric breakdown. For each sample a series of wave forms $E(t)$ (Fig. 3.6a) was measured in a repeated sequence. Each sequence was started by a reference measurement (zero-bias field) and continued by increasing stepwise the bias voltage during the returns of the optical delay line. After a scan with the maximum bias voltage the sequence was restarted and the whole procedure was repeated many times in order to improve the signal-to-noise ratio. This procedure minimized the influence of possible long-term drifts of the laser beam. The data acquisition at each temperature and for approximately six to eight values of the bias field lasted $\sim$3-4 h.

The THz dielectric spectra of unbiased STO (we denote the permittivity ε_0 and the refractive index N_0) were determined previously [24]. The spectra of the biased samples N_E

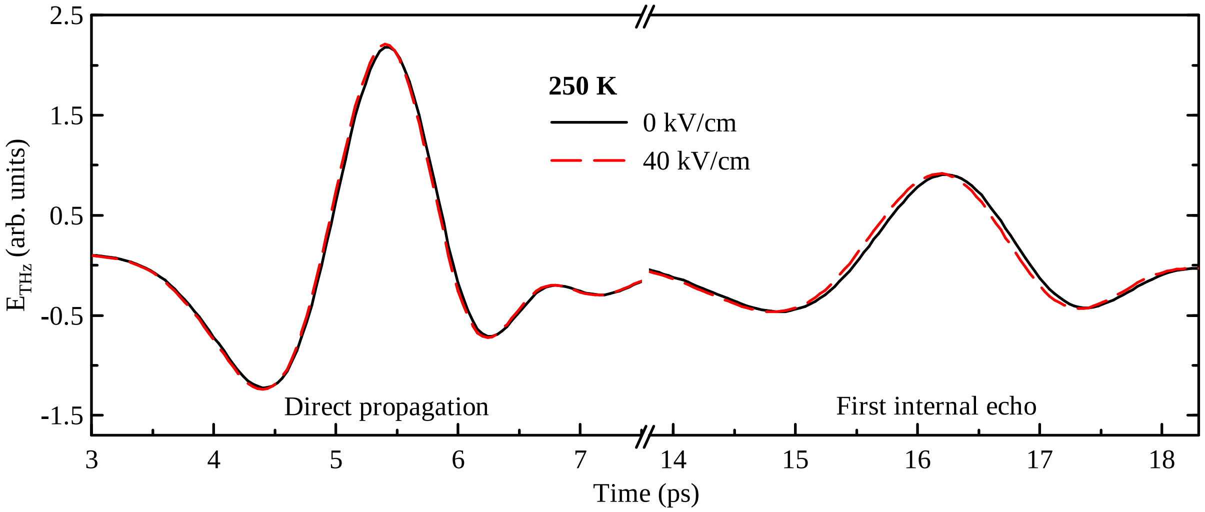

Figure 3.7: Time-domain wave form measured at 250 K: direct propagation and the first internal echo. Here the field-induced tuning is more pronounced for the echo; this is caused by tree times longer propagating distance within the biased material for the echo than that for the directly passed signal.

were determined numerically as a root of a complex equation for each spectral component:

$$\frac{T(\omega; N_E)}{T(\omega; N_0)} = \frac{T_E(\omega)}{T_0(\omega)}. \tag{3.21}$$

The spectra T_E and T_0 on the right-hand side are the measured complex transmission functions with and without bias, respectively. The left-hand side contains the theoretical expressions for the transmittance (2.9).

For the experiments done in the perpendicular geometry the field distribution inside the sample is homogeneous, and, consequently, the complex refractive index under bias N_E is also homogeneous. The sample is optically thick in the THz range due to its high THz permittivity value, and we may take an advantage of the time-domain windowing procedure [166]. Due to Fabry-Pérot reflections inside the sample, the signal wave form consists of a series of echoes well separated in time. Therefore, we truncate the experimental signal in such a way that the studied part of the wave form corresponds to the j^{th} echo which leaves the sample after $2j$ internal reflections. This means that we are left only with the j^{th} term of the sum of the analytical expression for the transmittance (2.9).

At low temperatures the dielectric spectra were obtained from a direct pass ($j = 0$). When the temperature is increased, the sample becomes more transparent and less tunable at the same time. In this case it is advantageous to perform the calculation for a higher-order echo ($j = 1$ or 2) for which the corresponding transmitted signal is still sufficiently high but more affected by the electric-field-modified refractive index. For instance, the first echo undergoes three passes through the sample while the directly transmitted beam undergoes a single one. This procedure increases the sensitivity of the experiment as shown in Fig. 3.7.

We used the approximation illustrated in Fig. 3.5b for the evaluation procedure of the data obtained in the parallel geometry. We consider a fraction of the sample under bias as a thin film with a homogeneous refractive index N_E and thickness d_E while the remaining bulk part was treated as a substrate with the refractive index N_0.

Assuming identical values for the parallel ($\beta_{||}$) and perpendicular ($\beta_{\perp}$) anharmonic coefficients, a comparison of equations (3.13) and (3.19) shows that the soft-mode frequency (and, consequently, the permittivity) should depend more steeply on the bias field in the parallel geometry. For identical voltages applied, the bias electric field close to the electrodes is substantially higher in the parallel geometry. This leads to much higher filed-induced effects near the electrodes. However, the perpendicular geometry allows one to induce a homogeneous change of the permittivity in the whole volume of the sample while in the parallel geometry only a 3.5-µm-thick layer is affected by the bias field. The THz pulse then acquires useful information only when it propagates through this thin layer and it just suffers an unwanted absorption in the rest of the sample. Taking this facts into account, we conclude that the perpendicular arrangement provides a larger sensitivity and a better accuracy of the measurements of the field-induced effects than the parallel one.

3.2.4 Results and discussion

Examples of raw experimental spectra are shown in Figs. 3.6 and Fig. 3.7. At 120 K the soft-mode frequency is as low as 1.5 THz, and, as a result, the sample is relatively opaque while its tunability is high (see Fig. 3.6). The soft-mode frequency rises above 2.4 THz close to the room temperature and the sample becomes much more transparent. However, the tunability is significantly reduced compared with low temperatures (see Fig. 3.7). It should be mentioned that at higher temperatures (250 and 300 K) the field-induced tuning was determined from the transmittance calculated using the first echo of the THz wave forms. The small field-induced contribution is visible in Fig. 3.7 as an advance of the first echo obtained under bias compared to that obtained without bias. It means that the THz pulse propagating through the biased sample experiences an optically shorter path than if it propagates through the unbiased sample, i.e, $N_E < N_0$. This approach allowed us to quantify the tunability of STO up to the room temperature.

The calculated permittivity spectra at 120 K under the bias for both geometries are shown in Fig. 3.8. When the bias is increased the real part of the permittivity is decreasing in the whole experimentally accessible frequency range for both geometries. Actually, this is a signature of the soft-mode hardening, as shown in the theoretical section. The shape of the spectra obtained in the perpendicular geometry remains unchanged within the experimental uncertainty. This means that the damping of the soft mode does not change significantly under the bias field. The data obtained in the parallel geometry show a

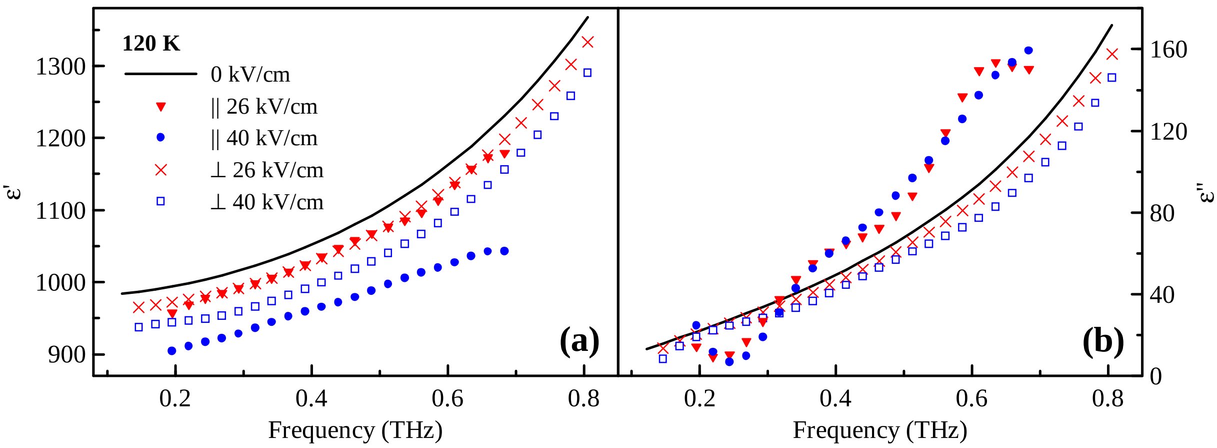

Figure 3.8: Dielectric permittivity of a 100-µm-thick STO crystal at 120 K: real part **(a)** and imaginary part **(b)**. Unbiased permittivity (solid line) is approximated using an underdamped harmonic oscillator model [24]. The permittivity under electric field was calculated from the experimental wave forms. Full symbols represent results of the tuning in the parallel geometry; crosses and empty symbols represent results obtained in the perpendicular geometry.

slightly higher tunability of the real permittivity than that obtained in the perpendicular geometry. A completely different behavior is observed for the losses: they slightly decrease in the perpendicular geometry, while they increase under bias in the parallel geometry. We think that such an increase of the losses might be related to a broadening of the soft mode induced by the inhomogeneous distribution of the applied field in the parallel geometry.

It is known that STO crystals experience a ferroelastic cubic-to-tetragonal phase transition at 105 K. In the low temperature ferroelastic phase the ferroelectric soft mode, which is a highly degenerated T_{1u} zone-center mode, splits into a doubly degenerated E_u mode and a higher-frequency A_{2u} mode, as reported, e.g., in a hyper-Raman study by Yamanaka et el [198]. Therefore, the linear dielectric properties of STO become anisotropic. However, the soft-mode splitting is continuous, and the anisotropy is quite small at temperatures close to the phase transition. For example, at 90 K the frequency splitting is of $\sim$0.9 cm^{-1}, i.e., of $\sim$2 % of the mean frequency value. This splitting leads to an anisotropy of the permittivity only of $\sim$4 % [183].

The soft-mode splitting below 105 K cannot be directly observed in the THz transmission spectra, since the thinnest samples investigated are completely opaque above $\sim$1 THz. In fact, the studied samples below the ferroelastic phase transition consist of a distribution of optically anisotropic parts forming a polydomain composite. Nevertheless, down to $\sim$90 K this local optical anisotropy remains weak and the experimental data represent an average dielectric response of such a composite. The measured field-induced soft-mode

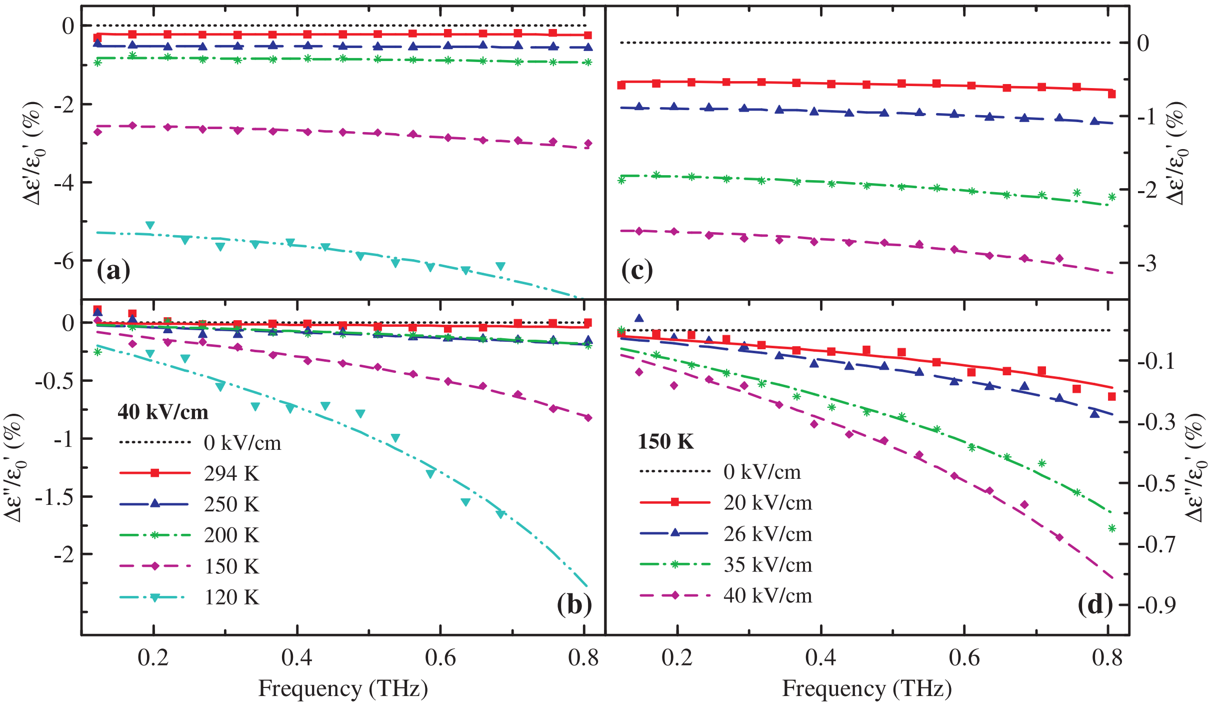

Figure 3.9: Relative field-induced changes in the complex dielectric function obtained for the perpendicular geometry. **(a)** and **(b)** E_{bias} = 40 kV/cm, varying T; **(c)** and **(d)** T =150 K, varying the bias field. Symbols: Experimental data. Lines: Fits by an underdamped harmonic oscillator.

hardening can then be understood as an average hardening of the two split soft-mode components. Indeed, we did not observe any measurable hysteresis of the electric-field-induced properties at 90 K, and this is in agreement with the low-temperature and low-frequency data reported by Hemberger et al [200]. In this way, our description of the tetragonal sample as an approximately cubic medium is justified.

Perpendicular geometry

Selected experimental spectra of the field-induced tunability obtained in the perpendicular geometry are shown in Fig. 3.9. The tunability is characterized by relative changes of the real and imaginary dielectric functions $\Delta\varepsilon'/\varepsilon'_0$ and $\Delta\varepsilon''/\varepsilon'_0$, where $\Delta\varepsilon'$ and $\Delta\varepsilon''$ are the variations upon the applied field of the real and imaginary parts of the permittivity, and ε'_0 is the real permittivity without an external bias.

Relative field-induced changes of the dielectric function for several temperatures under the same electric bias field of 40 kV/cm are shown in Figs. 3.9a,b. The field-induced tunability of the permittivity is increasing upon cooling and toward higher frequencies

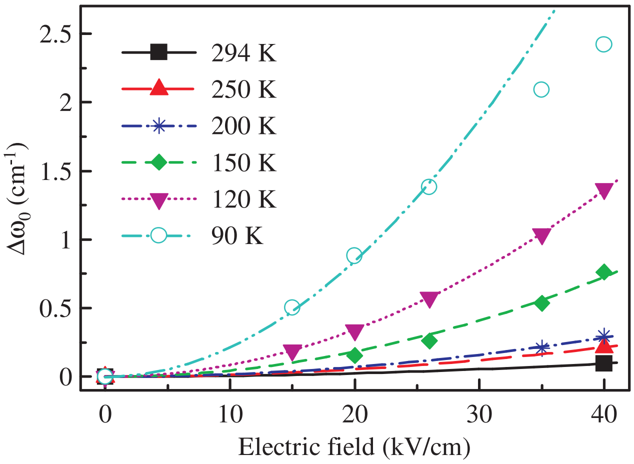

Figure 3.10: Electric-field-induced hardening of the soft-mode frequency in the perpendicular geometry at several temperatures. The symbols represent the fits of the experimental spectra using a harmonic oscillator model (3.20); the lines represent fits of the soft-mode behavior at each temperature by (3.22)

at all temperatures. The lines in Fig. 3.9 are fits of the experimental data by an underdamped harmonic oscillator model given by (3.20). The oscillator strength f_{osc} and the high-frequency permittivity ε_∞ are found to be unchanged with temperature and electric field. Therefore, the previously found values [24] were used and kept fixed for all fits. In addition, the values of the temperature-dependent soft-mode frequency and damping of unbiased STO were taken from the literature [24]. The only varying parameters during the fitting were thus the soft-mode frequency and damping in biased STO. The fit reveals that the soft-mode frequency constitutes the crucial parameter describing nearly entirely the field-induced changes observed in the spectra. The soft-mode damping does not vary substantially with the field and its variation has only a minor impact on the fit quality. At 120 K, a decrease of the real part of the permittivity induced by a field of 40 kV/cm is ~6 %. The change of its imaginary part is smaller but its frequency dependence becomes steeper with decreasing temperature. This behavior is consistent with an increased tunability of STO at lower temperatures. The soft mode softens with decreasing temperature, leading to larger anharmonic effects upon applied bias. Analogous results obtained at 150 K for several bias fields are shown in Figs. 3.9c,d. The behavior of the real and imaginary parts of the field-induced changes is in agreement with the picture of soft-mode hardening with increasing temperature and the electric field.

The complete picture of the soft-mode frequency tuning in the perpendicular geometry is shown in Fig. 3.10. The data is expressed as the difference between the soft-mode frequency with the field on and off: $\Delta\omega_0(E_{bias}) = \omega_0(E_{bias}) - \omega_0$. The values $\omega_0(E_{bias})$ were obtained by fitting the entire set of complex permittivity spectra with the harmonic oscillator model (3.20). The lines in Fig. 3.10 were fitted for each temperature by an expression derived from formula (3.13), which is valid for a reasonably weak field:

$$\Delta\omega_0\left(E_{bias}\right) \approx \omega_0\left[\sqrt{1+\beta_\perp\left(\varepsilon_{vac}f_{osc}/\omega_0^2\right)^3 E_{bias}^2}-1\right], \tag{3.22}$$

where $\beta_\perp$ is the only fitting parameter. The largest field-induced change in the soft-mode frequency under a maximum bias field (40 kV/cm) is of 2.4 cm^{-1} at 90 K. The tuning represents ∼6 % of the frequency of the soft mode. The field-induced changes in the permittivity exceeds 15 % in this case. One can observe a saturation of the soft-mode hardening in Fig. 3.10 for the data obtained at 90 K. This can be explained by higher-order terms in E_{bias}, which were neglected in expression (3.22). Therefore, the two data points obtained under highest-bias fields at 90 K were not taken into account in this fitting.

Parallel geometry

Experimental spectra of the field-induced tunability obtained in the parallel geometry are illustrated in Fig. 3.11. As already discussed, the experimental sensitivity in this case is lower than in the perpendicular geometry. It is especially pronounced on the data representing the imaginary part of the permittivity (Figs. 3.11b,d), where the noise is considerably larger causing less satisfactory fits. Nevertheless, the change of the real part of the dielectric function at 40 kV/cm and 120 K is larger (∼10 %) than the value found in the perpendicular geometry.

The highly inhomogeneous distribution of the applied field (shown in Fig. 3.5a) results in an inhomogeneous broadening of the soft-mode spectral line. Consequently, the best fits are achieved for a slightly increased value of the damping parameter Γ of the soft mode compared to its zero-bias value. For example, at 120 K the damping value at high fields increases by up to 65 % compared to zero field value $\Gamma(E_{bias}=0) = 8$ cm^{-1} [24]. However, close to room temperature this increase of the damping is not observed. This effect can be traced in Figs. 3.11b,d as well. Here, for higher temperatures ($T \geq 200$ K), the field-induced change of the imaginary part of the permittivity has a negative value $\Delta\varepsilon''(\omega) < 0$ similarly as it was found in the perpendicular geometry; and this reflects the picture of the soft-mode hardening under the bias. In contrast, for low temperatures, the field-induced change of the imaginary part acquires positive values $\Delta\varepsilon''(\omega) > 0$ due to a significant increase of the soft-mode damping caused by the inhomogeneous distribution of the applied field.

The complete picture of the soft-mode frequency tuning by the electric field in the parallel geometry is presented in Fig. 3.12. The largest field-induced change of the soft-mode frequency under a maximum bias field of 67 kV/cm and at $T = 90$ K is 10.5 cm^{-1} which corresponds to ∼27 % of the soft-mode frequency without bias. The lines presented in Fig. 3.12 are fits by an expression derived from equation (3.19), where the presence of

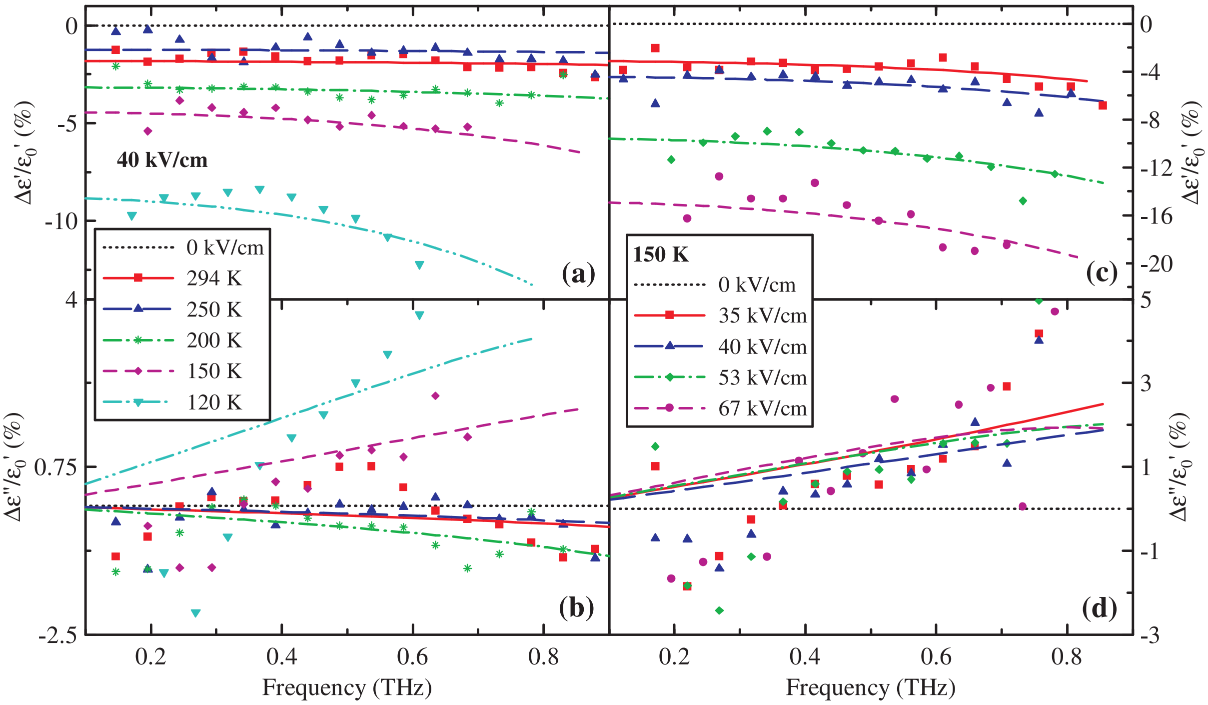

Figure 3.11: Relative field-induced changes in the complex dielectric function obtained for the parallel geometry. **(a)** and **(b)** E_{bias} = 40 kV/cm, varying T; **(c)** and **(d)** T =150 K, varying the bias field. Symbols: Experimental data. Lines: Fits by an underdamped harmonic oscillator.

both z and x components of the bias is taken into account:

$$\Delta\omega_0\left(E_{bias}\right) \approx \omega_0\left[\sqrt{1+3\beta_{\parallel}\left(\varepsilon_{vac}f_{osc}/\omega_0^2\right)^3 E_{z,bias}^2+\beta_{\perp}\left(\varepsilon_{vac}f_{osc}/\omega_0^2\right)^3 E_{x,bias}^2}-1\right]. \quad (3.23)$$

Here again, the only fitted parameter is the anharmonic coefficient $\beta_{\parallel}$, while $\beta_{\perp}$ is already known from the experiments performed in the perpendicular geometry. A relation between values of the bias field components $E_{z,bias}$ and $E_{x,bias}$ is obtained from the calculation of the electric-field distribution pattern shown in Fig. 3.5.

Nonlinear potential

Temperature dependences of $\beta_{\perp}$ and $\beta_{\parallel}$ together with data obtained by Christen et al. [193] in the microwave spectral range are shown in Fig. 3.13. According to our data, the anharmonic parameter $\beta_{\parallel}$ monotonically decreases with cooling, while Christen et al. reported its increase with cooling, at lower temperatures (below 80 K). The change in the slope of temperature variation of the anharmonic parameter is observed in a temperature

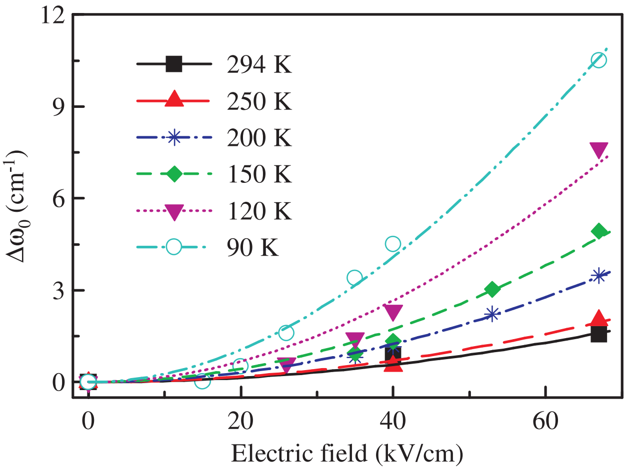

Figure 3.12: Electric-field-induced hardening of the soft-mode frequency in the parallel geometry at several temperatures. Symbols represent the values obtained from fits of the experimental spectra using a harmonic oscillator model (3.20); lines represent fits of the soft-mode behavior at each temperature by expression (3.23)

region near the ferroelastic antiferrodistortive phase transition which occurs at 105 K in STO. Therefore, we assume that this change of the slope in the temperature dependence of the anharmonic coefficient may indicate an influence of the structural phase transition on the soft-mode potential.

The values of the anharmonic coefficients are of the same order of magnitude as the values reported in [193]. However, the values of the anharmonic parameter $\beta_{\|}$ are slightly lower than those of $\beta_{\perp}$ at temperatures below 200 K. It should be noted that our values of $\beta_{\|}$ include a large experimental error due to the highly inhomogeneous character of the applied field in the parallel geometry and within this accuracy $\beta_{\perp} \approx \beta_{\|}$. We can state then that the soft-mode potential possesses an approximately spherical symmetry up to the fourth order of the power expansion. Our values of the anharmonic coefficients are also consistent with those estimated previously by Fleury and Worlock [191] from the Raman scattering spectra recorded at temperatures below 80 K. The authors also concluded that $\beta_{\perp} \approx \beta_{\|}$ at temperatures below 80 K.

3.2.5 Summary

The electric-field-induced tunability of the dielectric properties of bulk STO crystals was completely studied in a broad temperature range using THz time-domain spectroscopy. Two kinds of electrode structures deposited on the samples enabled the investigation of the field-induced tunability in two different orientations of the probing field with respect to the bias. Our theoretical description based on the Landau-Devonshire theory was

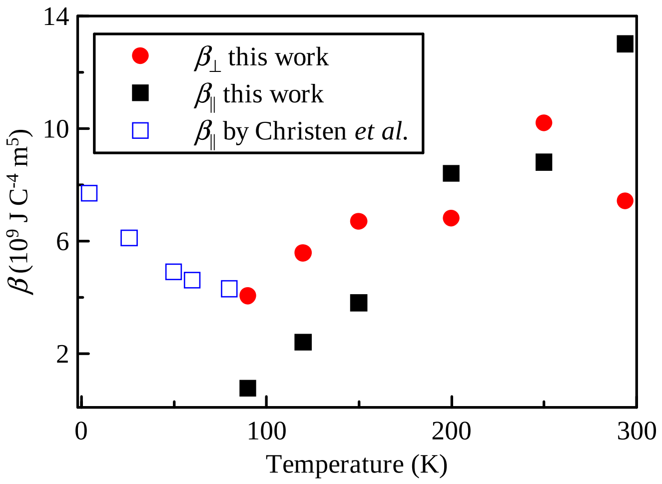

Figure 3.13: Resulting anharmonic parameters $\beta_\perp$ and $\beta_\parallel$ as functions of temperature (solid symbols) and $\beta_\parallel$ (empty symbols) taken from reference [193] for comparison.

elaborated for both experimental geometries. The experimental results and their fits to the theory strongly indicate that the electric-field tuning of STO single crystals is entirely due to the anharmonic character of the soft-mode potential. Moreover, absolute values of anharmonic coefficients and their temperature dependences were estimated by using two different electrode structures. The soft-mode dynamics fully determines the dielectric spectra in the THz and sub-THz frequency range, and this is observed in the whole investigated range of temperatures and of applied fields. No sign of an additional relaxation mode was observed even at the lowest temperatures. An appreciable tunability is demonstrated up to the room temperature.

These results can be used for or taken into account in developments of tunable structures (such as photonic crystals and/or metamaterials) controlled by an external voltage. An example of a tunable response of a photonic crystal (PC) exploiting the electric-field tunability of bulk STO dielectric properties is given in the next section.

3.3 Tunable photonic crystal

In this section we show one of possible applications of the electric-field-tunable dielectric properties of STO single crystals. We prepared a one-dimensional (1D) symmetric photonic crystal (PC) with STO defect layer in a similar way like it was done in reference [113]. However, instead of the temperature tunability of the STO dielectric properties we made use of their electric-field tunability. Appreciable defect-mode frequency shifts induced by reasonable values of an applied electric field were observed.

3.3.1 Structure specification

The investigated photonic structure was constructed of two identical Bragg mirrors and a defect layer enclosed between them (see Fig. 3.14). Our mirrors consisted of two alternating dielectric layers with a high refractive index contrast. In fact, several important circumstances should be kept in mind during the construction of the Bragg mirrors to obtain appropriate properties of the PC. First of all, a higher reflectance of the mirrors implies a stronger feedback. This results in a narrower defect mode and higher transmission losses in the defect layer which usually exhibits some losses. A compromise between a high peak transmission and an acceptable width of the defect mode should be found. Secondly, the lowest-frequency forbidden band as broad as possible is desired. This is achieved when the alternate dielectric layers forming the Bragg mirrors have the same optical thicknesses [201]. Finally, the widest tunability is reached when the defect layer, which usually possesses a high refractive index (n_D), is surrounded by layers with a low refractive index (n_L) [111].

We took the Bragg mirrors which were previously used for the investigation of thermally tunable defect mode in 1D PC [113]. Crystalline quartz served as the low-index material ($n_L \approx 2.1$), and undoped CeO_2 ceramics played the role of the high-index material ($n_H \approx 4.8 \approx 2.3\, n_L$). This ceramics shows low losses in the THz range and an almost temperature independent permittivity [202]. Each Bragg mirror was made of three quartz discs (each 230 μm thick) separated by two discs of CeO_2 ceramic (each 100 μm thick). The clear aperture of the mirrors was limited by the diameter of the ceramic discs which was 8 mm. All individual layers composing the Bragg mirrors were polished to an optical quality on both surfaces.

STO single crystals were purchased from Crystal GmbH and thinned down to 50 μm. The geometrical dimensions of the crystal used as the defect layer were $10\times10\times0.05$ mm^3. We deposited nanocrystalline Sb-doped SnO_2 films [199] with thickness of ∼200 nm on both sides of the STO plate. These films played the role of electrodes for application of the external bias field like they did in the characterization of the electric-field-induced tunability of STO single crystals in the perpendicular geometry. The areas of the sample covered by the thin-film electrodes were $\sim 8\times8$ mm^2 on both sides of the STO plate. Thin wires were put in contact with corners of both electrode square patterns (see Fig. 3.14) by a high-purity silver paint in a way that the wires were out of the contact surfaces of the STO plate and Bragg mirrors. Then, these wires were used to apply the electric field to the defect layer within the assembled photonic structure which was clamped between two metallic apertures electrically isolated from the PC.

3.3.2 Characterization and discussion

An example of measured transmission functions at 105 K and 150 K is shown in Fig. 3.15. The presented frequency range corresponds to the lowest-frequency forbidden band. At

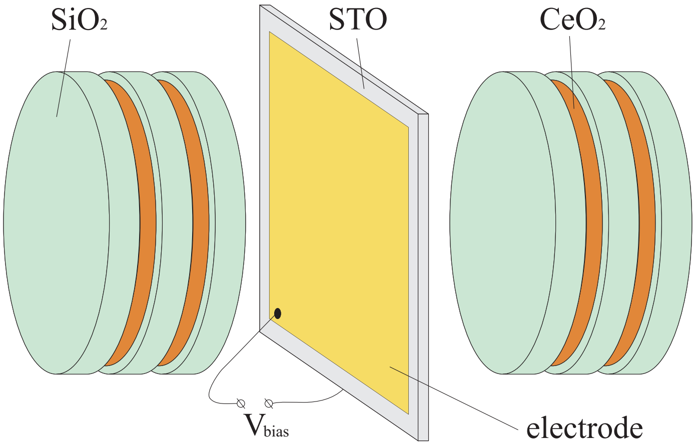

Figure 3.14: Scheme of the investigated photonic crystal with STO single crystal as a defect layer.

105 K it lies between 100 GHz and 215 GHz. A single defect mode appears in this range at ∼173 GHz for zero bias field. Upon an electric field application the defect-mode transmission peak shifts towards higher frequencies. Its amplitude increases with the bias. This behavior of the defect mode originates from the tunable dielectric properties of STO single crystals. Indeed, under the applied field, the permittivity of STO decreases (see Figs. 3.9a,c) leading to the frequency shift of the defect mode; while the simultaneous decrease of the dielectric losses of STO (see Figs. 3.9b,d) causes the increase of the defect-mode transmission. The field-induced frequency shift of the defect mode under the maximum applied field of 60 kV/cm at 105 K is 11.5 GHz with its linewidth of about 8 GHz. The relative tunability, calculated as a ratio of the tuning range and the central mode frequency, achieves 6.5 %. The defect-mode peak transmission is about −16 dB while in the forbidden band the transmission is lower than −30 dB.

Transmission functions calculated using a transfer matrix formalism [203] are shown along with the experimental data in Fig. 3.15. This calculation method allows one to determine the optical properties of any isotropic layered structure. In this formalism, the optical properties of each layer are introduced via a transfer matrix, which connects the tangential components of the electric and magnetic field at the input and output interface of the layer. Then, the transfer matrix of the whole structure is calculated simply as the product of transfer matrices of all individual layers. Finally, the reflection and transmission coefficients of the structure are calculated using the components of the transfer matrix of the structure. This approach simplifies the analysis of the propagation of electromagnetic radiation through a stratified medium; it provides a direct access to the optical properties of the medium without considering numerous partial reflections and transmissions of the radiation on each interface and their interferences.

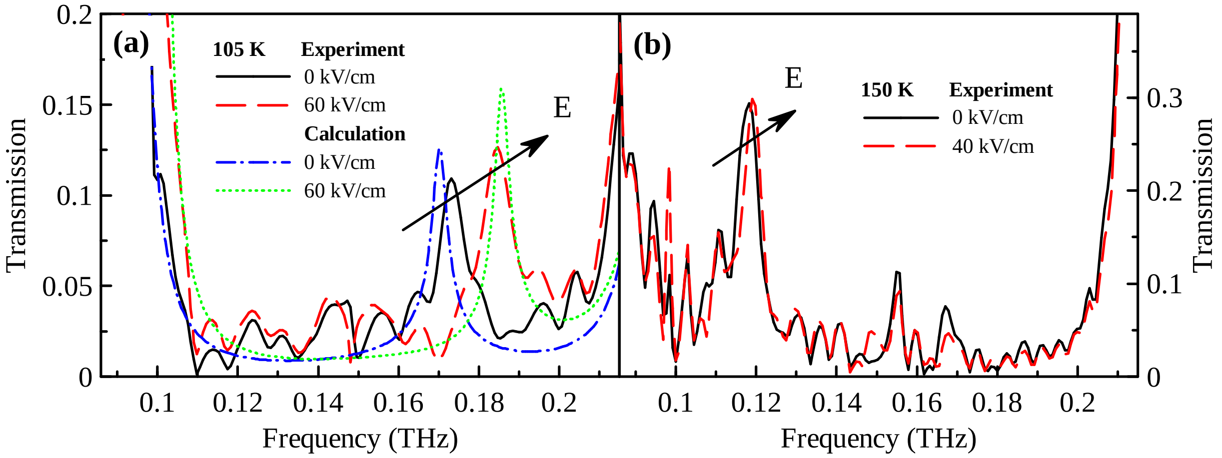

Figure 3.15: Amplitude transmissions of the investigated PC shown in the frequency range of the first forbidden band at 105 K **(a)** and 150 K **(b)**: solid and dashed curves are experimental data; dash-dotted and dotted curves are theoretically calculated data.

One can note a small frequency shift between the theoretical and experimental data. This small mismatch can originate in an uncertainty of the structural parameters of the PC. To prepare a very thin plate of STO embedded in the PC we used mechanical polishing, which is a procedure known to produce residual stress [204]. The latter may affect the lattice dynamics in STO crystals, and in this way change their steady-state (unbiased) dielectric properties and also their electric-field tunability, which are closely connected with the soft polar mode dynamics as it was shown in the previous section. Therefore, the absolute values of the biased and unbiased permittivity of 50-μm-thick crystals can slightly differ from one sample to another.

The fact that a theoretically predicted tunability ($\sim$10 %) is somewhat larger than the measured one ($\sim$6.5 %) can stem from a possible partial damage of the thin-film electrodes during the construction of the PC. Indeed, defects in the percolation of the conductive films and possible existence of small electrically isolated areas would decrease the volume of the sample influenced by the bias.

The measured and calculated electric-field-tunable transmission functions obtained at 105 K are shown in Fig. 3.16 in the frequency range including the two lowest-frequency forbidden bands. Despite some inconsistency, comparison of the observed and predicted electric-field-induced behavior of the defect mode demonstrates semiquantitatively the same pictures. The second forbidden band spreads from $\sim$400 GHz to $\sim$530 GHz, where one can distinguish two rather weak (≤ -30 dB) defect modes. The first one appears at about 480 GHz at the bias field off and shifts towards a higher-frequency allowed band upon electric field application. The second one splits out from the lower-frequency allowed band at about 20 kV/cm and shifts up to 450 GHz at 60 kV/cm bias. The relative

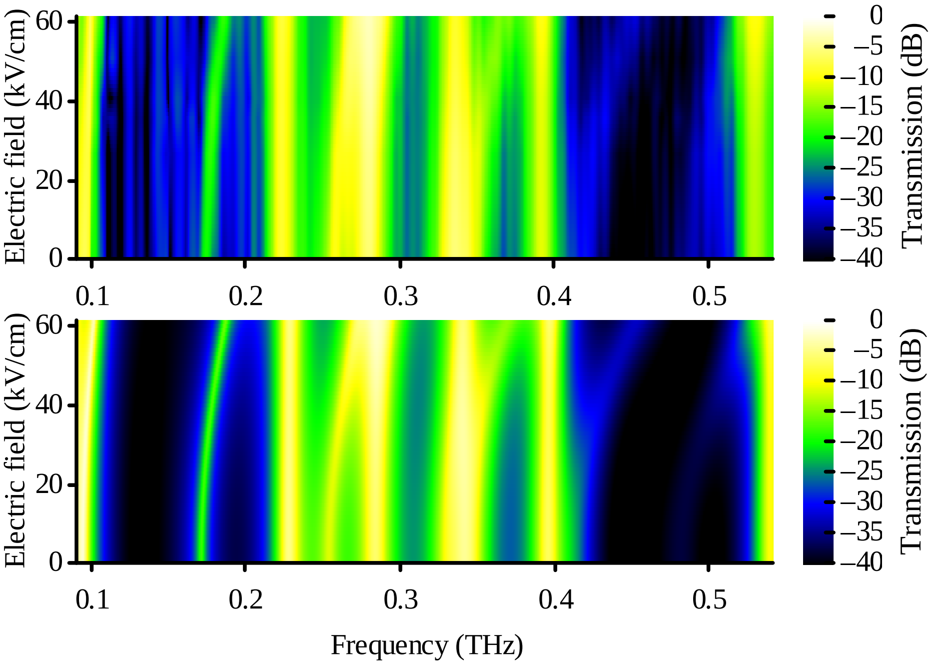

Figure 3.16: Electric-field-tunable transmission spectra shown in the frequency range including two lowest-frequency forbidden bands: upper panel – experimental data; lower panel – calculation.

tunability of these modes is about 10 %, which is comparable to that of the defect mode in the first forbidden band. However, the peak transmission of these modes is too low to be considered for applications.

As it can be seen in Fig. 3.15 the electric-field tunability of the defect mode decreases with increasing temperature, whereas the defect-mode peak transmission becomes higher due to the decrease of the dielectric losses in STO. For example, although the peak transmission of the defect mode at 150 K exceeds −9 dB the relative tunability of only ∼1 % is achieved at 40 kV/cm applied field (see Fig. 3.15b). However, the tunability of about 2 % with the transmission peak of about −13 dB is achieved at the same value of the external field at 120 K. Further cooling of the PC below 105 K is not reasonable because of a significant reduction of the defect-mode peak transmission owing to the rapidly increasing dielectric losses in STO. In addition, a ferroelastic cubic-to-tetragonal phase transition occurs at 105 K and it leads to an anisotropy of the dielectric properties of STO single crystals [183].

3.3.3 Summary

We have presented an example of a possible application of the electric-field-tunable dielectric properties of STO crystals; namely we have proposed a one-dimensional photonic crystal with the lowest-frequency forbidden band possessing a single defect mode which was tunable by the bias application. The relative tunability of 6.5 % was achieved at 105 K under the applied electric field value of 60 kV/cm. The phenomenon originates from the tunable permittivity of a 50-μm-thick STO crystal embedded as a defect layer in the photonic structure. The observed behavior is in accord with the model of the ferroelectric soft-mode behavior in STO single crystals under electric field described in the previous section.

3.4 Conclusions

Study of a broadband dielectric response of KTO ceramics presented in this chapter showed that their dielectric properties are very similar to those of KTO single crystals. This finding is quite surprising because it was expected that the polycrystalline ceramics displaying a bimodal distribution of the grain size would exhibit the dielectric properties inferior to those of single crystals, namely lower low-frequency permittivity values and higher dielectric losses. Indeed, we found that MW loss tangent acquired higher values compared to those in single crystals. This indicates an existence of defects in the KTO ceramics. However, the fact that the low-frequency permittivity almost reaches the value found in single crystals suggests that the permittivity is of intrinsic origin (i.e., due to the contribution of the polar phonons). We can conclude that the grain boundaries display a minor influence on the dielectric response of KTO ceramics in contrast to the previously studied STO ceramics [57, 182].

In the second section of this chapter we presented a comprehensive analysis of the electric-field tunability of the THz dielectric properties of STO single crystals. We have shown that the tunability originates in a highly anharmonic potential of the ferroelectric soft mode. Two different electrode structures deposited on samples allowed us to estimate anharmonicity of the soft-mode potential and even made a qualitative conclusion about its symmetry. The temperature and electric-field evolution of the THz dielectric spectra is fully governed by the soft-mode dynamics in STO single crystals. We did not observe any sign of an additional relaxation mode even at the lowest measured temperature. We have presented one of possible applications of the tunable dielectric properties of STO: we prepared a one-dimensional photonic crystal with an electric-filed-tunable defect mode in a forbidden band.

Investigation of possible electric-field tuning of the dielectric properties in the THz range of other appropriate bulk materials are believed to reveal qualitatively similar effects. KTO single crystals, KTO ceramics demonstrating the dielectric properties similar to those of single crystals (e.g., the ceramics described in the first section of this chapter), $Ba_xSr_{1-x}TiO_3$ (BST) crystals and ceramics are dielectrics having suitable properties for an electric field-tunability in the THz range. In fact, we put efforts in deposition of metallic electrodes with an interdigitated structure on BST ceramics of different compositions. The deposition of electrodes onto ceramics requires extreme care because of a high fragility of usually less then 100-μm-thick ceramic plates needed for THz transmission measurements. For the moment, the imperfections of the ceramic surface did not allow us to obtain any functional electrode structure.

We believe that the results presented in this chapter will induce further investigations of possible electric-field-tunable dielectric properties in related materials and that the tunability of STO THz properties already characterized in this chapter will find their applications in tunable structures like photonic crystals or metamaterials.

Chapter 4

Results on thin films

Thin films of incipient ferroelectrics

Incipient ferroelectrics have been intensely studied due to their specific dielectric properties with purpose of their application in microwave tunable devices. A possible control over a paraelectric-to-ferroelectric phase transition temperature (T_C) in the material is a very desirable option, which can improve the device performance. One possibility of adjusting the T_C is a chemical substitution. This is the case of $\mathrm{Ba}_x\mathrm{Sr}_{1-x}\mathrm{TiO}_3$, which are widely investigated materials with the dielectric constant tunable by applied bias [23]. However, chemical substitution introduces disorder, compositional fluctuations and clustering, and it breaks the translational symmetry. All these effects locally change the inter-ionic interaction; as a result, a more complex chemical composition can broaden the phase transition. In such materials, the dielectric properties can be less suitable for tunable device performance.

Another parameter leading to a modification of T_C in ferroelectrics and quantum paraelectrics is the strain [176, 205, 206]. An intelligent way to obtain a permanently strained material is an epitaxial deposition of a thin film on a substrate slightly lattice-mismatched with the film material. For example, it was shown [66] that a thin film of SrTiO_3 (STO) epitaxially deposited on DyScO_3 (DSO) or on $(\mathrm{LaAlO}_3)_{0.29}\times(\mathrm{SrAl}_{0.5}\mathrm{Ta}_{0.5}\mathrm{O}_3)_{0.71}$ (LSAT) undergoes a paraelectric-to-ferroelectric phase transition. Such a strain-induced change in T_C can reach hundreds of degrees. In the case of STO deposited on (110)-oriented DSO substrate the film experiences an in-plane biaxial tensile strain, and the spontaneous polarization in the ferroelectric phase develops in the plane of the film. STO films deposited on an LSAT substrate are characterized by a biaxial compressive strain leading to an out-of-plane direction of the polarization.

Thin STO films grown on (110) DSO substrates are of particular interest among scientists because the ferroelectric phase transition occurring near $\sim$300 K leads to a highly enhanced dielectric tunability close to the room temperature [66, 207–211].

4.1 $SrTiO_3$ films on $DyScO_3$: from single layer to heterostructures

In this section a comprehensive analysis of THz dielectric properties of thin film structures consisting of STO and DSO layers is given. It includes a detailed study of THz dielectric response of the thin film systems at various temperatures and applied electric fields using time-domain THz spectroscopy. This allows us to determine the paraelectric-to-ferroelectric phase transition temperature and to retrieve the most important parameters describing lattice dynamics of the studied structures.

Here we also explored the possibility to increase the total thickness of strained STO films while maintaining their strain-induced dielectric properties. The main problem, excluding all experimental challenges, of thicker strained epitaxial films, is that the strain relaxes with increasing thickness of the film. It has been shown by Zhai et al. [212] that the lattice strain relaxation in STO thin film deposited on (110) DSO occurs mainly at the distance of $50-90$ nm from the substrate surface. For thicknesses larger than 100 nm the surface layers of the film possess the same lattice parameters as those of a free-standing STO crystal. In addition, there is a lot of structure defects like dislocations in the range where the relaxation occurs. These defects can affect the dielectric properties of the material. Taking into account these facts we systematically studied multilayer structures consisting of a variable number of STO/DSO bilayers where the DSO layers were intended to retain the strain in STO films at larger distances from the substrate.

4.1.1 Sample preparation and experimental issues

Thin film structures were prepared by Dr. J. Schubert in Jülich using pulsed laser deposition (PLD) on (110)-oriented DSO substrates. PLD growth took place in an on-axis geometry using a KrF excimer laser with a wavelength of 248 nm, a pulse width of 25 ns and a fluence of 2.5 J cm^{-2} [213]. An STO single crystal and a DSO polycrystal were used as targets. The DSO substrates with geometrical dimensions of $10\times10\times0.9$ mm^3 were positioned directly onto a SiC resistive heater. Molecular oxygen partial pressure of 0.2 Pa was maintained in the chamber during the deposition.

DSO is orthorhombic with lattice constants $a = 5.440$ Å, $b = 5.713$ Å, and $c = 7.887$ Å. It is not ferroelectric down to 4 K. The (110) DSO surface has a pseudo-square mesh with an in-plane lattice spacing $a' = 3.944$ Å. A comparison of this spacing with the lattice parameter of a high-quality cubic STO ($a = 3.905$ Å) shows a tensile lattice mismatch of $+1.0$ % at room temperature. This approach enables the epitaxial growth of uniformly strained thin films.

An interdigitated gold electrode structure was deposited onto each sample for application of a bias electric field (Dr. G. Panaitov, Jülich). The electrode structure covered about one half of the sample surface (see Fig. 4.1). It was prepared by lift-off photolithog-

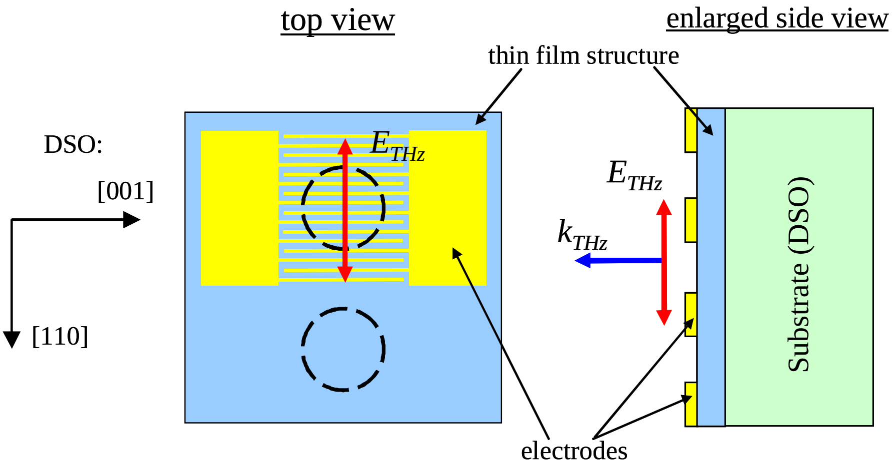

Figure 4.1: Scheme of the sample geometry and of the orientation of the electric field vector and wave vector of the incident THz radiation. In the top view two positions of an aperture are shown by dashed curves. They correspond to the measurements of the temperature dependence at zero field (position outside the electrode pattern) and of the electric field dependence (position inside the electrode pattern) of the dielectric properties.

raphy and subsequent deposition of 20-nm-thick Nb film (adhesion layer) and 300-nm-thick Au film by dc magnetron sputtering. The 6×6 mm^2 interdigitated structure consisted of 5-µm-wide gold stripes and 15-µm-wide gaps. The electrode fingers were parallel to the [001] direction of the DSO substrate. The experiments were made under normal incidence, i.e., the wave vector of the THz radiation was perpendicular to the plane of the thin film structures. The samples were oriented to have the electric field vector of the probing THz field perpendicular to the electrode fingers (see Fig. 4.1). In this experimental geometry the THz field is polarized along the transparent axis of a birefringent DSO substrate (with a lower refractive index and lower losses in the THz range).

All samples can be divided in two series; each series was prepared at once from a preselected set of substrates. Initially, substrates of both series were polished on both sides to an optical quality and with a precise control of their thickness (±2 µm) and their plane-parallelism (±1 µm). Then, all of the DSO plates were measured using time-domain THz spectrometer to estimate their thicknesses as precisely as possible. The next step was the deposition of the thin film structures. The interdigitated electrode structure was prepared on the samples from the first series (*i*) just after the thin films deposition. The experiments of the temperature dependence of the dielectric properties without field should have been done outside the electrode area (see Fig. 4.1). For this reason a relatively small aperture of 3 mm was used. For the second series (*ii*) the temperature dependence of dielectric properties of the thin film structures was measured before the deposition of metallic electrodes. As the whole area of the samples was available for these measurements, we used a larger aperture of 6 mm. This difference is reflected in the precision of the experimental data, namely the part of the spectra below 0.4 THz.

Altogether, seven samples were prepared and completely analyzed in terms of temperature and field dependence of the dielectric properties; their labels and detailed descriptions follow:
(*i*) **series**

1×100 100-nm-thick single layer of STO film.

2×50 Structure consisting of two bilayers of STO/DSO, where each single layer has a thickness of 50 nm. The total thickness of STO is 100 nm.

3×50 Structure consisting of three bilayers of STO/DSO, where each single layer has a thickness of 50 nm. The total thickness of STO is 150 nm.

4×50 A Structure consisting of four bilayers of STO/DSO, where each single layer has a thickness of 50 nm. The total thickness of STO is 200 nm. The results obtained for this sample were also discussed in detail in [214].

(*ii*) **series**

4×50×2 Identical thin film structures deposited on both sides of the substrate. Each structure is similar to that of 4×50 A sample. The interdigitated electrodes were sputtered on one side of the sample, therefore, the total thickness of STO film taken into account in the field dependent measurements is 200 nm, while in the measurements without field it is 400 nm.

6×50 Thin film structure consisting of six bilayers of STO/DSO with 50-nm-thick each single layer.

8×50 Thin film structure consisting of eight bilayers of STO/DSO with 50-nm-thick each single layer.

4.1.2 Experimental results

A large number of spectra was measured and analyzed in order to characterize all the thin film structures described above. All the measurements were done in two steps. First, equilibrium dielectric properties (without the bias field) of each sample were studied at different temperatures. Second, field-induced dielectric properties were measured at the same set of temperatures.

An example of time-domain THz wave forms measured with a DSO substrate and a 6×50 sample before the electrodes deposition is shown in Fig. 4.2a. One can see directly from the figure that the THz signal measured with the sample is retarded in time and

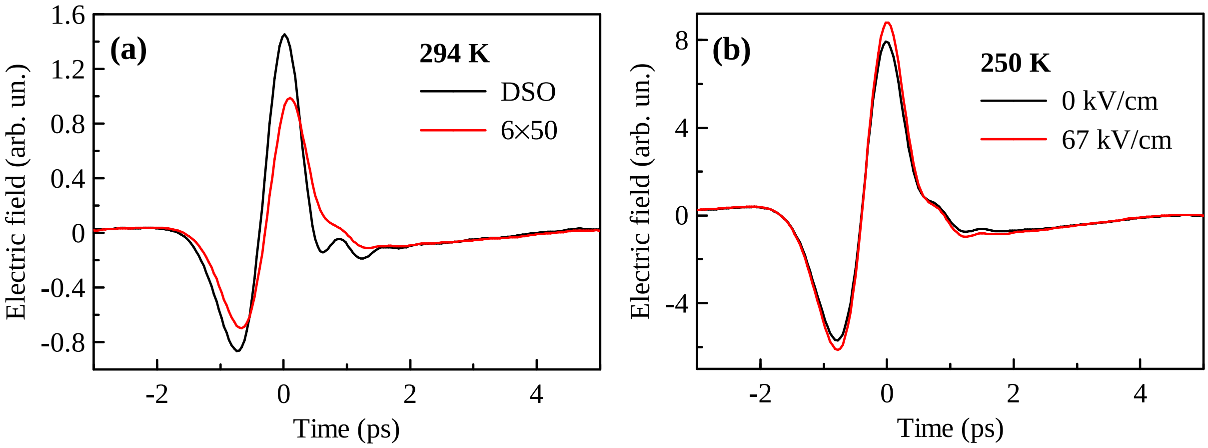

Figure 4.2: Examples of measured THz wave forms. **(a)** Room temperature wave forms transmitted through a bare DSO substrate (black curve) and through a DSO with the 6×50 multilayer (red curve). **(b)** Wave forms transmitted through the 6×50 sample at 250 K with the bias field off (black curve) and on (red curve).

has a lower amplitude due to higher refractive and absorptive indices of STO than those of DSO. In Fig. 4.2b we show a comparison of the wave forms measured at 250 K with the bias electric field off and on. Here, one observes an increased amplitude of the THz signal measured with the biased sample. This phenomenon originates from the soft-mode frequency hardening (increase) under the external electric field and the corresponding decrease of STO permittivity and losses in the THz frequency range. A detailed analysis of the spectra is provided below.

The experiments consisted of two consecutive measurements: of a signal wave form and of a reference wave form. In the case of the equilibrium measurements of the dielectric properties (1st step), the reference wave form was measured using a bare DSO substrate, and the signal wave form was measured using a sample with the thin film structures. In the case of measurements of the electric-field-induced properties (2nd step), the reference wave form was measured using the sample without an electric bias, whereas the signal wave form was measured with a non-zero bias. In both experimental steps, a ratio of the Fourier transforms of the signal and reference wave forms was calculated. In the equilibrium experiments, this ratio provides a complex transmission function of a thin film structure, which is analytically described by equation (2.11). In the experiments with an applied electric field, the ratio of the Fourier transforms of the signal and reference wave forms can be regarded as a complex transmission function of the field-induced changes in the dielectric properties of thin film structures. It is analytically described by equation (2.13).

The wavelength of the THz radiation is much larger than the optical thickness of

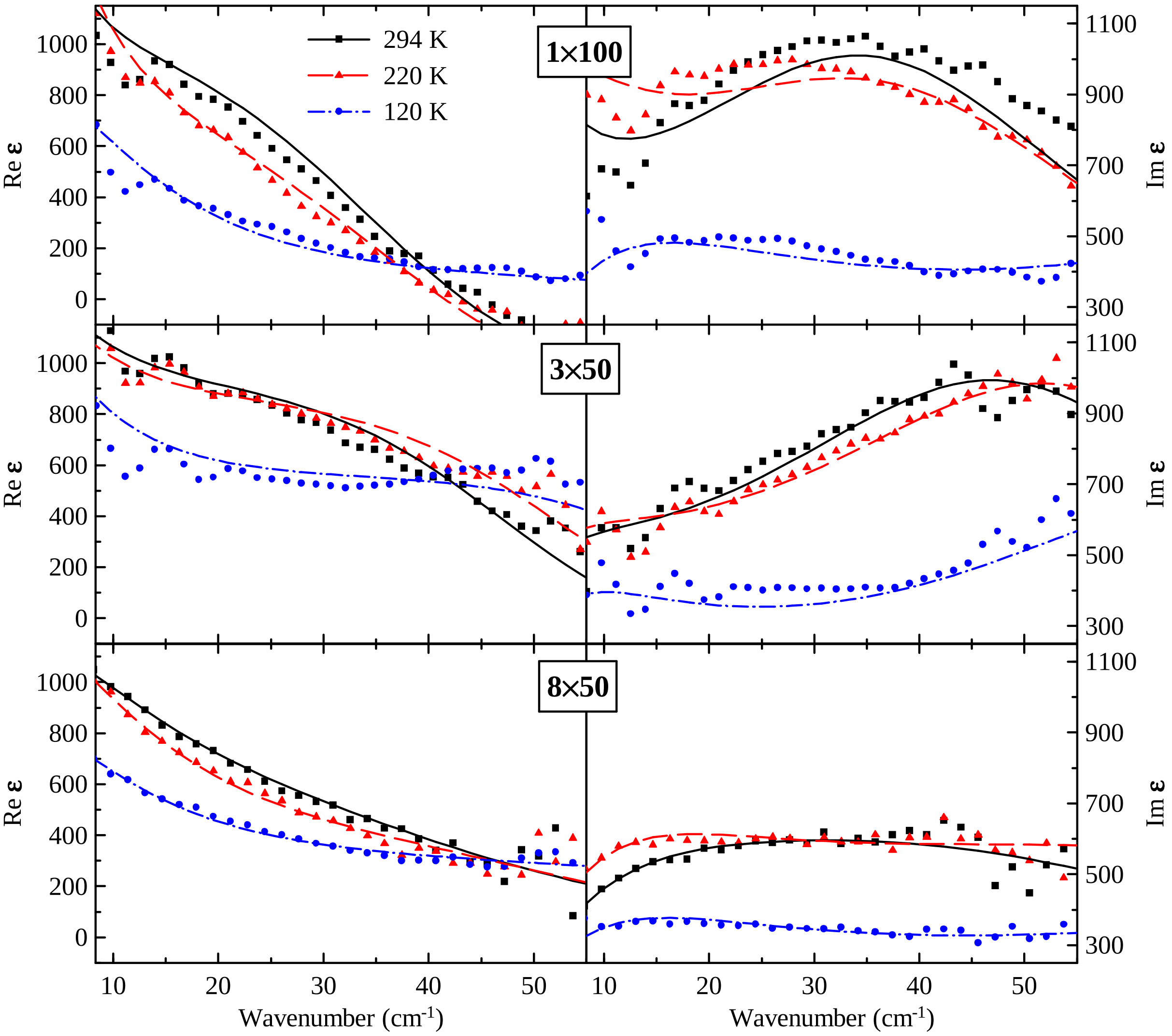

Figure 4.3: Examples of the measured dielectric spectra for selected thin film structures at three different temperatures. Symbols are experimental data; lines are fits with the formula (4.2).

separate layers within the investigated multilayer structures. Therefore, we can apply the effective medium approach for the calculation of the dielectric function of STO thin films from the measured spectra. In our evaluations, we treated the multilayer of STO/DSO as a STO/DSO bilayer with summed thicknesses of each material. The validity of this approach was previously verified [215] using the transfer matrix formalism for layered media by calculating and comparing the transmission functions of a multilayer and of the equivalent bilayer.

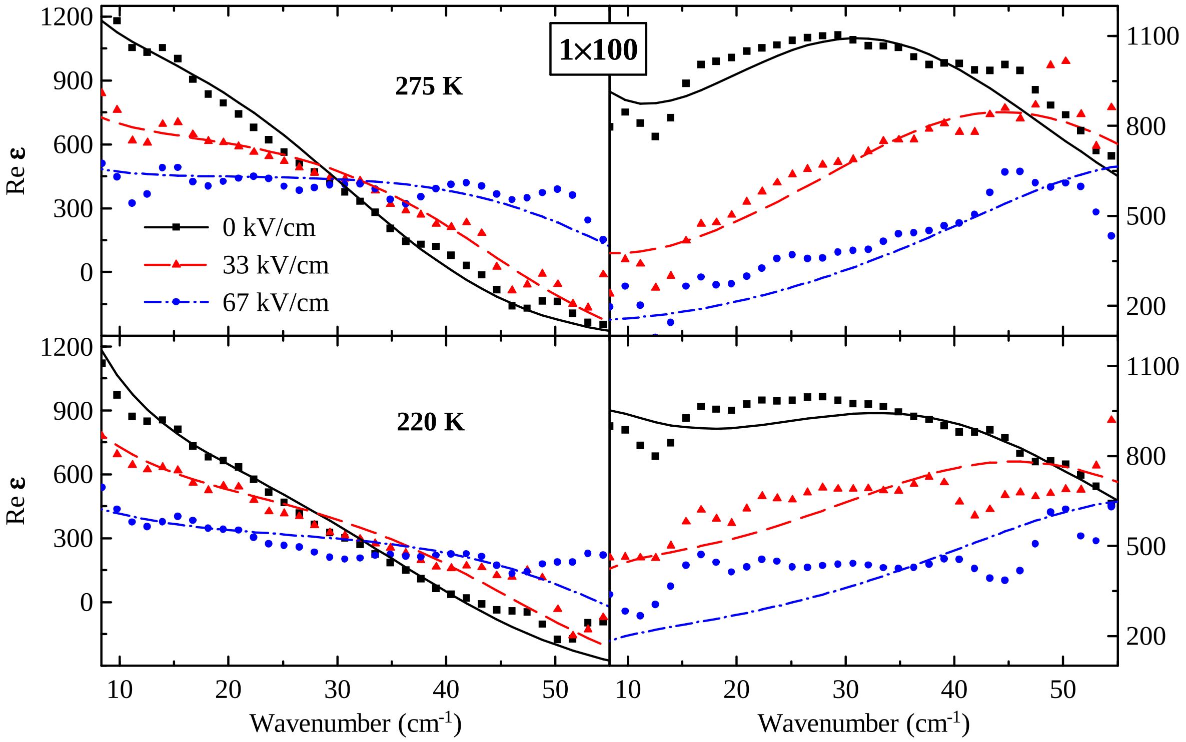

Figure 4.4: Selected dielectric spectra of 1×100 sample for several values of the bias field at 275 K and 220 K. Symbols: experimental data; lines: fits with the formula (4.2).

The measured equilibrium dielectric spectra of selected samples at three different temperatures are shown in Fig. 4.3. It should be mentioned that all the spectra of each sample are qualitatively similar to those which are shown in Fig. 4.3. They reach a permittivity value of about (or somewhat larger in some cases) 1000 at 10 cm^{-1} close to the room temperature. All loss spectra (Im ε) show rather broad features.

In the second step (measurements with the electric field) each sample was put into an optical cryostat equipped with wires for the electric field application to the deposited electrode structures. Then, a set of wave forms was measured under different electric field applied to the sample at each temperature. In Fig. 4.4, Fig. 4.5 and Fig. 4.6 we show selected dielectric spectra of three samples for several temperatures and values of the bias electric field. One can observe qualitatively similar electric-field-induced behavior for all the samples: the real part of the permittivity at lower frequencies (below $\sim$30 cm^{-1}) decreases upon the electric field application; and the dielectric losses decrease in the whole experimentally achievable spectral range under the bias field. In addition, electric-field-induced changes are significantly weaker at temperatures below 200 K (see Fig. 4.5 and Fig. 4.6). The other samples which are not shown in the figures show similar behavior of

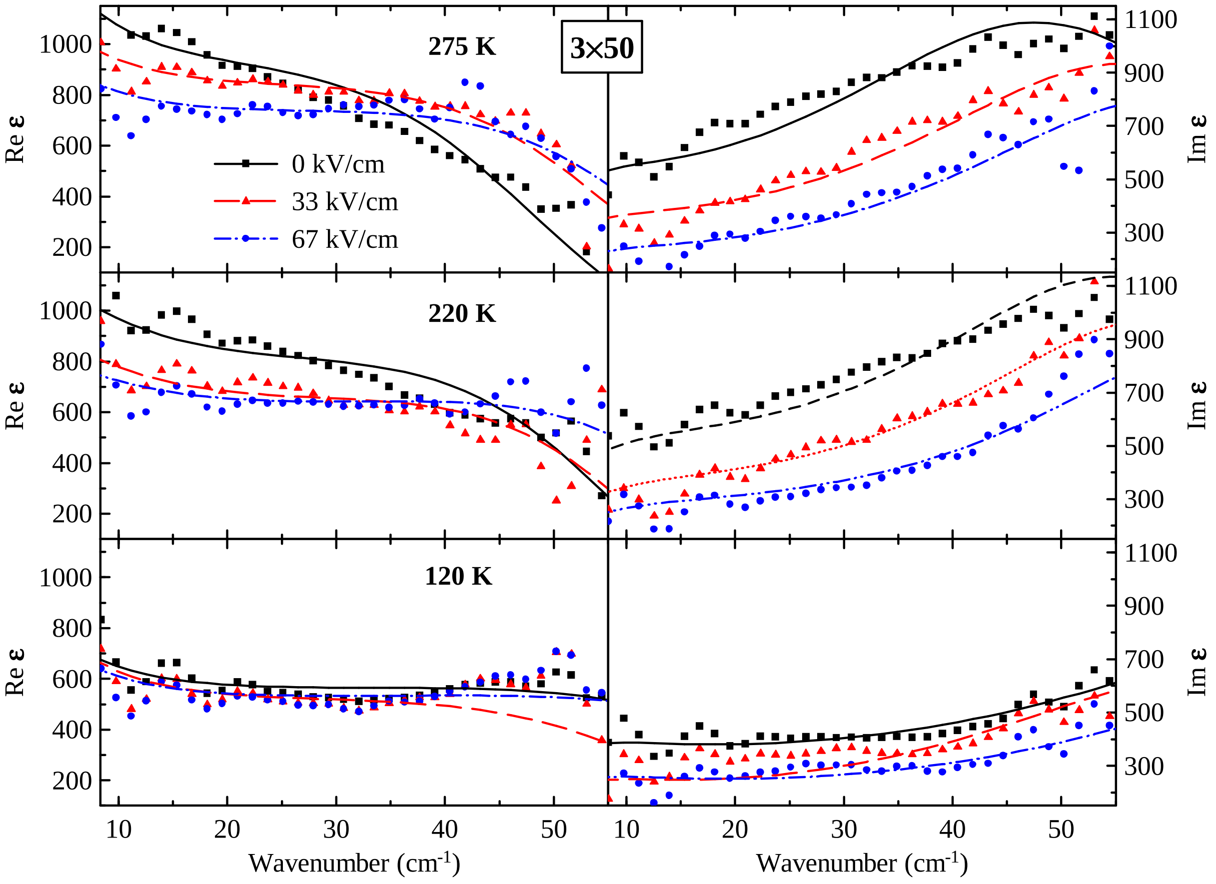

Figure 4.5: Selected dielectric spectra of 3×50 sample for several temperatures and bias field. Symbols: experimental data; lines: fits with the formula (4.2).

the dielectric properties with temperature and the applied electric field. Some dielectric spectra of the 4×50 A structure can be found in reference [214].

4.1.3 Complete analysis and discussion

Modeling of the dielectric response

In order to describe the measured spectra we consider a pair of linearly coupled lattice modes. A low-frequency excitation ($\sim$10 cm^{-1}) of relaxation type (called central mode) was observed in THz spectra at room temperature in the previous studies of similar thin film systems [215,216]. This excitation was shown not to be directly coupled to the polarization at room temperature (i.e. zero relaxation strength), but it appears in the dielectric spectra owing to its linear coupling to the soft mode. This behavior was demonstrated

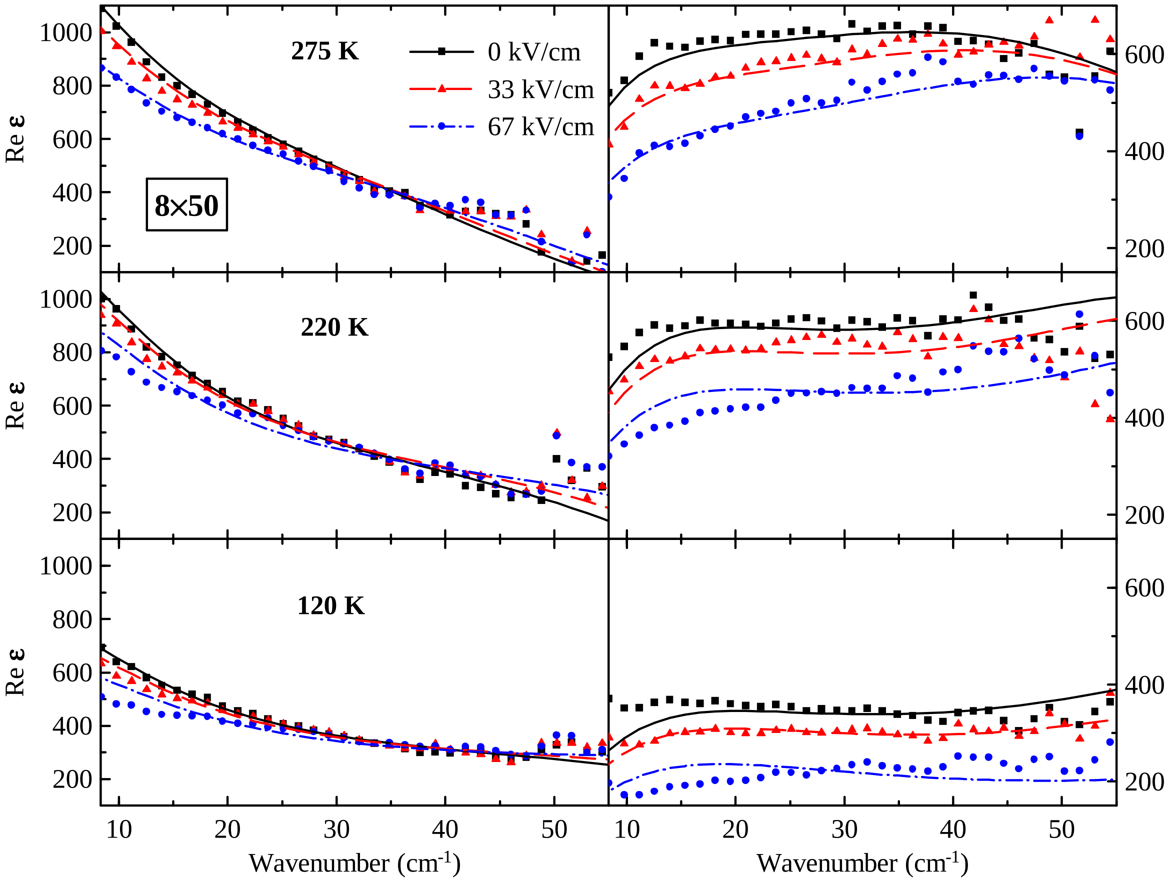

Figure 4.6: Selected dielectric spectra of 8×50 sample for several temperatures and bias field. Symbols: experimental data; lines: fits with the formula (4.2).

for the paraelectric phase of various strained STO layers [215]. Within this approach the relaxation-type excitation was modeled by a simple Debye relaxation with frequency γ, and the soft mode was described as a damped oscillator with a bare eigenfrequency ω_0, damping Γ, and oscillator strength f_{osc}. The analytical expression of the model used for fitting of the experimental spectra measured at room temperature in [214, 215] has the following form:

$$\varepsilon(\omega) = \frac{f_{osc}(1 - i\omega/\gamma)}{(\omega_0^2 - \omega^2 - i\omega\Gamma)(1 - i\omega/\gamma) - \delta^2} + \varepsilon_\infty, \tag{4.1}$$

where δ is a coupling constant, and ε_∞ is a contribution of higher-frequency excitations to the permittivity. This model yields that the appearance and strength of the relaxation mode in the THz spectra are strongly correlated with the soft-mode frequency. The contribution of the relaxation (with $\gamma \approx 10$ cm^{-1}) to the permittivity should not be observed for a high soft-mode frequency (i.e., $\omega_0 \gtrsim 90$ cm^{-1} as it was found in [215]). In contrast, its contribution becomes dominating when the soft-mode frequency is low ($\omega_0 \lesssim 50$ cm^{-1}). However, the fingerprints of the relaxation mode in the dielectric spectra were also clearly observed at low temperatures in the ferroelectric phase where the soft-mode frequency is high [214]; this is obvious in Fig. 4.6 (sample 8×50, 120 K).

This lead us to a more general formula [217, 218], where the bare relaxational mode contributes directly to the permittivity

$$\varepsilon(\omega) = \frac{f_{osc}(1 - i\omega/\gamma) + g(\omega_0^2 - \omega^2 - i\omega\Gamma) \pm 2\delta\sqrt{f_{osc}g}}{(\omega_0^2 - \omega^2 - i\omega\Gamma)(1 - i\omega/\gamma) - \delta^2} + \varepsilon_\infty, \tag{4.2}$$

where g is the relaxation mode strength, which is proportional to the squared effective charge of the mode. The "±" sign in the numerator describes whether the effective charges of the soft mode and central mode are the opposite (+) or the same (−).

The origin of the central mode (CM) which appears in the spectra of many ferroelectric materials in the vicinity of a phase transition of the displacive type is still a subject of scientific debate [15, 219–221]. On the one hand, a central mode can be induced by defects; on the other hand, recent ab-initio calculations show that in BST family the CM is of intrinsic origin. In these simulations [220–222] the coexistence of the oscillator and relaxator in both para- and ferroelectric phases directly stems from a strongly anharmonic SM behavior. Both excitations are described within a unit cell by a single degree of freedom which is connected to the SM eigenvector [220–222]. One can understand the relaxation mode as an additional low-frequency decay channel of the soft mode, which is associated with a specific anharmonicity (side minima) of the multiminimum soft-mode potential.

Results of fits

All the dielectric spectra of the investigated samples were fitted by the model (4.2). Since this model includes a lot of parameters there is no way to determine all the parameters independently for each spectrum. Therefore, we decided to fix values of most parameters as independent of temperature (or of applied field) and to fit several spectra simultaneously. We call this approach a global fit, because values of many parameters are common for all spectra involved in this fit. For each sample a set of global fits was performed.

Initially, a global fit of all equilibrium dielectric spectra (all temperatures at zero-bias field) was performed, where we assumed that Γ, f_{osc}, γ and δ are temperature independent, and $g(T)$ and $\omega_0(T)$ are temperature dependent. The dependences $\omega_0(T)$ and $g(T)$ are the key results of this part of the data analysis; they entirely describe the temperature evolution of the THz dielectric response. The high frequency permittivity ε_∞ was fitted for each spectrum independently. Note, that ε_∞ has no physical meaning in our fits as its value is the subject of a large uncertainty. In fact, the baseline of the real permittivity of thin films can be determined only with a very large experimental error as discussed in the chapter devoted to the experimental techniques (page 40).

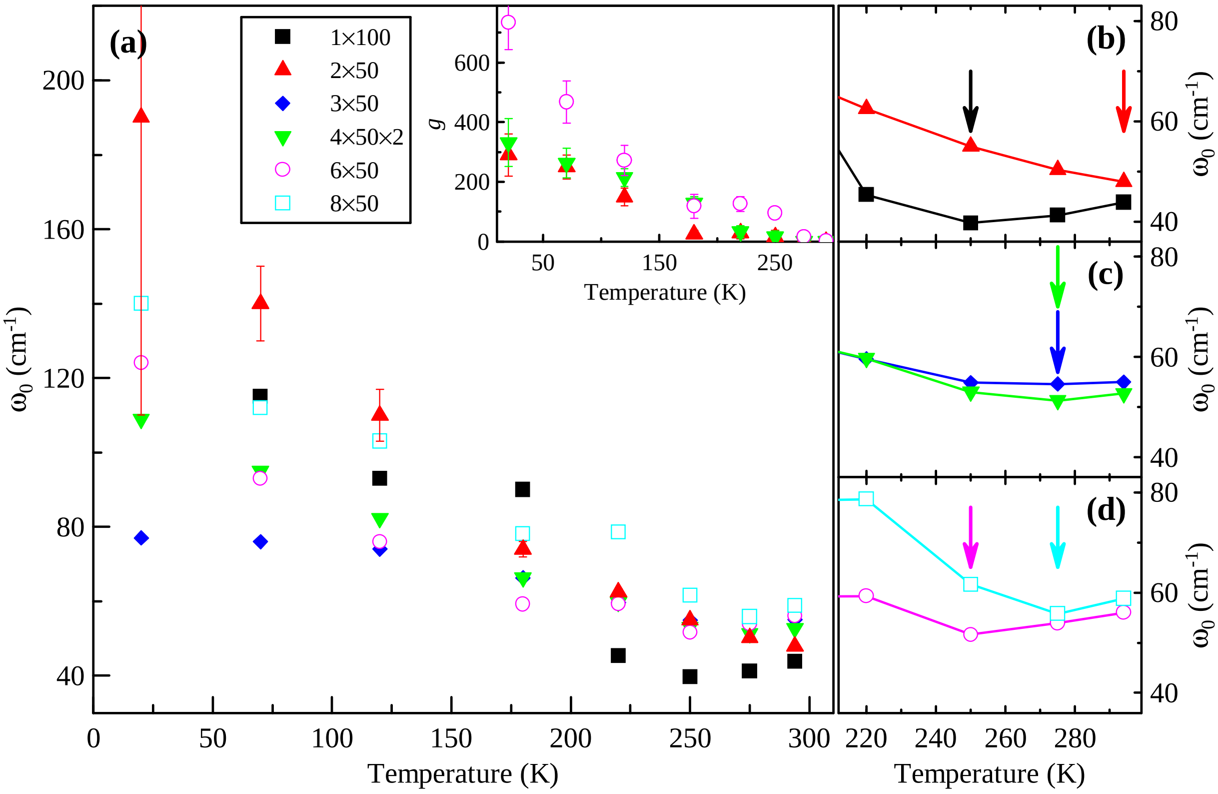

Figure 4.7: **(a)** Temperature dependence of the soft-mode frequency as obtained from the fits of the equilibrium spectra of the investigated samples. Inset: temperature dependence of the relaxation strength for selected samples. **(b)**,**(c)**,**(d)** The same data shown on an enlarged temperature scale in the vicinity of the phase transition temperature (T_C). Arrows denote T_C. All values shown in the figure are provided by the fits with the formula (4.2). The error bars shown in the figure correspond to the errors provided by the global fits. The error bars shown for the soft-mode frequency represent the typical errors for the corresponding values of ω_0.

The formula (4.2) was found to fit the data better with the sign "+". This sign corresponds to the opposite effective charges of the soft and central modes leading to a destructive interference in the spectral range between their resonance frequencies.

The resulting fits are shown along with the measured spectra in Fig. 4.3. The values of the soft-mode frequency obtained from the fits are presented in Fig. 4.7. Analyzing the temperature behavior of the soft-mode frequency one can assess the phase transition temperature of each thin film structure, as a temperature where the SM frequency reaches its minimum. It should be mentioned that the soft-mode frequency provided by the fit at lower temperatures (below 120 K) should be considered as very approximate. The soft-mode frequency is already rather high (above the accessible spectral range), and only its low-frequency tale contributes to the dielectric permittivity probed in our experimental setup. In addition, a high damping of the soft mode leads to its almost constant or weakly frequency-dependent contribution to the permittivity in the experimental spectra. Therefore, our model becomes less sensitive to the value of the soft-mode frequency at lower temperatures.

The fits of the equilibrium data showed that the relaxation strength acquires nonzero values only at lower temperatures, namely when the STO film is in the ferroelectric phase according to the temperature behavior of the soft-mode frequency (see the inset in Fig. 4.7a). Moreover, $g(T)$ grows with cooling below the transition temperature. The 2×50, 3×50 and 4×50×2 samples exhibit the maximum relaxation strength value of about 300 at 20 K, whereas 1×100, 6×50 and 8×50 samples show somewhat larger values in the range from 500 to 750. The values of temperature independent parameters (Γ,δ,f_{osc}) are very similar for each sample ($\Gamma \approx 70\text{cm}^{-1}$, $\delta \approx 32\ \text{cm}^{-1}$, $f_{osc} \approx 2.36\times10^{6}\ \text{cm}^{-2}$).

In this way we determined equilibrium values (without field) of all the fitting parameters for all the studied samples. In the next step, we fitted an evolution of the dielectric spectra upon an applied electric field. We formed sets of the measured spectra, where each set included spectra obtained for one sample at one temperature under varied value of the bias. Then, we again performed a global fit of each such set of the spectra with the model (4.2). These fits for selected samples at several temperatures and bias field values are presented along with the experimental data in Fig. 4.4, Fig. 4.5, and Fig. 4.6. In these global fits f_{osc} was fixed to the value of $2.36\times10^{6}\ \text{cm}^{-2}$ found in the previous fits, which is in agreement with the value found in STO single crystals [24]; the parameters Γ, δ and g were fitted independently for each global fit (i.e. for each temperature) in order to compare these values with the previously found ones from the measurements without the bias field. Such a comparison provides an approximate measure of the robustness of the parameter determination. The coupling constant δ and the oscillator strength g acquired the values very close to those obtained from the fits of the equilibrium data with a relative deviation not larger than 15 %. The SM damping Γ and the relaxation frequency γ exhibited some nontrivial temperature dependencies, which are discussed below. The key parameter of these fits is, however, the soft-mode frequency $\omega_0(T, E)$, which is the only parameter that was assumed to be electric-field dependent. The complete picture of the soft-mode frequency behavior with temperature and electric field in the 4×50×2 sample is presented in Fig. 4.8. The electric-field-induced tuning of ω_0 obtained at 70 and 20 K is not presented because of the insensitivity of the THz spectra to small changes in the soft-mode frequency at lower temperatures, as discussed above.

Discussion

From the temperature behavior of the soft-mode frequency shown in Fig. 4.7 one can conclude that the ferroelectric phase transition occurs at temperatures slightly below the

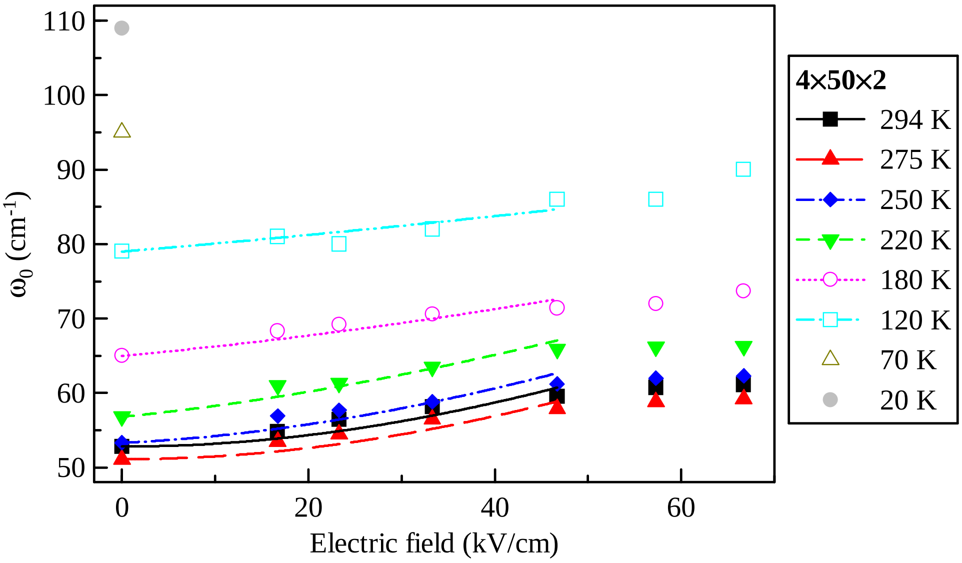

Figure 4.8: Electric-field induced tuning of the soft-mode frequency in 4×50×2 sample. Symbols are the data corresponding to the soft-mode frequency obtained from a fit of experimental spectra by model (4.2); Lines are fits of $\omega_0(E)$ by (4.7).

room temperature (250−294 K) in all the investigated thin film structures with the exception of 2×50. Its phase transition temperature cannot be rigorously determined because the minimum value of the soft-mode frequency is observed at the edge of the measured temperature range (see Fig. 4.7b). However, taking into account the low value of the soft-mode frequency at room temperature and general trends of the soft-mode temperature behavior for the other samples we can conclude that the transition occurs with a high probability somewhere in the range between 294 and 310 K. The estimated phase transition temperatures and the corresponding frequencies of the soft mode for all samples are summarized in Table 4.1.

Despite the significant strain relaxation in the relatively thick STO layer, the 1×100 structure shows the lowest soft-mode frequency (39.5 cm^{-1}) among the others. The 2×50 sample acquires also a low minimum value of the soft-mode frequency especially when one takes into account its possible further softening with the temperature increase. The 2×50 structure has the highest observed phase transition temperature. This is probably related to a more homogeneous strain distribution in two separate 50-nm-thick layers of STO than that in a 100-nm-thick layer of 1×100 sample or in thicker multilayer systems, where a gradual reduction of the strain towards the top-most layer can take place. The structures with more than 2 layers of STO exhibit slightly higher soft-mode frequencies. This fact can be again connected to an inhomogeneous distribution of the strain over the multilayer structure thickness, which eventually results in slightly different lattice dynamics in the individual STO layers within one multilayer structure.

The oscillator strength f_{osc} in the model (4.2) was found to attain a value of 2.36×10^6 cm^{-2} for all investigated structures and to be temperature independent. In fact, the same value of the oscillator strength was found for the STO single crystals [24]. The soft-mode damping acquired different values from sample to sample, which were, however, in the range between 43 and 90 cm^{-1}. We observe a general tendency of an increase of Γ for thicker samples. The damping value of each sample varied no more than by 50 % with temperature, but no clear trend in the temperature dependence was observed. In our fits we assumed that Γ is electric field independent. Nevertheless, referring to the data from the study of the dielectric tunability in a single crystal of STO we can suppose that there is a field-induced change in the SM damping due to an inhomogeneous applied electric field (see Fig. 3.5a). However, in the case of the thin film structures this effect is expected to be substantially weaker due to a large inhomogeneous broadening of the SM in the film

Sample	1×100	2×50	3×50	4×50×2	4×50A	6×50	8×50	20×10*	SC$^\diamond$
d_{STO} [nm]	100	100	150	200*	200	300	400	200	–
$\omega_0(0)$[cm^{-1}]	39.5	46.6	54	51.1	47	48	59.1	65	38.5
$\Delta\omega_0(67)$[cm^{-1}]	21.3	21.4	10.9	8.1	15.5	8.7	6.6	5	10.5
ε_0 (0)	4600	2010	1420	1760	2700	2050	1370	1050	1590
$\Delta\varepsilon_0$ (67)	3920	1380	440	600	1650	720	330	150	610
$\varepsilon_{0.5}$ (0)	880	770	960	1000	1030	930	780	750	1950
$\Delta\varepsilon_{0.5}$ (67)	470	290	200	170	250	70	120	50	840
T_C [K]	250	294†	275	275	275	250	275	225	–
f [10^6 cm^{-2}]	2.36								2.34
Γ [cm^{-1}]	55-65	57-81	43-55	60-90	48	62-85	63-84	92	5.2
γ [cm^{-1}]	6-23	7-30	10-17	6-15	10	7-23	17-20	10	–
δ [cm^{-1}]	32	33	28	32	35	33	32	34	–
β[10^9JC^{-4}m^5]	8.6	18	19	11	14	5.2	8.2	9	0.8

Table 4.1: Summary of the evaluated characteristics of the thin film structures. The total thickness of STO layers is denoted by d_{STO}. The soft-mode frequency ω_0 and the permittivities ε_0 and $\varepsilon_{0.5}$ for 0 kV/cm and their change upon 67 kV/cm ($\Delta\omega_0$, $\Delta\varepsilon_0$, $\Delta\varepsilon_{0.5}$) were taken at T_C for most samples. The static permittivity value ε_0 and its value at 0.5 THz, $\varepsilon_{0.5}$, were evaluated using parameters obtained from the fits. * Despite the overall STO thickness is 400 nm in this structure, only a 200-nm-thick STO layer was influenced by the bias electric field. † The probable value of T_C for the 2×50 sample is in the range 294−310 K (determined by extrapolation only). * The data are taken from [215] and they are available only for 294 K (not T_C). T_C for the 20×10 sample occurs near 225 K [223]. $^\diamond$ The data obtained for the STO single crystal at 90 K (not T_C).

(large value of Γ) and due to the small thickness of the STO/DSO structures (within their thickness an almost constant component of the bias field is expected along x axis in the notion of Fig. 3.5a). The thin film structures with a higher number (≥ 6) of individual STO layers exhibit slightly larger values of the soft mode damping and of its variation with temperature (see Table 4.1).

The relaxation frequency was found to be dependent on temperature in the second step of fitting. Its values also slightly varied from sample to sample. The obtained ranges of relaxation frequency for each sample are presented in the Table 4.1. At higher temperatures (> 180 K) the form of the experimental THz spectra was mainly given by the soft-mode contribution to the permittivity and only the lower-frequency part of the spectra was influenced by the relaxation contribution. However, at low temperatures (≤ 120 K) the form of the spectra was completely governed by the relaxation because the soft-mode frequency was above the accessible spectral range and its contribution to the spectra virtually consisted of a quasi-constant background (for example see Fig. 4.3). Generally, the relaxation mode shows a gradual increase of its frequency on cooling within the range shown in Table 4.1. Small deviations of the best fit from the experimental dielectric spectra observed in some cases at low temperatures suggest that in reality there might be several relaxation processes with a distribution of their frequencies in the STO strained films.

The relaxation strength acquired nonzero values only in the ferroelectric phase of the STO films, as was mentioned above (see the inset in Fig. 4.7a). We point out an interesting fact that for 2×50, 3×50, 4×50×2 samples g attains maximum values of $\sim$300 at low temperatures, whereas the other samples acquire substantially higher values. These larger values may be again connected with a possible gradient of the strain in these structures. We can conclude that at lower temperatures the relaxation modes are much stronger in 1×100, 6×50 and 8×50 (i.e. more relaxed) samples than in the others; and, as a result, the low-frequency permittivity maintained high values even at the lowest temperatures due to the relaxation contribution to the THz permittivity.

The coupling constant showed similar values ($\delta \approx 32$ cm^{-1}) for all samples; they are summarized in the Table 4.1. This means that the oscillator-relaxator coupling is universal near the ferroelectric phase transition and below, and it does not depend on the magnitude of the strain.

In order to analyze the dielectric tunability of the samples we compared the static permittivity values ε_0 obtained at 0 kV/cm and at 67 kV/cm bias. These values were calculated by extrapolation of the model with the fitted parameters to the zero frequency. We emphasize that these values should be understood as THz data extrapolations and they have a good meaning only for our comparison. They should not be considered as an approximation of "true" static values because other low-frequency excitations, which may significantly contribute to the permittivity (for example a contribution due to the domain walls), are also expected to appear. This fact will be illustrated later on in this work when the stoichiometry effect of strained STO films will be studied (page 96). The extrapolated static permittivity values ε_0 are shown in the Table 4.1 together with the permittivity values $\varepsilon_{0.5}$ obtained by the fits at 0.5 THz under the same applied electric fields. First, from a comparison of ε_0 and $\varepsilon_{0.5}$ values it is seen that the relaxation-mode contribution to the permittivity is substantial. Second, the tunability strongly correlates with the soft-mode frequency: a lower soft-mode frequency implies a stronger field-induced change in the permittivity. This trend manifests both in the behavior of the extrapolated static permittivity and of the pemittivity found at 0.5 THz regardless of the contribution given by the relaxation mode.

To interpret the electric field-induced soft-mode behavior, we considered the Helmholtz free energy expansion (3.2). In the case of the thin films, where the probing THz electric field is parallel to the applied bias, the expression reduces to its simplest form which reads:

$$F = \frac{\alpha}{2}P^2 + \frac{\beta}{4}P^4, \tag{4.3}$$

where β is the coefficient that characterizes the anharmonicity of the soft-mode potential minimum; and the coefficient α has the same form as for single crystals [cf. (3.4)]

$$\alpha = \frac{\omega_r^2}{f_{osc}\varepsilon_{vac}}, \tag{4.4}$$

where ε_{vac} is the vacuum permittivity and ω_r is the soft-mode frequency which is renormalized due to nonvanishing spontaneous polarization P_s in the ferroelectric phase. We denote by $\omega_0(T,E)$ the value of the soft-mode eigenfrequency at a given temperature and electric bias field; the renormalized soft-mode frequency is then simply the soft-mode frequency at zero-bias field, i.e. $\omega_0(T,0) = \omega_r(T)$.

In the ferroelectric phase of the investigated structure under an applied bias E, we expect three polarization components: the spontaneous polarization P_s, a field-induced polarization $\Delta P(E)$, and a weak dynamic polarization P_{THz} oscillating at THz frequencies (the response to the probing pulse). It should be noted that thanks to the interdigitated electrodes deposited on the samples, we applied relatively high electric fields which may pole the STO film and induce regions with a nonvanishing macroscopic spontaneous polarization. Taking this into account we can write the total in-plane polarization as

$$P = P_s + \Delta P(E) + P_{THz}. \tag{4.5}$$

The harmonic part of the free energy F, oscillating at THz frequencies, then can be written as

$$F_{THz} = \frac{\omega_r^2}{2f_{osc}\varepsilon_{vac}}P_{THz}^2 + \frac{3}{2}\beta\left[P_s + \Delta P(E)\right]^2 P_{THz}^2. \tag{4.6}$$

In the weak field limit the soft-mode hardening due to the bias electric field together with its renormalization by the spontaneous polarization is then expressed in the following way:

$$\omega_0(T,E) = \omega_0(T,0)\sqrt{1 + 3\beta\left[\varepsilon_{vac}f_{osc}/\omega_0^2(T,0)\right]^3 E^2 + 6\beta\left[\varepsilon_{vac}f_{osc}/\omega_0^2(T,0)\right]^2 P_sE}. \tag{4.7}$$

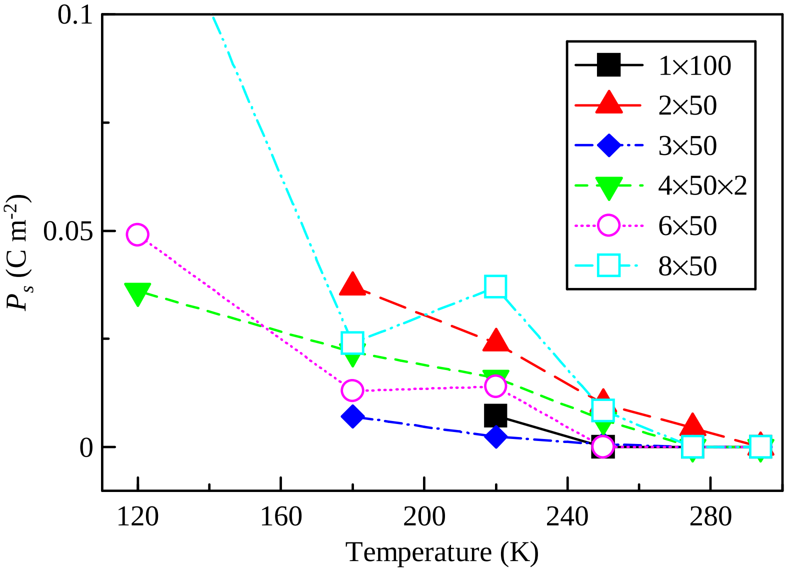

Figure 4.9: Estimated temperature dependence of the spontaneous polarization. Symbols are values obtained by the fits. Lines are guides to the eye.

Our interdigitated electrode structure implies that the adjacent gaps between the electrode fingers are poled with the opposite field, i.e., the sign of P_s alternates in the adjacent gaps. However, the sign of P_s and E [or $\Delta P(E)$] is always the same regardless the orientation of the field. Hence, the mixed term $P_s \cdot E$ in (4.7) is positive in each probed part of the sample and contributes to the electric-field-induced soft-mode hardening.

In the paraelectric phase or in an unpoled sample the last term under the square root in (4.7) is absent, while it may significantly contribute to the soft-mode tunability at low temperatures. Each experimentally obtained soft-mode electric-field dependence in the ferroelectric phase was fit by this expression. Resulting fits for 4×50×2 sample are presented along with the experimental data in Fig. 4.8. These fits describe well two basic features observed in the figure: (1) the SM tunability does not substantially decrease with decreasing temperature below the phase transition as it would be expected from the SM hardening $\omega_0(T)$; (2) for low temperatures the variation of $\omega_0(T, E)$ with field tends to be linear even for low fields. Both these phenomena are explained by a non-vanishing spontaneous polarization P_s in the ferroelectric phase.

At temperatures of the phase transitions or higher, i.e., where $P_s = 0$, the only fitting parameter in the equation (4.7) is the anharmonic coefficient β. The fitted values of β are presented in Table 4.1. In the weak field limit ($E < 35$ kV/cm), the soft mode displays a quadratic growth with the external bias (Fig. 4.8).

At temperatures below the phase transition, we assumed that β is temperature independent. We used the values found by fitting in the paraelectric phase (shown in Table 4.1) for fitting the SM behavior in the ferroelectric phase. The spontaneous polarization P_s was again the only fitting parameter in the model. An increase of its value was observed on cooling. The temperature dependence of the spontaneous polarization is shown in Fig. 4.9 for the investigated samples. These values should be considered with caution because possible contribution of higher-order terms in (4.3) and (4.7) cannot be excluded within the accuracy of our experimental data and, in reality, the anharmonic coefficient β can exhibit a weak temperature dependence like it was found for STO single crystals.

Thin films of STO grown on YBCO substrates studied by Fuchs et al. [224] were found to be in the ferroelectric phase below 90 K and to possess the spontaneous polarization of $P_s \approx 0.3$ C/cm^2 at helium temperatures. The saturated spontaneous polarization of $P_s \approx 0.28$ C/cm^2 found in the ferroelectric phase of BaTiO$_3$ single crystals [225] is also comparable to the previous one. We, therefore, think that values stemming from our data (see Fig. 4.9) are quite reasonable.

Repeatability of results in multilayer structures

Since even small changes in the preparation process of epitaxial thin film structures can lead to a dramatic variation in their dielectric properties we decided to compare the THz response of similar samples. Additional thin film structure denoted 4×50 B was prepared. It had the same layer sequence as 4×50 A sample, and, correspondingly, should posses the same dielectric properties. However, only temperature dependent dielectric properties without electric field were probed in this sample as it was destroyed during the deposition of the metallic electrodes. Thus we disposed of 3 samples with nominally the same

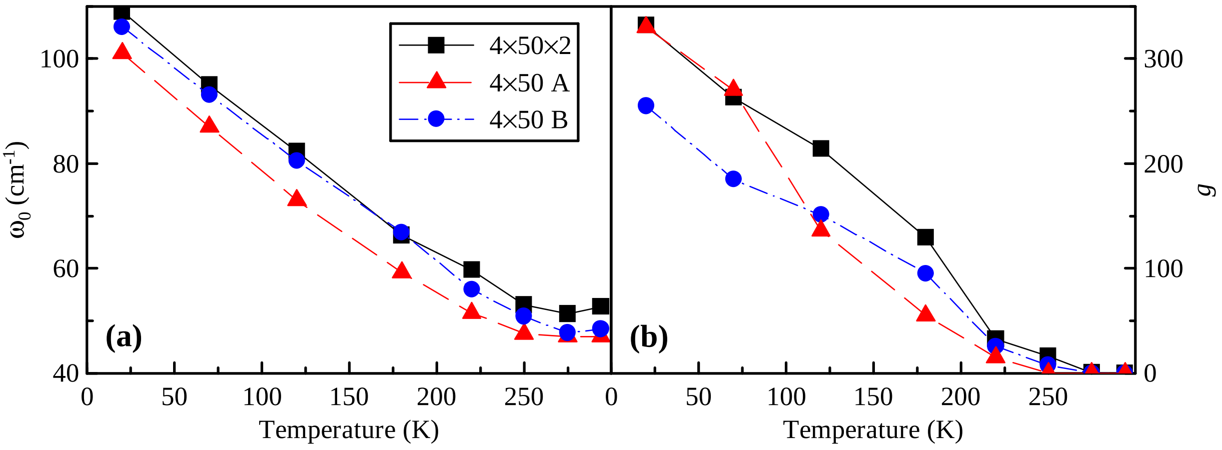

Figure 4.10: Soft-mode frequency **(a)** and relaxation strength **(b)** temperature behavior for three different thin film structures with the same structural parameters. Symbols are values provided by the fits. Lines are guides to the eye.

properties: 4×50 A, 4×50 B and 4×50×2. A comparison of the temperature behavior of the soft-mode and of the relaxation strength for these samples is shown in Fig. 4.10. One can observe that the temperature dependences of these two parameters have very similar characters for the three samples. In the case of the soft-mode frequency temperature dependence, samples 4×50×2 and 4×50 B show very similar values, while the 4×50 A sample displays slightly lower values. This small difference can be caused, for example, by a better composition stoichiometry of STO film in this sample compared to that in the others (role of stoichiometry will be discussed below in details). Nevertheless, all these thin film structures exhibit the same phase transition temperature of 275 K. The anharmonic parameter of the soft-mode potential for the 4×50×2 sample at room temperature was estimated to attain a value of 12×10^9 J C^{-4} m^5, while the value of 14×10^9 J C^{-4} m^5 was found for 4×50 A sample.

Taking into account the accuracy of our experimental data and numerous technological difficulties in the sample preparation process we can state that a nearly perfect agreement between the estimated parameters was observed. Hence, an excellent repeatability in the preparation of strained nm-thick-film structures was achieved despite technological challenges.

Dynamic tunability

We also carried out experiments aiming to characterize the dynamic tunability of the dielectric properties of the multilayered structures. The 4×50 A sample was used in these experiments where a train of rectangular pulses of positive electric field was applied as a bias. The frequency of the bias was tuned from units of Hz up to 100 kHz. The measured THz signals constituted a difference between THz wave forms with the bias field off and on. Then, the THz wave forms of the biased sample were calculated using the measured wave form with the unbiased sample. The power transmission spectra of the biased sample normalized to the spectra measured without bias are shown in Fig. 4.11.

The maximum tunability is achieved at 0.75 THz. Under the dc electric-field bias of 67 kV/cm the power tunability reaches 60 %, while weaker ones (43−50 %) are observed at higher driving frequencies. This decrease of the dynamic tunability is most probably related to a hysteresis effect observed in the thin film structures [216]. We observed that immediately after switching off the applied electric field of a high value ($>$ 35 kV/cm) the permittivity does not acquire the equilibrium value. This value is reached only after some time or after an application of the reversed field bias. In terms of the soft mode it means that its frequency does not soften to its equilibrium value immediately at switching off the bias. Therefore, the amplitude of the dynamic tuning slightly decreases compared to the static effect.

The variation of the tunability at various frequencies of the applied bias may originate from electrical characteristics of the devices used in the experiments. Since we were dealing with the ac bias of a relatively high voltage, at some frequencies there could appear

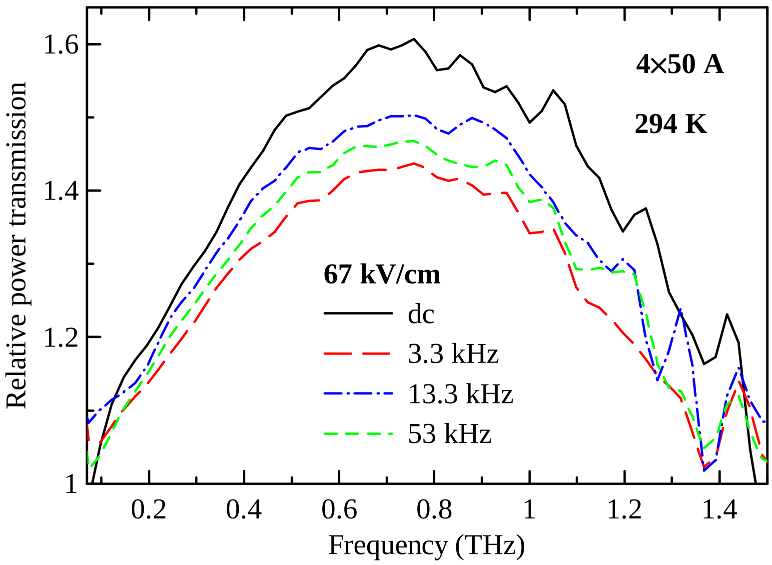

Figure 4.11: Ratio of the power transmittances with and without bias measured with 4×50 A sample at room temperature and with a train of rectangular pulses of positive electric field as a bias at several frequencies.

electrical resonances in the experimental circuit providing the bias, which can lead to an attenuation of the bias applied to the sample despite the fact that a voltage supply displayed a specified voltage value.

The high-frequency limit of the ac bias field for the thin film samples is determined by the electrode structure and the electrical characteristics of experimental devices. Namely, it originates from the reactance of the sample, and, correspondingly, from the ability of the devices to deal with this reactance. The electrode structure possesses a non-negligible capacitance. To apply the specified voltage to the electrodes the device should deliver a corresponding electric charge. At some frequency f_{max}, however, the necessary electric charge cannot be accumulated in the electrode structures even during the time $1/(2f_{max})$. For example, in the case of a 50-µm-thick STO single crystal with tin oxide electrodes on both surfaces we observed a characteristic time of several seconds, and there was no way to carry out such experiments with an alternative driving field.

4.1.4 Summary

The THz dielectric properties and the electric-field tunability of several STO/DSO thin film structures have been characterized using the time-domain THz spectroscopy. The dielectric spectra were obtained in a broad temperature range (20−294 K) which allowed us to estimate the paraelectric-to-ferroelectric phase transition temperatures for all the investigated structures. A general model for the THz permittivity is shown to well describe all the measured spectra at different temperatures and applied electric fields. The model includes a damped harmonic oscillator (the soft mode) coupled with a Debye relaxation (the central mode). The relaxation strength (or the effective charge) is found to acquire nonzero values only in the ferroelectric phase of the STO layers while it attains zero values in the paraelectric phase. Nevertheless, the central mode is still observable in the spectra owing to its coupling to the strongly polar soft mode. The effective charges of the soft and relaxation mode are shown to be of the opposite signs.

The variation of the soft-mode frequency with temperature and electric field $\omega_0(T, E)$ was demonstrated to be responsible for the general behavior of the THz dielectric spectra. At higher temperatures the central mode gives an improvement of the form to the lower-frequency part of the spectra, whereas it fully determines the spectral shape at temperatures below 120 K.

We described the electric-field-induced permittivity changes by the soft-mode frequency hardening using the anharmonic soft-mode potential in terms of the Landau-Devonshire theory. The anharmonic coefficient β is evaluated for all the investigated structures. Surprisingly, the electric-field tunability does not substantially decrease with cooling below the phase transition temperature. This is explained by a high value of the spontaneous polarization, which renormalizes the effective soft-mode potential.

The differences in the dielectric spectra and in the temperature and electric-field behavior of the estimated parameters among the investigated structures are explained in terms of the possible gradual relaxation of the strain with increasing distance from the substrate (total STO thickness). The strain gradient provides two reasons for the observed phenomena. First, slightly different dielectric properties of each separate layer within the thin film structure are expected due to differently strained lattice of each layer. Second, as it was shown in [212] the strain is relaxing through the dislocation defects which may significantly affect the dielectric properties. We assume that these defects are mainly responsible for an intense manifestation of the relaxation mode in the spectra of the structures with a large number (≥ 6) of STO/DSO bilayers and in the 100-nm-thick STO layer.

Taking into account all the experimental data and their complete analysis we can state that the most optimal structure for the tunable application is the one possessing four STO/DSO bilayers. It has the total STO thickness of 200 nm and demonstrates comparatively high tunability which is still not deteriorated by a strong contribution to the permittivity of the relaxation mode. In addition, a functional structure can be prepared with the thin film structure on both sides like the 4×50×2 sample.

4.2 Impact of composition stoichiometry on the dielectric properties of $SrTiO_3$ films

In this section we present the study of the dielectric properties and soft-mode behavior of strained epitaxial STO films with different stoichiometric composition grown on DSO substrates [226]. This part of the work was done in a tight collaboration with colleagues from several institutions in the United States. A great number of experimental techniques was involved in order to compare properties of the nominally stoichiometric and non-stoichiometric films. My part of the work consisted in the measurements and interpretation of the THz data.

The dielectric constant and loss of biaxially strained STO thin films were previously found to be dependent on frequency in a way like if they were relaxor ferroelectrics [227,228]. It was then proposed that all STO films were indeed relaxor ferroelectrics [229]. In that paper the relaxor behavior was attributed to pre-existing polar nanoregions originating from unintentional deviations of STO stoichiometry in nominally stoichiometric samples.

4.2.1 Samples

Several thin films of $Sr_{1+x}TiO_3$ ($-0.05 < x < 0.05$) with the thickness of 50 nm were grown on well-oriented ($\pm 0.1°$) (110) DSO substrates by codeposition from Sr, Ti, and O_2+~10 % O_3 molecular beams in a Veeco GEN10 oxide MBE system. The oxidant background pressure (O_2+~10 % O_3) was maintained at 5×10^{-7} Torr during and after the deposition until the sample cooled below 200 °C in order to minimize oxygen vacancies. During growth the substrate temperature was held at 700 °C. Other technological details including a way of the precise control of the composition stoichiometry can be found in reference [226].

The film crystalline structure, including out-of-plane and in-plane lattice constants and crystallinity, was examined by x-ray diffraction (XRD) using Cu $K\alpha_1$ radiation on a high-resolution Philips X′Pert MRD diffractometer. The out-of-plane lattice constants of the $Sr_{1+x}TiO_3$ ($-0.05 < x < 0.05$) films are plotted as a function of strontium content in Fig. 4.12. The values were calculated from the $00l$ film peak positions in the $\theta - 2\theta$ scans. The nominally stoichiometric sample shows the smallest out-of-plane lattice parameter of 3.8802 ± 0.0003 Å. For non-stoichiometric films this value increases both for the strontium and for titanium rich films. This phenomenon is in agreement with the previous study of homoepitaxial STO films grown by MBE [230] and illustrates that the out-of-plane lattice constant can be used to establish whether the STO films are stoichiomteric with the precision of about ±1 %. The slightly larger out-of-plane constant (3.8833 ± 0.0005 Å) of STO/DSO found by Biegalski et al. [227] suggests that in that work the reported relaxor behavior could originate from a small (~3 %) off-stoichiometry in the studied

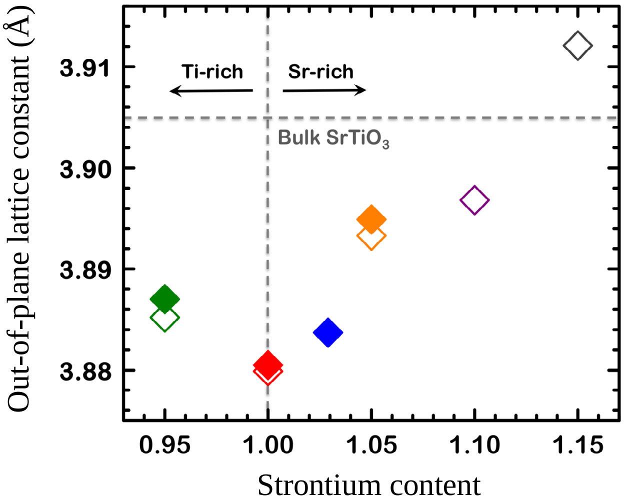

Figure 4.12: Out-of-plane lattice constant as a function of strontium content in $Sr_{1+x}TiO_3$ ($-0.05 < x < 0.15$) films grown on (110) DSO substrates. Dashed lines indicate the lattice spacing and stoichiometry of bulk STO. The error bar of the lattice constants is about the size of the symbols. The dielectric measurements are performed on selected samples whose Sr content is shown by the solid symbols. After [226].

films. Minor deviations from the nominal stoichiometry could be as well at the origin of the observed variation in the out-of-plane lattice spacing of similar STO/DSO structures in reference [231]; the relaxor behavior was also reported for these structures.

The composition of the films shown in Fig. 4.12 by solid symbols was verified using Rutherford backscattering spectrometry (RBS). The results confirmed that all the films had the expected composition stoichiometry within the experimental error.

4.2.2 Dielectric measurements and discussion

The dielectric properties of selected samples were measured in the radio-frequency (RF) range using an Agilent E4980A LCR meter with a Lake Shore 332 temperature controller. For these measurements Cr/Au interdigitated electrode structures were deposited on top of the films. The dielectric permittivity and loss tangent (tan δ) measured over the temperature range $10 - 350$ K from 1 kHz to 1 MHz are shown in Fig. 4.13.

The presence of frequency dispersion in the vicinity of the ε'_{max} is a common signature of relaxor ferroelectrics. The relaxor behavior of mixed ABO_3 perovskite oxides like $Pb(Mg_{1/3}Nb_{2/3})O_3$ and La-doped $PbZr_{1-x}Ti_xO_3$ is believed to be caused by compositional disorder and related random electric fields [175]. Adding impurities into ferroelectrics and/or into incipient ferroelectrics can also induce relaxor behavior. Point defects like impurity-oxygen vacancy clusters and anti-site defects can lead to the formation of dipo-

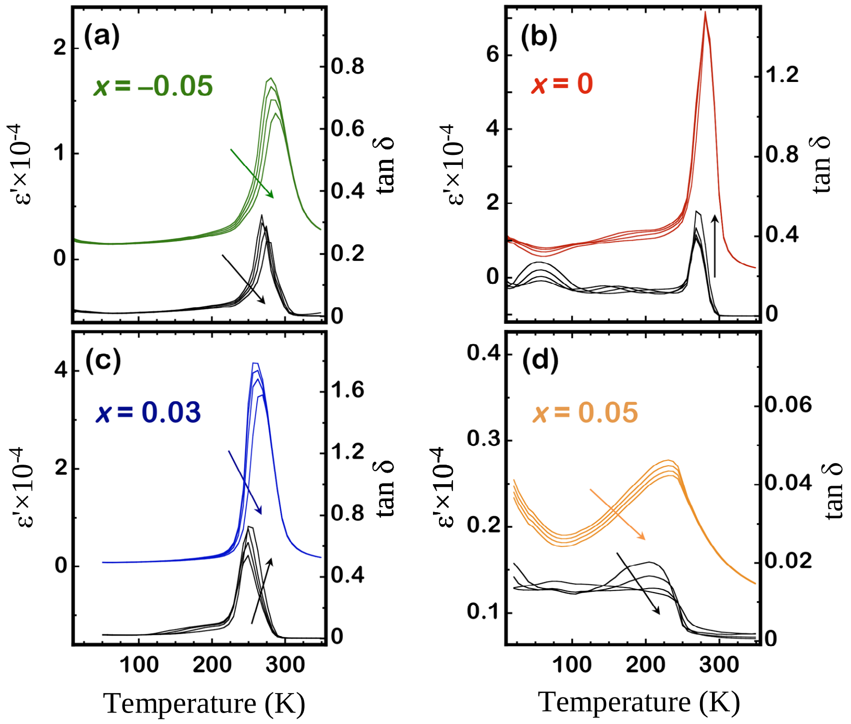

Figure 4.13: In-plane dielectric constant (color curves) and tan δ (black curves) as a function of temperature measured on $Sr_{1+x}TiO_3$ films with: **(a)** $x = -0.05$, **(b)** $x = 0$, **(c)** $x = 0.03$, and **(d)** $x = 0.05$. Arrows indicate the direction of shift of the measured data with increasing measurement frequency in the sequence 1, 10, 100, and 1000 kHz. After [226].

lar inclusions which polarize a small volume around them and form polar nanoregions [175]. Decreasing the point defect concentration, for example for STO thin films by achieving a precise stoichiometric composition, can significantly reduce the number of the polar nanoregions. This improvement then can be observed in reduction of the permittivity dispersion at low frequencies (see Fig. 4.13b).

The nominally stoichiometric ($x = 0$) sample demonstrates the dielectric constant peak value of ~70000 at 280 K, which is much higher than those of the off-stoichiometric samples. The samples with $x = -0.05$ and $x = 0.03$ exhibit the permittivity maximum at temperatures ~280 K and ~265 K, respectively. Their phase transition temperatures, as given by the maximum permittivity value, are frequency dependent, whereas the nominally stoichiometric sample does not show any frequency dispersion. The paraelectric-to-ferroelectric transition temperature (T_C) of the film with $x = 0$ is in agreement with the predicted transition temperature from thermodynamic analysis [232] and it also agrees with the PT temperatures we determined for $n{\times}50$ films in the previous section.

The structural disorder caused by Ruddlesden-Popper defects (i.e., insertions of extra SrO monolayers at random positions along $\{100\}$ STO planes that shift and terminate continuous Ti-O-Ti chains between TiO_6 octahedra [233]) could be responsible for the lowest observed ε'_{max} and $T(\varepsilon'_{max})$. The structural relaxation in Sr-rich samples is also a reason for the lower temperature $T(\varepsilon'_{max})$ of the permittivity maximum value.

The measured spectra of tan δ demonstrate different behavior in the films with $x = -0.05$ and $x = 0.05$ (Figs. 4.13a,d) from that of the films with $x = 0$ and $x = 0.03$ (Figs. 4.13b,c). For more stoichiometric films the maximum in the loss tangent increases with increasing the measurement frequency. This is typical for a broad relaxation, which either slows down or broadens towards lower frequencies with decreasing temperature [234]. The opposite tendency is observed for samples with a higher concentration of point defects ($x = 0.05$ and $x = -0.05$). This behavior may be explained by the presence of a second very low-frequency relaxation peak slowing down over the measurement frequency range during cooling.

Since the ferroelectric soft mode is at the origin of the phase transition in STO, it was expected to exhibit a different behavior in each of the investigated thin films. To characterize the soft-mode behavior we investigated the films with $x = 0$ and $x = 0.03$ by the THz time-domain spectroscopy. The in-plane complex dielectric response of the thin films in the THz range was calculated from the complex transmittance spectra measured in a cryostat and in a furnace.

The measured complex permittivity spectra of the nominally stoichiometric sample at several temperatures are shown in Fig. 4.14 by symbols. The dominant feature in the spectra is due to the contribution to the permittivity given by the ferroelectric soft mode. Its marked temperature variation is directly seen from the measured spectra especially for the nominally stoichiometric film. In addition, a contribution to the spectra of the relaxation mode (central mode) is noticeable near the low-frequency limit of the available data. Altogether, these features in the spectra suggested that investigated films displayed the same behavior as that of the thin film heterostructures described in the previous section. Therefore, the experimental complex permittivity spectra were fitted using the same model (4.2) involving a damped harmonic oscillator representing the soft mode coupled to a Debye relaxation representing the central mode. All the fitting parameters of thin films with $x = 0$ and $x = 0.03$ were found to acquire very close values to those previously found for different thin film structures. Again the soft-mode frequency $\omega_0(T)$ was found to be the key parameter which describes the temperature evolution of the dielectric spectra.

The complete temperature behavior of the soft-mode frequency in sample with $x = 0$ and $x = 0.03$ obtained as a fitting parameter is presented in the inset of Fig. 4.14. The soft-mode frequency of the nominally stoichiometric films softens (decreases) to much lower values ($\sim$23 cm^{-1}) than that for the non-stoichiometric film ($\sim$46 cm^{-1}). Therefore, the soft-mode contribution to the permittivity is expected to be the largest in the stoichiometric sample. In fact, this correlates well with the RF results obtained on the same samples (see Figs. 4.13b,c). According to the temperature dependence of the soft-mode frequency

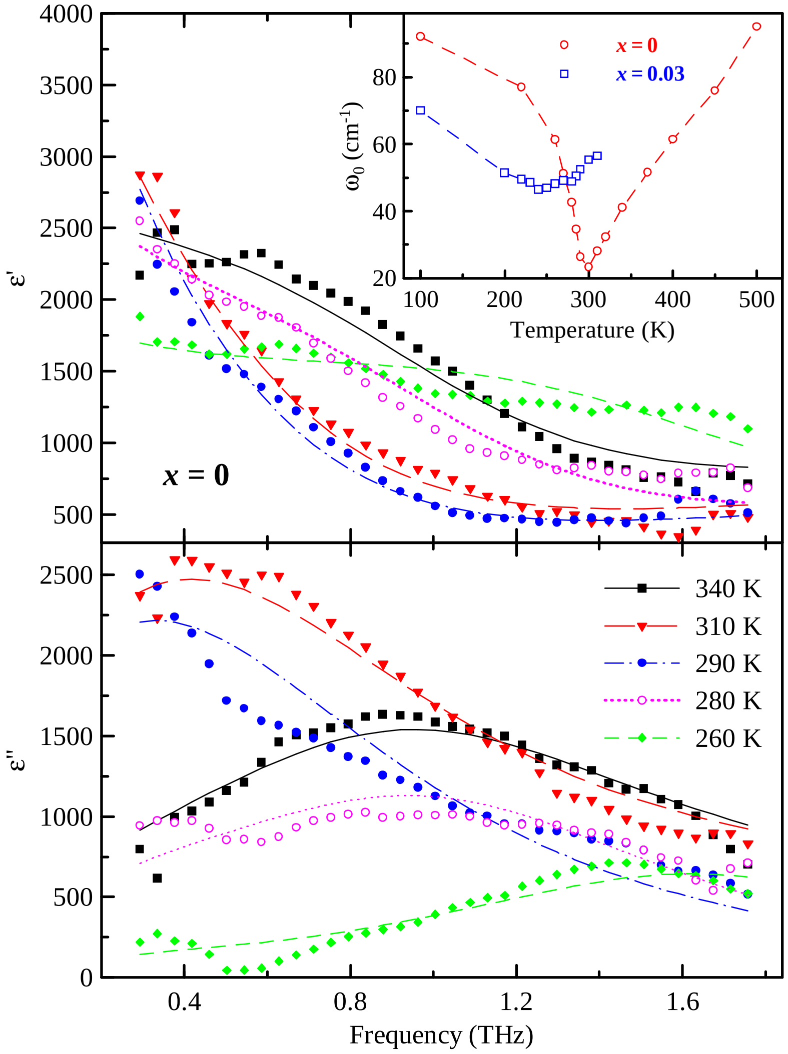

Figure 4.14: Complex permittivity spectra of the nominally stoichiometric $Sr_{1+x}TiO_3/DyScO_3$ film ($x = 0$) at several temperatures. Symbols represent measured data; lines are fits by the model (4.2). Inset: the soft-mode frequency behavior with temperature for films with $x = 0$ and $x = 0.03$. The data points are obtained as fit parameters; lines are guides to the eye.

the ferroelectric phase transition occurs at temperatures between 290 and 300 K in the film with $x = 0$ and between 230 and 260 K in the film with $x = 0.03$, which is again in agreement with the RF data. In addition, the soft mode is slightly broader (larger damping) $\Gamma = 56$ cm^{-1} in the non-stoichiometric sample than that in the stoichiometric one $\Gamma = 52$ cm^{-1}. It may be caused by defects coming from the off-stoichiometric composition of the film. The coupling constant δ and the relaxation frequency γ in the film with $x = 0$ acquired values of $\sim$12 cm^{-1} and $\sim$10 cm^{-1}, respectively.

In order to exclude an impact of impurities diffusion from the underlying DSO substrate into the film on its dielectric properties the $x = 0$ and $x = 0.03$ samples were examined by secondary ion mass spectrometry. The results showed comparable amounts of dysprosium (Dy) and scandium (Sc) diffused into the films, which means that diffusion defects should have comparable effects in these films. Therefore, the origin of the significant differences in the RF and THz dielectric properties can be mainly attributed to the different Sr:Ti stoichiometry of these films.

Taking into account the soft-mode temperature behavior in the nominally stoichiometric and non-stoichiometric samples we can conclude that the stoichiometric film exhibits classical features of a displacive ferroelectric. Whereas small deviations from the stoichiometric formula are shown to result in a stiffened soft-mode frequency and its weaker temperature dependence. It is an interesting fact that such parameter like the soft-mode frequency characterizing the lattice dynamic can provide us with a quite precise measure of the microscopic quality of the thin films. Nevertheless, the soft-mode contribution to the permittivity cannot completely account for the temperature dependence of the low-frequency (RF) dielectric constant. For example, the extrapolated static permittivity value for the stoichiometric film ($x = 0$) calculated using the fitting model at the phase transition temperature is about 7000, which is one order of magnitude smaller than the maximum permittivity ε'_{max} value measured in the kHz−MHz frequency range. The fact that the central-mode contribution to the permittivity always dominates near $T(\varepsilon'_{max})$ suggests that the phase transition is displacive with crossover to order-disorder type in the stoichiometric sample.

4.2.3 Summary

We have studied the impact of composition stoichiometry on the dielectric properties of the strained STO films. We found that the nominally stoichiometric film exhibits the smallest out-of-plane lattice constant, dispersion-free low frequency (RF) permittivity, and a deep reduction of the soft-mode frequency near the ferroelectric phase transition temperature. The soft-mode frequency in the stoichiometric thin film is found to be as low as that for single crystals at temperatures where the quantum fluctuations begin to play the role in suppressing the soft-mode further softening (below 70 K). It has not been previously reported any STO film with the ferroelectric mode slowing down to such low frequencies.

We believe that these properties are the intrinsic properties of STO thin films, and they should not show relaxor behavior as long as defect concentrations are reduced by precise composition control. Defects induced by a small deviation from the nominally stoichiometric composition should be responsible for the lack of repeatability in the dielectric behavior of different (but nominally the same) samples and for the inferior dielectric properties of thin films than those of bulk single crystals. This investigation confirmed an important and extremely sensitive coupling of the dielectric properties of complex oxide systems with defects caused by their non-stoichiometric composition. Precise composition control, therefore, should be the key point in order to obtain the intrinsic and desirable properties of STO in both bulk and thin film forms.

4.3 Ferroelectric phase transition in $KTaO_3$ film

This section is devoted to the investigation of a polycrystalline $KTaO_3$ (KTO) thin film deposited on a sapphire plate. This incipient ferroelectric compound exhibits the dielectric properties and their temperature behavior similar to those of STO. Despite the fact that the dielectric constant of KTO is slightly lower than that of STO, KTO has a larger value of the coefficient β [23] which characterizes the anharmonicity of the soft-mode potential [see (4.3)]. This implies a possibly stronger field-induced tunability of the dielectric properties of potassium tantalate. In addition, the loss tangent ($\tan\delta$) in microwave (MW) frequency range is shown to become significantly lower than that of STO at temperatures below 100 K [174]. These properties attract a high interest to KTO. Nevertheless, there is still a way to improve its room temperature properties by inducing the paraelectric-to-ferroelectric phase transition, e.g. by strain.

This work was done in a tight collaboration with colleagues from Jožef Stefan Institute in Ljubljana (Slovenia) who prepared the samples and provided their chemical and x-ray characterization [235]. We performed the dielectric measurements and showed that the ferroelectric phase transition occurs in these polycrystalline films.

4.3.1 Film preparation

The films were prepared by chemical solution deposition. Potassium acetate and tantalum ethoxide were dissolved in 2-methoxyethanol. The solution was deposited on (0001) sapphire substrates by spin-coating. Then, it was dried at 180 °C for 2 min on a hot plate, and annealed at 900 °C for 5 min. The deposition procedure was repeated 4 times to obtain the film thickness of 200 nm. The final annealing lasted 15 min at 900 °C. More technical details can be found in reference [235].

X-ray diffraction (XRD) analysis performed in a $\theta-2\theta$ geometry with a monochromatic Cu $K\alpha_1$ radiation source revealed perovskite KTO film with preferred (100) orientation (see Fig. 4.15). Surface morphology of the film was analyzed by field emission scanning microscopy (FE-SEM). The microstructure shown in the inset of Fig. 4.15 consists of grains with an average size of 160 nm as determined by lineal analysis.

In order to check the chemical composition of the film a quantitative chemical analysis was performed using plasma mass spectrometry. Besides the main components K and Ta, the presence of 53 mass ppm of Na and 13 mass ppm of Mg was revealed. Other impurities were below 5 mass ppm.

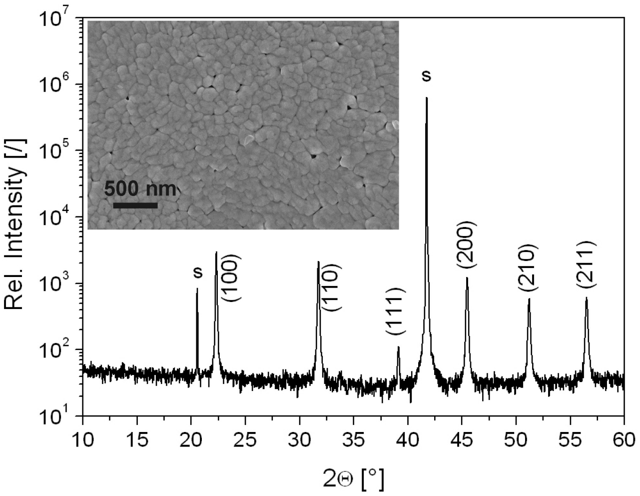

Figure 4.15: X-ray diffraction pattern of the KTO thin film deposited on (0001) sapphire. Peaks coming from the substrate are denoted as S. Inset: Plain-view FE-SEM micrograph of the film. After [235].

4.3.2 Spectroscopic results and discussion

The complex dielectric spectra in the THz range were calculated from the measured complex transmittances with a thin film on a substrate and with a bare substrate. An example of the calculated dielectric functions obtained at selected temperatures is shown in Figs. 4.16a,b. The general form of the spectra is governed by the soft mode, whose frequency variation is responsible for the observed changes in the spectra with cooling. A central-mode contribution to the permittivity is seen at lower temperatures. The relaxation frequency of the central mode is near the low-frequency edge of the accessible spectral range. The form of the spectra and their qualitative behavior seem to be similar to those of STO films and multilayers studied above. We used, therefore, the model of coupled oscillator and Debye relaxation (4.2) which was proven to describe THz permittivity spectra of a large variety of strained STO films.

Again, a common fit of all the measured spectra has been performed. The soft-mode frequency ω_0 and damping Γ were allowed to be temperature dependent in our fit. The oscillator strength f_{osc} and the coupling constant δ were assumed to be temperature independent, and they acquired values of about $f_{osc} \approx 1.3\times10^6$ cm^{-2}, $\delta \approx 27$ cm^{-1}. The bare relaxation mode was characterized by the temperature independent relaxation frequency ($\gamma \approx 6$ cm^{-1} from the fit) and by the relaxation strength g whose value was allowed to be temperature dependent. All the fitting parameters acquired very similar values to those obtained for STO thin film structures shown in Table 4.1.

The soft-mode frequency and the relaxation strength versus temperature as obtained by

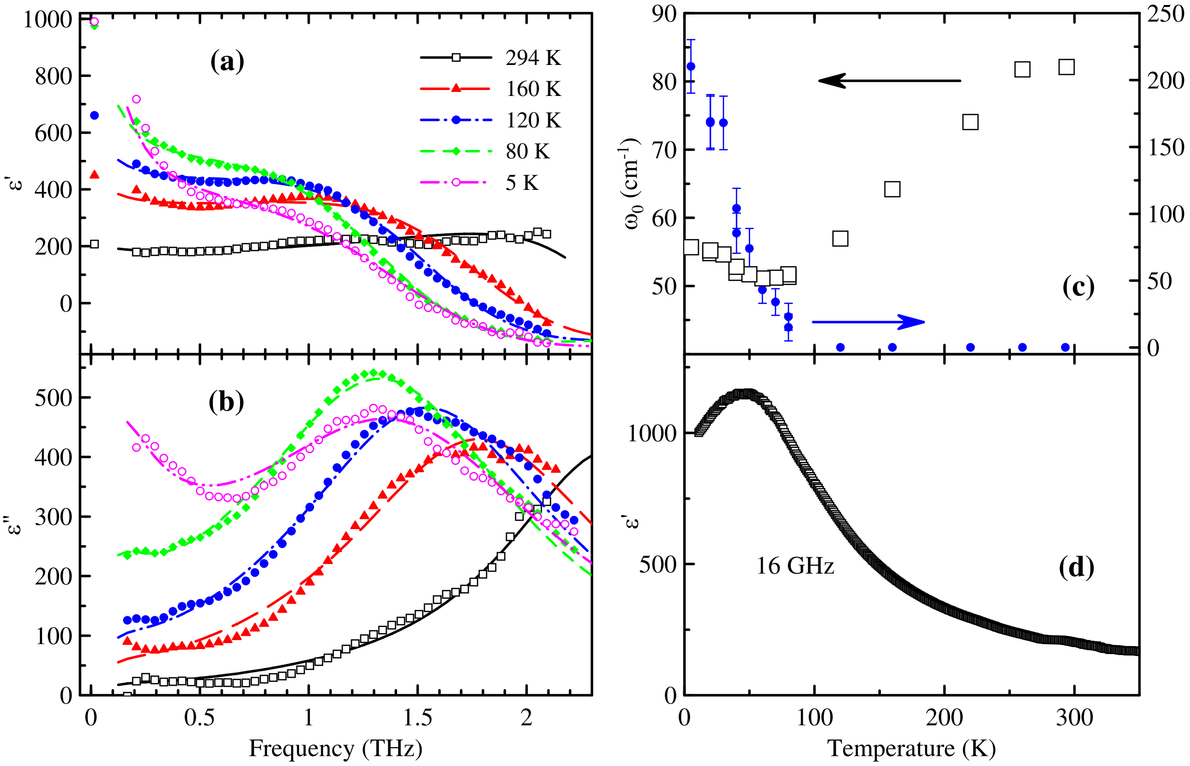

Figure 4.16: Real **(a)** and imaginary **(b)** part of the permittivity of KTO film at selected temperatures. Symbols are experimental data; lines are fits by (4.2). **(c)** Soft-mode frequency ω_0 and relaxation strength g as functions of temperature provided by the fits of THz spectra. **(d)** Temperature dependence of the dielectric constant measured at 16 GHz.

the fits are shown in Fig. 4.16c. The temperature dependence of the soft-mode frequency exhibits a minimum of 51 cm^{-1} near 60 K. Around this temperature the central mode also starts to couple to the polarization, which is expressed by the value of the relaxation strength g vanishing at higher temperatures and becoming non zero below ∼80 K. Similar picture has been observed at the ferroelectric phase transition in STO/DSO systems.

The THz spectra were complemented by dielectric measurements in the gigahertz (GHz) frequency range using a thin dielectric resonator method [236]. The microwave permittivity measured at 16 GHz is presented in Fig. 4.16d. Its temperature dependence shows a maximum in the range of 40–60 K. It can be fitted by the Curie-Weiss law (1.1) above 80 K. This fit yields the Curie-Weiss temperature $T_0 \approx 15$ K.

Since incipient ferroelectrics are structurally rather unstable, a weak mechanical strain or a small amount of chemical impurities may induce a ferroelectric order. In the case of the studied KTO film, quantitative chemical analysis showed insufficient amount of impurities for inducing the ferroelectricity. We, thus, suppose that the ferroelectric ordering originates from the strain.

The in-plane ferroelectric order in STO thin films can be induced by a weak tensile strain as shown in the previous sections of this work. Recently, occurrence of the ferroelectric phase transition was reported also in an epitaxial thin film of KTO on STO substrate [237]. In this case a large compressive strain (-2.1 %) led to a phase transition at 700 K. The thermal expansion coefficient of sapphire is larger than that of KTO. Therefore, cooling the sample after its annealing at 900 °C may lead to a compressive in-plane strain in the KTO film. By analogy with STO films, this strain would induce a paraelectric-to-ferroelectric phase transition with an out-of-plane spontaneous polarization.

Železný et al. investigated the ferroelectric soft mode in polycrystalline KTO film on Si and SiO_2 using the far infrared (IR) transmission spectroscopy [238]. The authors did not observed any phase transition but found a significant stiffening of the soft mode. Its frequency decreased only down to $\sim$55 cm^{-1} at 10 K which is close to the value we have found, whereas the soft mode softens down to 20 cm^{-1} in KTO single crystal [239]. Soft-mode stiffening was observed also in STO films by Ostapchuk et al. [240]. It was explained using an effective medium approximation by the presence of low-permittivity grain bondaries and possible nano-crack-type porosity which is at the origin of a substantially reduced permittivity.

4.3.3 Summary

Comprehensive characterization of the dielectric properties of a polycrystalline KTO film on (0001) sapphire substrate was done using time-domain THz spectroscopy and MW dielectric measurements. The THz spectroscopy allowed us to observe the soft mode and its coupling to a lower-frequency relaxation (CM). We observed a classical softening of the soft mode down to 60 K and its hardening with further cooling of the film. Such a minimum in the temperature dependence of the soft-mode frequency provides a strong evidence of the ferroelectric phase transition occurring near 60 K, which was confirmed by the dielectric measurement at 16 GHz.

It should be stressed that despite the completely different preparation technology and crystalline structure (epitaxial vs polycrystalline) of the thin films our model for the dielectric permittivity proposed for STO/DSO structures is able to describe THz spectra and their temperature evolution for the KTO film. This fact confirms that the THz dielectric response of thin films of both materials originates from similar excitations, namely the ferroelectric oscillation mode (SM) coupled to the relaxation mode (CM).

KTO thin films exhibiting an induced ferroelectric phase transition may attract a lot of interest mainly owing to the relatively simple preparation technique which does not require technological equipment for an epitaxial deposition of thin films. Although the dielectric properties of the polycrystalline KTO are inferior to those of strained STO films they may exhibit substantial electric-field tunability due to a stronger anharmonicity of the soft-mode potential.

4.4 Tuning of hard polar phonons in $SrTiO_3$ films

An observed electric-field-induced tunability of hard polar modes in strained STO films investigated by the far infrared (FIR) Fourier spectroscopy is reported in this section. The thin film structures of (i) series characterized by the time-domain THz spectroscopy in the first section of this chapter were used in this investigation. FIR measurements in a not completely standard arrangement carried out in the reflection geometry allowed us to perform a semi-quantitative analysis of hard-mode frequencies behavior upon an applied electric field. The quantitative results will be presented for the 100-nm-thick STO layer deposited on DSO substrate (the sample previously denoted by 1×100) since the other samples showed qualitatively the same behavior and no additional significant information can be extracted.

4.4.1 Experimental issues

In a usual Fourier transform infrared setup which is adjusted for reflectance measurements the input face of a sample is in contact with a metallic aperture defining the probed area of the sample. However, this was not possible in our case because of the presence of the conductive electrode structure on top of the thin films. Therefore, the probing infrared radiation illuminated not only part of the sample covered with electrodes (active area) but also other parts of the sample and a sample holder (inactive area). Schematic layout of the sample and probing beam is shown in Fig. 4.17. The probing infrared radiation was polarized in a way that its electric-field vector was perpendicular to the electrode fingers and parallel to [110] direction of DSO substrate. In this geometry the electrode structure was transparent for the FIR radiation and had a minor influence on the reflected signal.

Each measurement consisted of a reference spectrum $R_0(\omega)$ measured without an electric field and a reflectance spectrum $R_E(\omega)$ measured upon applied dc field E. The ratio $S(\omega)$ of these two spectra can be written as follows:

$$S = \frac{R_E}{R_0} = \frac{I_E + I_S}{I_0 + I_S}, \tag{4.8}$$

where I_E is the infrared power reflected from the active area of the sample with the bias field on, I_0 is the power reflected from the active area with the field off, and I_S is a signal reflected from the inactive area. The quantity S is indeed the raw experimental signal. An example of these raw reflectance curves measured at room temperature and under three different electric fields with sample 1×100 is shown in Fig. 4.18a. The pure field-induced

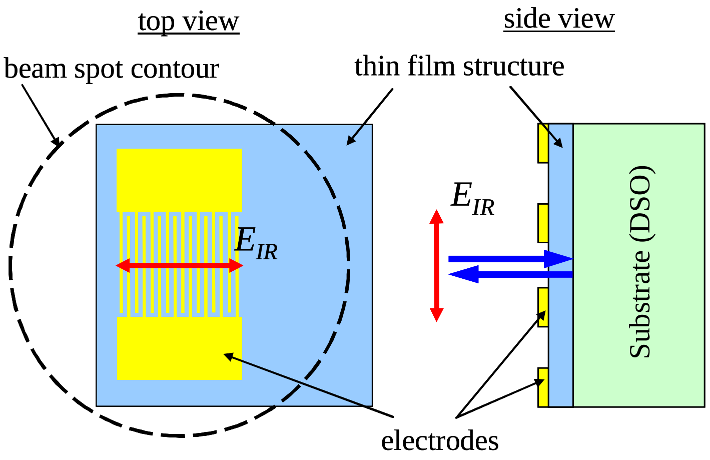

Figure 4.17: Schematic layout of the sample and of the probing infrared beam.

change in the FIR reflectance R_{FIR} then reads

$$R_{FIR} = \frac{I_E}{I_0} = (S-1)A + 1, \tag{4.9}$$

where the factor $A = 1+I_S/I_0$, and it describes the deviation due to a larger beam spot. We estimated this deviation from the low-frequency (below 100 cm^{-1}) behavior of the spectra. Initially, we assumed that the factor A is a frequency independent parameter. It seems to be a reasonable first-order approximation because the value of A is primarily related to the ratio of the surfaces of the active and inactive area. The complex dielectric spectra corresponding to the low-frequency part of the reflectance ratio spectra R_{FIR} are known from the THz time-domain experiments. The dielectric response in this frequency range is fully governed by the ferroelectric soft mode coupled with the central mode. Therefore, we could evaluate the expected field-induced change in the reflectivity spectrum R_{THz} in the frequency range 50−100 cm^{-1} using the THz data. The parameter A was then chosen in a way that the closest match between R_{FIR} and R_{THz} is found.

4.4.2 Results and discussion

In Fig. 4.18b we show an example of the normalized experimental spectra R_{FIR}. The substrate has centrosymmetric structure and does not show any electric-field tunability of the dielectric properties. Obviously, any value in the spectra which differs from unity is caused by electric-field-induced changes in the dielectric properties of the thin film. Tunable properties then modify the absorption of radiation in the film and the impedance mismatch at air/STO and STO/DSO interfaces. An interesting observation was made that some features of the reflectivity spectrum of DSO substrate (i.e., its phonon structure) may

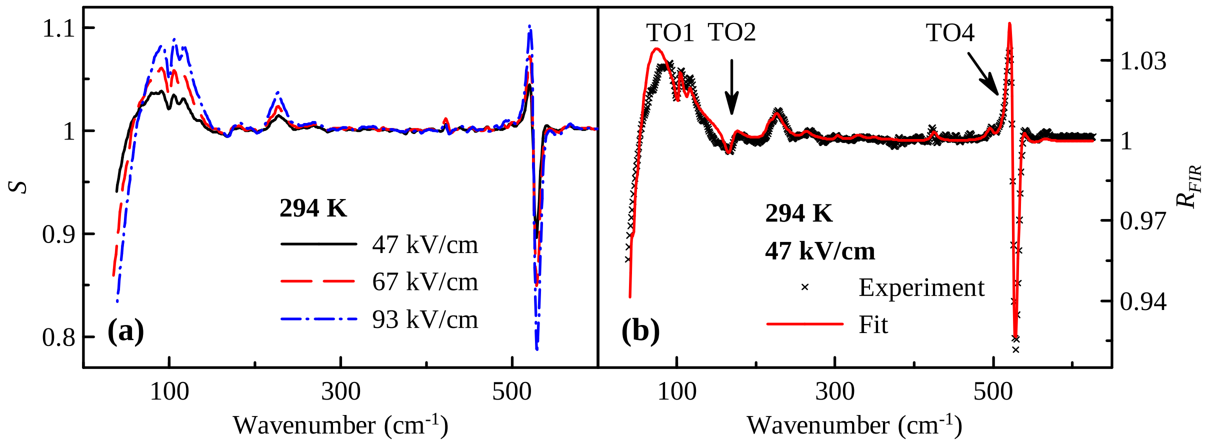

Figure 4.18: **(a)** Example of raw experimental signal S measured at room temperature under three different bias fields for 100-nm-thick STO layer. **(b)** Comparison of normalized experimental (symbols) reflectance ratio R_{FIR} with its fit (solid line) using the model (4.10); room temperature, 47 kV/cm bias, the same sample.

appear to some extent in the measured R_{FIR} spectra. This phenomenon originates from the field-induced change in the impedance mismatch at the STO/DSO interface. For example, the peak near 225 cm^{-1} (see Fig. 4.18) is coming from an overlap between the tails of tunable modes of STO and a strong phonon of DSO showing a reststrahlen band below 220 cm^{-1}.

Two prominent features are observed in the spectra (Fig. 4.18); they are related to the electric-field-induced frequency change of the ferroelectric soft mode (TO1) and of TO4 mode. There is a small signature of the TO2 mode tuning as well. In order to evaluate the tunability of the high frequency modes we tried to model the dielectric response of the thin film structures in a broad frequency range covering the experimental spectra. This model involves the expression (4.2) for the dielectric contribution of the soft mode coupled with the relaxation mode, which was previously introduced, and of two independent underdamped harmonic oscillators representing the hard modes

$$\varepsilon(\omega) = \frac{f_{osc}(1 - i\omega/\gamma) + g(\omega_0^2 - \omega^2 - i\omega\Gamma) + 2\delta\sqrt{f_{osc}g}}{(\omega_0^2 - \omega^2 - i\omega\Gamma)(1 - i\omega/\gamma) - \delta^2} + \sum_{j=2,4} \frac{f_{\mathrm{TO}j}}{\omega_{\mathrm{TO}j}^2 - \omega^2 - i\omega\Gamma_{\mathrm{TO}j}} + \varepsilon_\infty, \tag{4.10}$$

where $f_{\mathrm{TO}j}$, $\omega_{\mathrm{TO}j}$ and $\Gamma_{\mathrm{TO}j}$ are respectively the oscillator strength, eigenfrequency and damping of the hard modes. We calculated the expected reflectance of the structure using the transfer matrix formalism [203] where the STO permittivity was modeled by the expression (4.10) and the substrate dielectric properties were represented by the four parameters model (2.22). The parameters of the latter were found independently by fitting the reflectance spectra of the bare DSO.

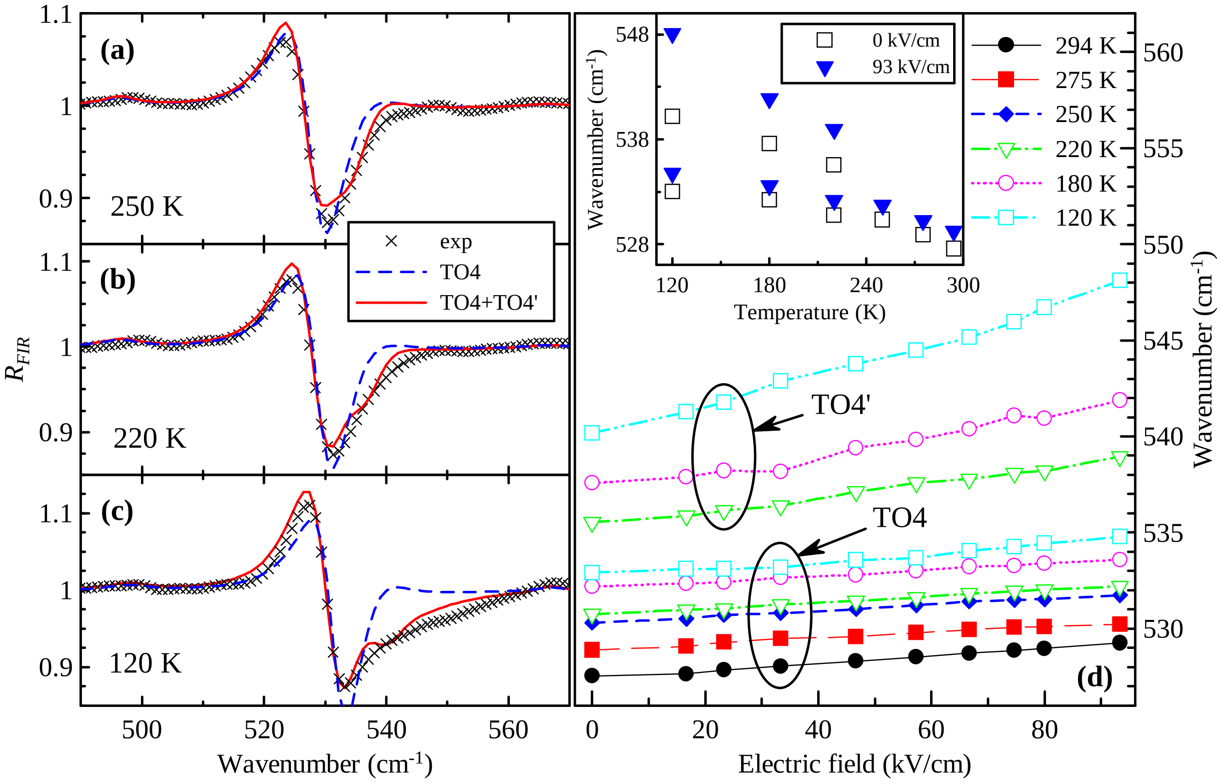

Figure 4.19: **(a)**, **(b)**, **(c)** Comparison of high-frequency parts of experimental (symbols) and fitted (lines) R_{FIR} curves for the bias field of 67 kV/cm. Fits shown by solid lines include TO4′ mode. **(d)** Tuning of the TO4 hard mode by the electric-field bias at different temperatures. Empty symbols denote split modes. Inset: temperature dependence of the hard modes frequency at zero and 93 kV/cm bias. Lines are guides to the eye.

Each normalized R_{FIR} spectra was fitted by the ratio of reflectances calculated for the bias field on and off. The parameters describing the permittivity of DSO were fixed during fitting. All the parameters describing the temperature and electric-field behavior of the coupled soft mode [parameters of the first term of (4.10)] were taken from the previous study of the thin film structures. Only the second term of (4.10) contains the fitted parameters. The oscillator strength $f_{\mathrm{TO}j}$ and the damping $\Gamma_{\mathrm{TO}j}$ were assumed to be temperature and field independent. The eigenfrequencies of TO2 and TO4 modes were assumed to depend both on temperature and electric field [i.e., $\omega_{\mathrm{TO2}}(T, E)$ and $\omega_{\mathrm{TO4}}(T, E)$]. It should be noted that for a given temperature T each spectrum measured with a non-zero E depends on both $\omega_{\mathrm{TO}j}(T, E)$ and $\omega_{\mathrm{TO}j}(T, 0)$.

In some spectra we observed signatures of TO4 mode splitting (Figs. 4.19a,b,c). In order to fit these spectra we supplemented the model (4.10) with an additional harmonic oscillator describing the new mode denoted TO4′. In a similar way the oscillator strength $f_{\mathrm{TO4}'}$ and the damping $\Gamma_{\mathrm{TO4}'}$ of this mode were assumed to be temperature and field independent, and its bare frequency $\omega_{\mathrm{TO4}'}(T, E)$ both field and temperature dependent. The splitting of the TO4 mode is clearly observed at 220 K (Fig. 4.19b) and it becomes highly pronounced with the temperature decrease. The situation is not clear at 250 K (Fig. 4.19a), however, the fact that the fit including TO4′ mode yields a twice reduced least square sum suggests that splitting of the mode has already started. Qualitatively similar splitting of TO4 mode was recently observed on a similar film below 200 K in the reflectance spectra polarized along [001] [241]. The authors suggested that it was connected to the antiferrodistortive phase transition observed at ∼180 K. According to our findings (for the polarization along [110]) the splitting manifests itself even at higher temperatures, we thus conclude that it is related to the symmetry breaking at the ferroelectric phase transition which occurs close to the room temperature in these thin film structures.

Complete picture of the TO4 mode frequency tuning by the electric field is presented in Fig. 4.19d. One can observe a linear dependence of the mode frequency on applied bias. The TO4 mode field-induced hardening is of up to 2 cm^{-1} for the maximum bias, whereas the split TO4′ mode hardens by up to 8 cm^{-1} at 120 K. The tiny field-induced relative changes in the mode frequency (0.4 % and 1.5 % for TO4 and TO4′, respectively) can be easily detected in our experiments due to an underdamped nature ($\Gamma_{\mathrm{TO4}} \approx 13$ cm^{-1}) of the high-frequency modes in STO.

The splitting of TO4 mode with decreasing temperature is shown for zero and maximum (93 kV/cm) bias in the inset of Fig. 4.19d. Externally applied bias field enhances the splitting of the modes. We observed the TO4 mode splitting of about 7 cm^{-1} in unbiased film for [110] polarization of FIR radiation while a splitting of ∼14 cm^{-1} was reported by Nuzhnyy et al. [241] for [001] polarization. This difference might be a signature of the lack of fourfold axis in the strained sample.

The tuning of the TO2 mode eigenfrequency is observed in the spectra near 169 cm^{-1} as a tiny dip (Fig. 4.18). Although the electric-field tunability of the TO2 mode frequency (∼1 cm^{-1} at 67 kV/cm and room temperature) is comparable to that of TO4 mode, the sensitivity of the experimental spectra is dramatically different for these two modes. This fact is again related to the impedance mismatch between STO and DSO. We calculated the refractive indices for both materials using the corresponding models (see Fig. 4.20); and we found a large contrast between the refractive indices in the spectral range of TO4 mode ($n_{\mathrm{STO}} \approx 3.8$, $n_{\mathrm{DSO}} \approx 0.3$) while this contrast is small close to TO2 mode ($n_{\mathrm{STO}} \approx 5.5$, $n_{\mathrm{DSO}} \approx 6.5$). This is the reason why we obtained only a rough estimation of TO2 mode tuning and we were not able to perform any deeper characterization. A similar hardening of the TO2 mode was reported by Akimov et al. [242].

We did not detect the silent TO3 mode in our experiments, however, it was observed under applied electric field by Raman scattering both in bulk STO [191, 243] and in thin films [242].

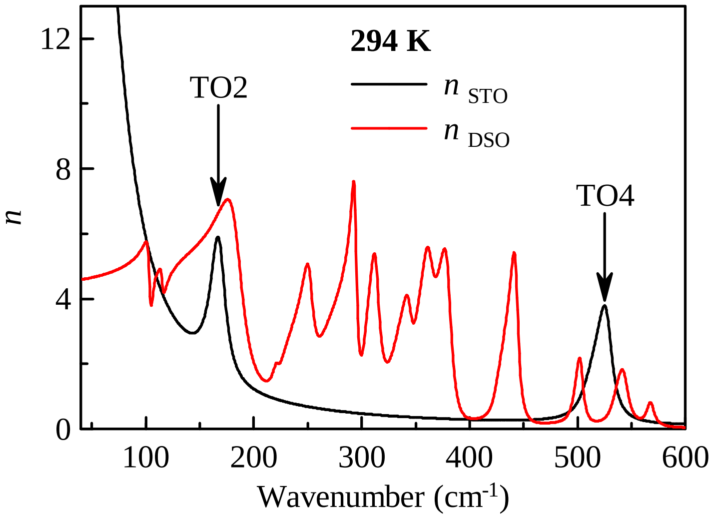

Figure 4.20: Calculated refractive indices for STO and DSO at room temperature using the model (4.10) and the four parameters model (2.22) for STO and DSO, respectively.

4.4.3 Summary

In this part of the work we have shown the electric field-induced tuning of high frequency polar phonons in the strained thin film structures. This phenomenon is in a tight relation to the tuning of TO1 (soft) mode, which is responsible for the tunability of THz pemittivity. Eigenvectors of polar phonons in STO are strongly mixed by the Coulomb interaction, and it is thus natural that the change in the soft-mode frequency should influence other polar modes. This follows also from the first principle calculations of perovskite oxides showing that the longitudinal phonon frequency of the TO1 soft mode corresponds to the mode usually denoted as LO4 mode near 800 cm^{-1} [244].

The electric-field-induced tuning of hard TO2 and TO4 modes is smaller than that of the soft mode. Detailed analysis performed in the case of TO4 mode revealed its splitting below 220 K, which might be induced by the ferroelectric phase transition observed in the strained structures. This splitting exhibits dependence on the applied field; this implies that the eigenvector of the split TO4$'$ mode experiences a stronger coupling to the eigenvector of TO1 mode than that of TO4 mode.

4.5 Conclusions

Study of strained thin films of incipient ferroelectrics using mainly the time-domain THz spectroscopy and a large number of other experimental techniques is reported in this chapter. The THz spectroscopy covering the spectral range of the soft mode, which is at the origin of the ferroelectric phase transition, allowed us to extract a set of important parameters of the materials. We found that these parameters reflect a correlation between the dielectric properties and microscopic structure of the material and even the lattice strain.

We have investigated several epitaxially grown thin film STO/DSO structures. All the studied structures were shown to exhibit the paraelectric-to-ferroelectric phase transition close to the room temperature. The observed variation of the phase transition temperature and the THz dielectric response among the structures was ascribed to a partial strain relaxation. Nevertheless, the structures with a high number of STO/DSO bilayers (≥ 6) still experience the phase transition confirming that our approach to maintain STO layers strained by the sequential inserting of thin film layers of DSO is valid.

We have shown that small deviations in STO thin film stoichiometry strongly affects its dielectric response in the radio and THz frequency ranges. The observed strain-induced phase transition temperature was found to be different for the films with various off-stoichiometry deviations. We think that this is connected with a rapid strain relaxation on structure defects originating from the non-stoichiometric composition and leading to a relaxor-type dielectric response of the films. Indeed, the nominally stoichiometric STO film exhibits the highest phase transition temperature (about 300 K), the highest low-frequency permittivity value (70000) and the lowest soft-mode frequency (23 cm^{-1}) at the phase transition temperature.

We have observed an electric-field-induced tuning of the hard polar modes in strained STO films using the far infrared Fourier spectroscopy. This phenomenon is explained by a strong mixing of polar phonons eigenvectors.

To explain the temperature and electric-field evolution of the dielectric spectra of the investigated structures a general model has been proposed. It includes a damped harmonic oscillator coupled to a Debye relaxation which describe the soft-mode and central-mode contributions to the permittivity, respectively. The model satisfactorily fits all the spectra of the investigated STO/DSO structures. Moreover, it is able to fit well the THz dielectric response of a polycrystalline thin film of KTO deposited on sapphire substrate. Results of this fitting suggest a ferroelectric phase transition occurrence near 60 K. We suppose that the phase transition in these films is again induced by the strain coming from the substrate. Finally, let us note that the same model probably describes the soft-mode dynamics in the whole family of $(\mathrm{BaSr})\mathrm{TiO}_3$ compounds [222].

We think that the findings presented in this chapter provide valuable information from the fundamental science point of view and, consequently, helpful references for further development of new dielectric tunable structures operating in the THz frequency range and below.

Chapter 5

Conclusions and outlooks

A study of materials and structures with tunable THz dielectric properties is presented in this thesis. The experimental characterization of investigated materials was performed primarily using the time-domain THz spectroscopy, however, in some cases other experimental techniques were involved to obtain a more complete picture of evolution of the dielectric properties with temperature and with electric field and to explain the observed behavior. The investigated samples are divided in two categories: bulk materials, and thin films. The main results of this work are summarized below:

Bulk materials

- A comprehensive study of an electric-field tunability of the THz dielectric properties of $SrTiO_3$ single crystals was performed up to the room temperature. A highly anharmonic potential of the ferroelectric soft mode is shown to be at the origin of the dielectric tunability of $SrTiO_3$. Its anharmonicity was characterized with the help of two different electrode structures deposited on the samples. The temperature and electric-field behavior of the THz dielectric spectra of $SrTiO_3$ single crystal is fully governed by the soft-mode dynamics, and no other relaxation modes were observed.

  One of possible applications of $SrTiO_3$ dielectric tunability was proposed: a one-dimensional photonic crystal with an electric-field-tunable defect mode in a forbidden band was prepared and characterized in a broad temperature range.

- Investigation of the dielectric properties of a high-density $KTaO_3$ ceramics in a broad frequency range has revealed that the temperature behavior of its permittivity is similar to that of $KTaO_3$ single crystal. The low-frequency (1 kHz) permittivity value very close to that found in single crystals suggests that the permittivity of the studied ceramics is mainly governed by polar phonons, in other words, it is of intrinsic origin. However, the microwave loss tangent acquired higher values than those in single crystals, which indicates the presence of defects in the material.

Thin film materials

- A systematic study of several epitaxially grown thin film $SrTiO_3/DyScO_3$ structures was done. All the structures exhibited ferroelectric phase transition induced by strain near the room temperature. A partial relaxation of the strain is believed to be at the origin of the observed variation of the phase transition temperature and of the THz dielectric spectra among the studied structures. An approach consisting in intercalating of $SrTiO_3$ layers with $DyScO_3$ layers in order to maintain $SrTiO_3$ films strained was shown to be valid up to the total $SrTiO_3$ thickness of 400 nm.

- Small deviations in stoichiometry of strained $SrTiO_3$ films were shown to have a strong impact on the dielectric properties in the radio and THz frequency ranges. Films with various off-stoichiometric deviations exhibited different phase transition temperatures. The nominally stoichiometric sample showed the highest phase transition temperature, the highest low-frequency permittivity value and the lowest soft-mode frequency at the phase transition. The off-stoichiometric samples exhibited a relaxor-type dielectric response. The observed differences are thought to be connected with a rapid strain relaxation on structure defects due to non-stoichiometry.

- A general model has been proposed to describe the temperature and electric-field behavior of THz dielectric properties of the investigated $SrTiO_3/DyScO_3$ structures. It consists of a damped harmonic oscillator coupled to a Debye relaxation which describe the soft-mode and the central mode contribution to the permittivity, respectively.

- An electric-field-induced tuning of the hard polar phonons in strained $SrTiO_3$ films was observed and characterized using the far infrared Fourier spectroscopy. A strong mixing of eigenvectors of polar phonons is at the origin of this phenomenon.

- The ferroelectric phase transition occurring near 60 K was revealed in a polycrystalline thin film of $KTaO_3$ deposited on sapphire substrate. The strain coming from the substrate is supposed to be at the origin of the observed phase transition. The model for the dielectric response proposed for $SrTiO_3/DyScO_3$ structures was able to fit well the permittivity in the THz range of the polycrystalline $KTaO_3$ film.

Although we did not observe any relaxation mode in the THz dielectric spectra of $SrTiO_3$ single crystals even at the lowest temperatures, this feature was noticeable in the THz response of all the investigated thin film structures including the $KTaO_3$ film on sapphire. These experimental findings are in agreement with molecular dynamic simulations [221, 222, 245], which were extensively done for the (Ba,Sr)TiO_3 system [222]. It seems that the existence and the temperature range of the existence of the central mode is related to the temperature of the ferroelectric phase transition; the dynamics of the central mode is thermally activated following the Arrhenius law. As the transition temperature increases with an increasing content of Ba, the central mode is observed in a broader temperature range in samples with a larger content of Ba.

Let us note that in these simulations the ferroelectric phase transition does exist also in a pure $SrTiO_3$ (at ∼100 K) and the central mode appears in a very narrow range of a few K near the phase transition. The existence of the transition in the simulations is related to the fact that the local ferroelectric soft modes are the only degrees of freedom taken into account in the simulations. It means that the motion corresponding to the zone-boundary mode connected to the tilt of the oxygen octahedra and leading to the antiferrodistortive phase transition into ferroelastic phase is not taken into account. Experimentally, the antiferrodistortive phase transition occurs at 105 K and obviously the tilt of the octahedra prevails over the polar ordering.

Thus, in the theoretical model the width of the temperature range where the central mode exists is clearly correlated to the value of the ferroelectric transition temperature itself. In the pure $SrTiO_3$ single crystal we did not observe any central mode, which is in agreement with the simulations taking into account the fact that the ferroelectric phase transition does not really occur.

In strained $SrTiO_3$ films the phase transition occurs close to the room temperature and it is accompanied by an emergence of the central mode. This is again supported by the molecular dynamic simulations for strained STO films [245]. The strength of the central mode in the experiments is then related not only to the intrinsic behavior of strained $SrTiO_3$ but also to the existence of defects in the thin films.

We hope that the results of this thesis are valuable from the point of view of the physics of ferroelectrics and that they will serve as helpful references for further development of tunable structures operating in the THz range and below. It is known that planar metallic metamaterial structures with suitably chosen geometrical parameters may exhibit electromagnetic resonances. Recently, such metamaterials deposited on $SrTiO_3$ single crystal substrates were shown [95] to possess thermally tunable dielectric resonance in the THz frequency range. However, the presented structure showed a low total transmission because of substantial dielectric losses in a bulk $SrTiO_3$ substrate. Using similar idea a metallic metamaterial structure can be deposited on strained $SrTiO_3$ films. In this case, one can obtain a structure exhibiting an electric-field-tunable resonance and a higher transmission due to a thinner layer of the ferroelectric material with the thickness comparable to the penetration depth of the bias field.

We also wish to push further the investigation of the dielectric properties of $KTaO_3$ single crystals and thin films versus temperature and electric field. Despite the fact that $KTaO_3$ possesses a lower permittivity than $SrTiO_3$ it might exhibit a higher anharmonicity of the soft-mode potential. Consequently, the resulting electric-field tunability may be sufficiently large to be considered for potential applications.

Bibliography

[1] M. E. Lines and A. M. Glaas. *Principles and application of ferroelectrics and related materials.* Clarendon Press, Oxford (1977).

[2] G. A. Samara. *Solid state physics, Chapter: Ferroelectricity revisited–Advances in materials and physics*, vol. 56. Academic press (2001).

[3] J. Valasek. Piezo-electric and allied phenomena in rochelle salt. *Phys. Rev.* **17**, 475 (1921).

[4] G. Busch and P. Scherrer. A new seignette-electric substance. *Naturwiss* **23**, 737 (1935).

[5] B. Wul and I. M. Goldman. *C. R. Acad. Sci., URSS* **46**, 139 (1945).

[6] B. Matthias. New ferroelectric crystals. *Phys. Rev.* **75**, 1771 (1949).

[7] B. Matthias and J. Remeika. Ferroelectricity in the ilmenite structure. *Phys. Rev.* **76**, 1886 (1949).

[8] G. Shirane, S. Hoshino, and K. Suzuki. Crystal structure of lead titanate and of lead-barium titanate. *J. Phys. Soc. Jpn.* **5**, 453 (1950).

[9] J. Petzelt, S. Kamba, and J. Hlinka. *New developments in advanced functional ceramics, Chapter: Ferroelectric soft modes in ceramics and films.* Transworld research network, Kerala, India (2007).

[10] L. Landau and E. Lifshits. *Statistical physics.* Addison-Wesley, New York (1958).

[11] R. Lyddane, R. Sachs, and E. Teller. On the polar vibrations of alkali halides. *Phys. Rev.* **59**, 673 (1941).

[12] W. Cochran. Crystal stability and the theory of ferroelectricity. *Phys. Rev. Lett.* **3**, 412 (1959).

[13] J. Petzelt, G. V. Kozlov, and A. Volkov. Dielectric spectroscopy of paraelectric soft mode. *Ferroelectrics* **73**, 101 (1987).

[14] J. Hlinka, J. Petzelt, S. Kamba, D. Noujni, and T. Ostapchuk. Infrared dielectric response of relaxor ferroelectrics. *Phase Transitions* **79**, 41 (2006).

[15] E. Buixaderas, S. Kamba, and J. Petzelt. Lattice dynamics and central-mode phenomena in the dielectric response of ferroelectrics and related materials. *Ferroelectrics* **308**, 131 (2004).

[16] J. Slater. The Lorentz correction in barium titanate. *Phys. Rev.* **78**, 748 (1950).

[17] J. Last. Infrared-absorption studies on barium titanate and related materials. *Phys. Rev.* **105**, 1740 (1957).

[18] J. Axe. Apparent ionic charges and vibrational eigenmodes of $BaTiO_3$ and other perovskites. *Phys. Rev.* **105**, 1740 (1967).

[19] W. G. Spitzer, R. C. Miller, D. A. Kleinman, and L. E. Howarth. Far infrared dielectric dispersion in $BaTiO_3$, $SrTiO_3$, and TiO_2. *Phys. Rev.* **126**, 1710 (1960).

[20] C. H. Perry, B. Khanna, and G. Rupprecht. Infrared studies of perovskite titanates. *Phys. Rev.* **135**, A408 (1964).

[21] R. Joseph and B. Silverman. Optical modes of the perovskite structure. *J. Phys. Chem. Solids* **24**, 1349 (1963).

[22] O. Vendik, E. Hollmann, A. Kozyrev, and A. Prudan. Ferroelectric tuning of planar and bulk microwave devices. *J. Superconductivity* **12**, 325 (1999).

[23] A. K. Tagantsev, V. O. Sherman, K. F. Astafiev, J. Venkatesh, and N. Setter. Ferroelectric materials for microwave tunable applications. *J. Electroceram.* **11**, 5 (2003).

[24] P. Kužel and F. Kadlec. Tunable structures and modulators for THz light. *Comptes Rendus Physique* **9**, 197 (2008).

[25] H.-T. Chen, J. F. O'Hara, A. K. Azad, and A. J. Taylor. Manipulation of terahertz radiation using metamaterials. *Laser Photonics Rev.* **5**, 513 (2011).

[26] P. Kužel and H. Němec. *Terahertz Spectroscopy and Imaging, Chapter: Metamaterials*, vol. 171. Springer Series in Optical Sciences, Berlin (2013).

[27] I. Libon, S. Baumgrtner, M. Hempel, N. Hecker, J. Feldmann, M. Koch, and P. Dawson. An optically controllable terahertz filter. *Appl. Phys. Lett.* **76**, 2821 (2000).

[28] L. Fekete, J. Y. Hlinka, F. Kadlec, P. Kužel, and P. Mounaix. Active optical control of the terahertz reflectivity of high-resistivity semiconductors. *Opt. Lett.* **30**, 1992 (2005).

[29] T. Nozokido, H. Minamide, and K. Mizuno. Modulation of submillimeter wave radiation by laser-produced free carriers in semiconductors. *Electron. Comm. Jpn. II* **80**, 1 (1997).

[30] C. Karaalioglu, I.-C. Chen, M. Brucherseifer, A. Meshal, and R. Martini. Highly efficient THz modulation using optically excited silicon. *Proc. SPIE* **5790**, 263 (2005).

[31] S. Biber, D. Schneiderbanger, and L.-P. Schmidt. Design of a controllable attenuator with high dynamic range for THz-frequencies based on optically stimulated free carriers in high-resistivity silicon. *Frequenz* **59**, 141 (2005).

[32] T. Kleine-Ostmann, P. Dawson, K. Pierz, G. Hein, and M. Koch. Room-temperature operation of an electrically driven terahertz modulator. *Appl. Phys. Lett.* **84**, 3555 (2004).

[33] M. DiDomenico, D. A. Johnson, and R. H. Pantell. Ferroelectric Harmonic Generator and the Large Signal Microwave Characteristics of a Ferroelectric Ceramic. *J. Appl. Phys.* **33**, 1697 (1962).

[34] M. Lancaster, J. Powell, and A. Porch. Thin-film ferroelectric microwave devices. *Supercond. Sci. Technol.* **11**, 1323 (1998).

[35] X. Xi, H. Li, W. Si, A. Sirenko, I. Akimov, J. Fox, A. Clark, and J. Hao. Oxide thin films for tunable microwave devices. *J. Electroceram.* **4**, 393 (2000).

[36] F. A. Miranda, F. W. V. Keuls, R. R. Romanofsky, C. H. Mueller, S. Alterovitz, and G. Subramanyam. Ferroelectric thin films-based technology for frequency- and phase-agile microwave communication applications. *Integrated Ferroelectrics* **42**, 131 (2001).

[37] O. Vendik. *Ferroelectrics in microwaves (in Russian)* (1979).

[38] S. Gevorgian, E. Carlsson, E.Wikborg, and E. Kollberg. Tunable microwave devices based on bulk and thin film ferroelectrics. *Integrated Ferroelectrics* **22**, 765 (1998).

[39] S. Wolf and D. Treger. Frequency Agile Materials for Electronics (FAME)-Progress in the DARPA Program. *Integrated Ferroelectrics* **42**, 39 (2002).

[40] A. Deleniv, A. Eriksson, and S. Gevorgian. Design of narrow-band tunable band-pass filters based on dual mode $SrTiO_3$ disc resonators. *2002 IEEE MTT-S International Microwave Symposium Digest* **1-3**, 1197 (2002).

[41] V. Keis, A. Kozyrev, M. Khazov, J. Sok, and J. Lee. 20 GHz tunable filter based on ferroelectric $(Ba,Sr)TiO_3$ film varactors. *Electronics Letters* **34**, 1107 (1998).

[42] B. Moeckly and Y. Zhang. Strontium titanate thin films for tunable $YBa_2Cu_3O_7$ microwave filters. *IEEE Transaction on Applied Superconductivity* **11**, 450 (2001).

[43] I. Vendik, O. Vendik, V. Pleskachev, A. Svishchev, and R. Woerdenweber. Design of tunable ferroelectric filters with a constant fractional band width. *2002 IEEE MTT-S International Microwave Symposium Digest* **3**, 1461 (2001).

[44] P. Bao, T. Jackson, X. Wang, and M. Lancaster. Barium strontium titanate thin film varactors for room-temperature microwave device applications. *J. Phys. D: Appl. Phys.* **41**, 06 3001 (2008).

[45] B. Acikel, T. Taylor, P. Hansen, J. Speck, and R. York. A new high performance phase shifter using $Ba_xSr_{1-x}TiO_3$ thin films. *IEEE Microwave and Wireless Components Letters* **12**, 237 (2002).

[46] A. Kozyrev, A. Ivanov, A. Prudan, O. Soldatenkov, E. Hollmann, V. Loginov, D. Ginley, and T. Rivkin. Microwave phase shifter employing $SrTiO_3$ ferroelectric varactors. *Integrated Ferroelectrics* **24**, 287 (1999).

[47] V. Sherman, K. Astafiev, N. Setter, A. Tagantsev, O. Vendik, I. Vendik, S. Hoffmann-Eifert, U. Bottger, and R. Waser. Digital reflection-type phase shifter based on a ferroelectric planar capacitor. *IEEE Microwave and Wireless Components Letters* **11**, 407 (2001).

[48] F. Miranda, G. Subramanyam, F. Keuls, R. Romanofsky, J. Warner, and C. Mueller. Design and development of ferroelectric tunable microwave components for Ku- and K-band satellite communication systems. *IEEE Trans. on Microwave Theory and Techniques* **48**, 1181 (2000).

[49] T. Samoilova, K. Astafiev, T. Rivkin, and D. Ginley. Frequency conversion in coplanar waveguide based on $Ba_xSr_{1-x}TiO_3$ film. *J. Appl. Phys.* **90**, 5703 (2001).

[50] J. Colom, R. Rodrigues-Solis, J. Almodovar, and M. Castaneda. Design and simulation of a tunable multilayer Lange coupler. *Integrated Ferroelectrics* **42**, 313 (2002).

[51] A. Pashkin. *Terahertz spectroscopy of ferroelectrics and related materials.* Ph.D. thesis, Charles university in Prague (2004).

[52] V. Gurevich and A. Tagantsev. Intrinsic dielectric loss in crystals. *Adv. Phys.* **40**, 719 (1991).

[53] G. J. Coombs and R. A. Cowley. Piezoelectric and Pyroelectric Crystals: I. Dielectric Properties. *J. Phys. C* **6**, 121 (1973).

[54] V. Gurevich. Dielectric-relaxation in crystals. *Fiz. Tverd. Tela* **21**, 3453 (1979).

[55] C. Kittel. *Introduction to Solid State Physics.* John Wiley & Sons, Inc., New York, London (1971).

[56] E. Schlöman. Dielectric losses in ionic crystals with disordered charge distributions. *Phys. Rev.* **135**, A413 (1964).

[57] J. Petzelt, T. Ostapchuk, I. Gregora, I. Rychetský, S. Hoffmann-Eifert, A. Pronin, Y. Yuzyuk, B. Gorshunov, S. Kamba, V. Bovtun, J. Pokorný, M. Savinov, V. Porokhonskyy, D. Rafaja, P. Vaněk, A. Almeida, M. Chaves, A. Volkov, M. Dressel, and R. Waser. Dielectric, infrared, and Raman response of undoped $SrTiO_3$ ceramics: Evidence of polar grain boundaries. *Phys. Rev. B* **64**, 18 4111 (2001).

[58] O. Vendik and S. Zubko. Ferroelectric phase transition and maximum dielectric permittivity of displacement type ferroelectrics ($Ba_xSr_{1-x}TiO_3$). *J. Appl. Phys.* **88**, 5343 (2000).

[59] E. Ngo, P. Joshi, M. Cole, and C. Hubbard. Electrophoretic deposition of pure and MgO-modified $Ba_{0.6}Sr_{0.4}TiO_3$ thick films for tunable microwave devices. *Appl. Phys. Lett.* **79**, 248 (2001).

[60] L. Wu, S. Wu, F.-C. Chang, Y.-T. Shen, and Y.-C. Chen. DC field dependence of dielectric constant and loss factor of Al_2O_3-doped barium strontium titanate for application in phased array antennas. *J. Materials Science* **35**, 5945 (2000).

[61] L. Sengupta and S. Sengupta. Breakthrough advances in low loss, tunable dielectric materials. *Mat. Res. Innovat.* **2**, 278 (1999).

[62] C. Ang, A. Bhalla, R. Guo, and L. Cross. Effect of dc bias on dielectric properties of $Cd_2Nb_2O_7$ ceramics. *J. Appl. Phys.* **90**, 2465 (2001).

[63] M. Daglish, M. Presland, and S. Batbedat. Alternative choices for voltage-tunable dielectrics. *Integrated Ferroelectrics* **39**, 1289 (2001).

[64] D. Li and M. Subramanian. Noval tunable ferroelectric compositions: $Ba_{1-x}Ln_xTi_{1-y}M_yO_3$ (Ln = La, Sm, Gd, Dy, M = Al, Fe, Cr). *Solid State Science* **2**, 507 (2000).

[65] S. Triebwasser. Study of ferroelectric phase transitions of solid-solution single crystals of $KNbO_3$-$KTaO_3$. *Phys. Rev.* **114**, 63 (1959).

[66] J. H. Haeni, P. Irvin, W. Chang, R. Uecker, P. Reiche, Y. L. Li, S. Choudhury, W. Tian, M. E. Hawley, B. Craigo, A. K. Tagantsev, X. Q. Pan, S. K. Streiffer, L. Q. Chen, S. W. Kirchoefer, J. Levy, and D. G. Schlom. Room-temperature ferroelectricity in strained $SrTiO_3$. *Nature* **430**, 758 (2004).

[67] V. Veselago. Electrodynamics of substances with simultaneously negative values of ε and μ. *Sov. Phys. Usp.* **10**, 509 (1968).

[68] J. B. Pendry, A. J. Holden, and W. J. Stewart. Extremely low frequency plasmons in metallic mesostructures. *Phys. Rev. Lett.* **76**, 4773 (1996).

[69] J. B. Pendry, A. J. Holden, D. J. Robbins, and W. J. Stewart. Low frequency plasmons in thin-wire structures. *J. Phys.: Condens. Matter* **10**, 4785 (1998).

[70] J. B. Pendry, A. J. Holden, D. J. Robbins, and W. J. Stewart. Magnetism from conductors and enhanced nonlinear phenomena. *IEEE Trans. Microw. Theory Tech.* **47**, 2075 (1999).

[71] J. B. Pendry. Negative refraction makes a perfect lens. *Phys. Rev. Lett.* **85**, 3966 (2000).

[72] D. R. Smith, W. J. Padilla, D. C. Vier, S. C. Nemat-Nasser, and S. Schultz. Composite medium with simultaneously negative permeability and permittivity. *Phys. Rev. Lett.* **84**, 4184 (2000).

[73] T. J. Yen, W. J. Padilla, N. Fang, D. C. Vier, D. R. Smith, J. B. Pendry, D. N. Basov, and X. Zhang. Terahertz magnetic response from artificial materials. *Science* **303**, 1494 (2004).

[74] H.-T. Chen, W. J. Padilla, J. M. O. Zide, A. C. Gossard, A. J. Taylor, and R. D. Averitt. Active terahertz metamaterial devices. *Nature* **444**, 597 (2006).

[75] R. Marqués, F. Martín, and M. Sorolla. *Metamaterials with negative parameters.* John Wiley & Sons, Inc., Hoboken, New Jersey (2008).

[76] S. A. Ramakrishna and T. M. Grzegorczyk. *Physics and applications of negative refractive index materials.* CRC Press, Boca Raton, London, New York (2009).

[77] W. Cai and V. Shalaev. *Opticals metamaterials.* Springer (2010).

[78] H. Němec, P. Kužel, F. Kadlec, C. Kadlec, R. Yahiaoui, and P. Mounaix. Tunable terahertz metamaterials with negative permeability. *Phys. Rev. B* **79**, 24 1108 (2009).

[79] H. Tao, A. C. Strikwerda, K. Fan, W. J. Padilla, X. Zhang, and R. D. Averitt. Reconfigurable terahertz metamaterials. *Phys. Rev. Lett.* **103**, 14 7401 (2009).

[80] W. L. Chan, H.-T. Chen, A. J. Taylor, I. Brener, and M. J. Cich. A spatial light modulator for terahertz beams. *Appl. Phys. Lett.* **94**, 21 3511 (2009).

[81] H.-T. Chen, J. F. O'Hara, A. J. Taylor, R. D. Averitt, C. Highstrete, M. Lee, and W. J. Padilla. Complementary planar terahertz metamaterials. *Opt. Express* **15**, 1084 (2007).

[82] W. J. Padilla, M. T. Aronsson, C. Highstrete, M. Lee, A. J. Taylor, and R. D. Averitt. Electrically resonant terahertz metamaterials: theoretical and experimental investigations. *Phys. Rev. B* **75**, 04 1102 (2007).

[83] A. K. Azad, A. J. Taylor, E. Smirnova, and J. F. O'Hara. Characterization and analysis of terahertz metamaterials based on rectangular split-ring resonators. *Appl. Phys. Lett.* **92**, 01 1119 (2008).

[84] H.-T. Chen, W. J. Padilla, M. J. Cich, A. K. Azad, R. D. Averitt, and A. J. Taylor. A metamaterial solid-state terahertz phase modulator. *Nature Photon.* **3**, 148 (2009).

[85] O. Paul, C. Imhof, B. Lägel, S. Wolff, J. Heinrich, S. Höfling, A. Forchel, R. Zengerle, R. Beigang, and M. Rahm. Polarization-independent active metamaterial for high-frequency terahertz modulation. *Opt. Express* **17**, 819 (2009).

[86] H.-T. Chen, H. Lu, A. K. Azad, R. D. Averitt, A. C. Gossard, S. A. Trugman, J. F. O'Hara, and A. J. Taylor. Electronic control of extraordinary terahertz transmission through subwavelength metal hole arrays. *Opt. Express* **16**, 7641 (2008).

[87] W. J. Padilla, A. J. Taylor, C. Highstrete, M. Lee, and R. D. Averitt. Dynamical electric and magnetic metamaterial response at terahertz frequencies. *Phys. Rev. Lett.* **96**, 10 7401 (2006).

[88] H.-T. Chen, W. J. Padilla, J. M. O. Zide, S. R. Bank, A. C. Gossard, A. J. Taylor, and R. D. Averitt. Ultrafast optical switching of terahertz metamaterials fabricated on ErAs/GaAs nanoislands superlattices. *Opt. Lett.* **32**, 1620 (2007).

[89] C. Kadow, S. B. Fleischer, J. P. Ibbetson, J. E. Bowers, A. C. Gossard, J. W. Dong, and C. J. Palmstrøm. Self-assembled ErAs islands in GaAs: Growth and subpicosecond carrier dynamics. *Appl. Phys. Lett.* **75**, 3548 (1999).

[90] Y. Shi, Q. Zhou, W. Liu, J. Liu, and C. Zhang. Anomalous transmission of terahertz waves in arrays of double-ring resonators induced by a 400 nm pump pulse. *Appl. Phys. Lett.* **98**, 19 1112 (2011).

[91] J.-M. Manceau, N.-H. Shen, M. Kafesaki, C. M. Soukoulis, and S. Tzortzakis. Dynamics response of metamaterials in the terahertz regime: blueshift tunability and broadband phase modulation. *Appl. Phys. Lett.* **96**, 02 1111 (2010).

[92] H.-T. Chen, J. F. O'Hara, A. K. Azad, A. J. Taylor, R. D. Averitt, D. B. Shrekenhamer, and W. J. Padilla. Experimental demonstration of frequency-agile terahertz metamaterials. *Nature Photon.* **2**, 295 (2008).

[93] N.-H. Shen, M. Kafesaki, T. Koschny, L. Zhang, E. N. Economou, and C. M. Soukoulis. Broadband blueshift tunable metamaterials and dual-band switches. *Phys. Rev. B* **79**, 16 1102 (2009).

[94] Y. Yuan, C. Bingham, T. Tyler, S. Palit, T. H. Hand, W. J. Padilla, N. M. Jokerst, and S. A. Cummer. A dual-resonant terahertz metamaterial based on single-particle electricfield-coupled resonators. *Appl. Phys. Lett.* **93**, 19 1110 (2008).

[95] R. Singh, A. K. Azad, Q. X. Jia, A. J. Taylor, and H.-T. Chen. Thermal tunability in terahertz metamaterials fabricated on strontium titanate single-crystal substrates. *Opt. Lett.* **36**, 1230 (2011).

[96] J. Wu, B. Jin, Y. Xue, C. Zhang, H. Dai, L. Zhang, C. Cao, L. Kang, W. Xu, J. Chen, and P. Wu. Tuning of superconducting niobium nitride terahertz metamaterials. *Opt. Express* **19**, 12 021 (2011).

[97] Q.-Y. Wen, H.-W. Zhang, Q.-H. Yang, Y.-S. Xie, K. Chen, and Y.-L. Liu. Terahertz metamaterials with VO_2 cut-wires for thermal tunability. *Appl. Phys. Lett.* **97**, 02 1111 (2010).

[98] G. He, R.-X. Wu, Y. Poo, and P. Chen. Magnetically tunable double-negative material composed of ferrite-dielectric and metallic mesh. *J. Appl. Phys.* **107**, 09 3522 (2010).

[99] B. Ozbey and O. Aktas. Continuously tunable terahertz metamaterial employing magnetically actuated cantilevers. *Opt. Express* **19**, 5741 (2011).

[100] E. Yablonovitch. Inhibited spontaneous emission in solid-state physics and electronics. *Phys. Rev. Lett.* **58**, 2059 (1987).

[101] K. Sakoda. *Optical properties of photonic crystals.* Springer, Berlin (2001).

[102] J. Joannopoulos, S. Johnson, J. Winn, and R. Meade. *Photonic crystals.* Princeton university press, Princeton and Oxford (2008).

[103] E. Yablonovitch, T. J. Gmitter, R. D. Meade, A. M. Rappe, K. D. Brommer, and J. D. Joannopoulos. Donor and acceptor modes in photonic band-structure. *Phys. Rev. Lett.* **67**, 3380 (1991).

[104] S. L. Mccall, P. M. Platzman, R. Dalichaouch, D. R. Smith, and S. Schultz. Microwave propagation in two-dimensional dielectric lattices. *Phys. Rev. Lett.* **67**, 2017 (1991).

[105] B. Temelkuran and E.Özbay. Experimental demonstration of photonic crystal based waveguides. *Appl. Phys. Lett.* **74**, 486 (1999).

[106] M. Schuster and N. Klein. Controlled excitation of electromagnetic band-gap line and point defect modes at microwave frequencies. *J. Appl. Phys.* **93**, 3182 (2003).

[107] B. Wild, R. Ferrini, R. Houdré, M. Mulot, S. Anand, and C. J. M. Smith. Temperature tuning of the optical properties of planar photonic crystal microcavities. *Appl. Phys. Lett.* **84**, 846 (2004).

[108] X. Hu, Q. Zhang, Y. Liu, B. Cheng, and D. Zhang. Ultrafast three-dimensional tunable photonic crystal. *Appl. Phys. Lett.* **83**, 2518 (2003).

[109] Y. Lai, W. Zhang, L. Zhang, J. A. R. Williams, and I. Bennion. Optically tunable fiber grating transmission filters. *Opt. Lett.* **28**, 2446 (2003).

[110] E. Özbay and B. Temelkuran. Reflection properties and defect formation in photonic crystals. *Appl. Phys. Lett.* **69**, 743 (1996).

[111] H. Němec, L. Duvillaret, F. Quemeneur, and P. Kužel. Defect modes caused by twinning in one-dimensional photonic crystals. *J. Opt. Soc. Am. B* **21**, 548 (2004).

[112] H. Němec, L. Duvillaret, F. Garet, P. Kužel, P. Xavier, J. Richard, and D. Rauly. Thermally tunable filter for terahertz range based on a one-dimensional photonic crystal with a defect. *J. Appl. Phys.* **96**, 4072 (2004).

[113] H. Němec, P. Kužel, L. Duvillaret, A. Pashkin, M. Dressel, and M. T. Sebastian. Highly tunable photonic crystal filter for the terahertz range. *Opt. Lett.* **30**, 549 (2005).

[114] L. Fekete, F. Kadlec, H. Němec, and P. Kužel. Fast one-dimensional photonic crystal modulators for the terahertz range. *Opt. Express* **15**, 8898 (2007).

[115] L. Fekete, F. Kadlec, P. Kužel, and H. Němec. Ultrafast opto-terahertz photonic crystal modulator. *Opt. Lett.* **32**, 680 (2007).

[116] H. Eisele and G. I. Haddad. Two-terminal millimeter-wave sources. *IEEE Trans. on Microwave Theory and Techniques* **46**, 739 (1998).

[117] F. J. Trew. High-frequency solid-state electronic devices. *IEEE Trans. on Microwave Theory and Techniques* **52**, 638 (2005).

[118] D. H. Auston, K. P. Cheung, and P. R. Smith. Picosecond photoconducting Hertzian dipoles. *Appl. Phys. Lett.* **45**, 284 (1984).

[119] C. Fattinger and D. Grischkowsky. Terahertz beams. *Appl. Phys. Lett.* **54**, 490 (1989).

[120] D. Grischkowsky, S. Keiding, M. V. Exter, and C. Fattinger. Far-infrared time-domain spectroscopy with terahertz beams of dielectrics and semiconductors. *J. Opt. Soc. Am. B* **7**, 2006 (1990).

[121] K. Sakai. *Terahertz optoelectronics, Topics Appl. Phys.* Springer, Berlin (2005).

[122] G. Kozlov and A. Volkov. *Millimeter and Submillimeter Wave Spectroscopy of Solids, Chapter: Coherent Source Submillimeter Wave Spectroscopy*, vol. 74. Springer-Verlag Berlin Heidelberg (1998).

[123] B. Gompf, M. Gerull, T. Müller, and M. Dressel. THz-micro-spectroscopy with backward-wave oscillators. *Infrared Phys. Techn.* **49**, 128 (2006).

[124] M. Bass, P. A. Franken, J. F. Ward, and G. Weinreich. Optical rectification. *Phys. Rev. Lett.* **9**, 446 (1962).

[125] A. Nahata, A. S. Weling, and T. F. Heinz. A wideband coherent terahertz spectroscopy system using optical rectification and electro-optic sampling. *Appl. Phys. Lett.* **69**, 2321 (1996).

[126] L. Xu, X. C. Zhang, and D. H. Auston. Terahertz beam generation by femtosecond optical pulses in electrooptic materials. *Appl. Phys. Lett.* **61**, 1784 (1992).

[127] K. Reimann, R. P. Smith, A. M. Weiner, T. Elsaesser, and M. Woerner. Direct field-resolved detection of terahertz transients with amplitudes of megavolts per centimeter. *Opt. Lett.* **28**, 471 (2003).

[128] X.-C. Zhang, X. F. Ma, Y. Jin, T.-M. Lu, E. P. Boden, P. D. Phelps, K. R. Stewart, and C. P. Yakymyshyn. Terahertz optical rectification from a nonlinear organic crystal. *Appl. Phys. Lett.* **61**, 3080 (1992).

[129] H. Hashimoto, H. Takahashi, T. Yamada, K. Kuroyanagi, and T. Kobayashi. Characteristics of the terahertz radiation from single crystals of N-substituted 2-methyl-4-nitroaniline. *J. Phys.: Cond. Matt.* **13**, 529 (2001).

[130] X.-C. Zhang, Y. Jin, K. Yang, and L. J. Schowalter. Resonant nonlinear susceptibility near the GaAs band gap. *Phys. Rev. Lett.* **69**, 2303 (1992).

[131] D. H. Auston, K. P. Cheung, J. A. Valdmanis, and D. A. Kleinman. Cherenkov radiation from femtosecond optical pulses in electro-optic media. *Phys. Rev. Lett.* **53**, 1555 (1984).

[132] AB Millimetre. `http://www.abmillimetre.com`.

[133] K. A. McIntosh, E. R. Brown, K. B. Nichols, O. B. McMahon, W. F. DiNatale, and T. M. Lyszczarz. Terahertz photomixing with diode lasers in low-temperature-grown GaAs. *Appl. Phys. Lett.* **67**, 3844 (1995).

[134] R. Köhler, A. Tredicucci, F. Beltram, H. E. Beere, E. H. Linfield, A. G. Davies, D. A. Ritchie, R. C. Iotti, and F. Rossi. Terahertz semiconductor-heterostructure laser. *Nature* **417**, 156 (2002).

[135] K. Kawase, J. Shikata, and H. Ito. Terahertz wave parametric source. *J. Phys. D: Appl. Phys.* **35**, R1 (2002).

[136] K. Kawase, H. Minamide, K. Imai, J. Shikata, and H. Ito. Injection-seeded terahertz-wave parametric generator with wide tunability. *Appl. Phys. Lett.* **80**, 195 (2002).

[137] L. Ozyuzer, A. E. Koshelev, C. Kurter, N. Gopalsami, Q. Li, M. Tachiki, K. Kadowaki, T. Yamamoto, H. Minami, H. Yamaguchi, T. Tachiki, K. E. Gray, W.-K. Kwok, and U. Welp. Emission of Coherent THz Radiation from Superconductors. *Science* **318**, 1291 (2007).

[138] E. J. Reed, M. R. Armstrong, K. Kim, M. Solja, R. Gee, J. H. Glownia, and J. D. Joannopoulos. Terahertz radiation from shocked materials. *Mater. Today* **10**, 44 (2007).

[139] M. Abo-Bakr, J. Feikes, K. Holldack, P. Kuske, W. B. Peatman, U. Schade, G.Wüstefeld, and H.-W. Hübers. Brilliant, Coherent Far-Infrared (THz) Synchrotron Radiation. *Phys. Rev. Lett.* **90**, 09 4801 (2003).

[140] G. L. Carr, M. C. Martin, W. R. McKinney, K. Jordan, G. R. Neil, and G. P. Williams. High-power terahertz radiation from relativistic electrons. *Nature* **420**, 153 (2002).

[141] F. E. Doany, D. Grischkowsky, and C.-C. Chi. Carrier Lifetime versus Ion-Implantation Dose in Silicon on Sapphire. *Appl. Phys. Lett.* **50**, 460 (1987).

[142] H. Němec, A. Pashkin, P. Kužel, M. Khazan, S. Schnüll, and I. Wilke. Carrier dynamics in low-temperature grown GaAs studied by terahertz emission spectroscopy. *J. Appl. Phys.* **90**, 1303 (2001).

[143] K. Liu, A. Krotkus, K. B. J. Xu, and X.-C. Zhang. Terahertz radiation from n-type GaAs with Be-doped low-temperature-grown GaAs surface layers. *J. Appl. Phys.* **94**, 3651 (2003).

[144] M. V. Exter, C. Fattinger, and D. Grischkowsky. High-brightness terahertz beams characterized with an ultrafast detector. *Appl. Phys. Lett.* **55**, 337 (1989).

[145] J. T. Darrow, B. B. Hu, X.-C. Zhang, and D. H. Auston. Subpicosecond electromagnetic pulses from large-aperture photoconducting antennas. *Opt. Lett.* **15**, 323 (1990).

[146] B. B. Hu, J. T. Darrow, X.-C. Zhang, D. H. Auston, and P. R. Smith. Optically steerable photoconducting antennas. *Appl. Phys. Lett.* **56**, 886 (1990).

[147] P. K. Benicewicz and A. J. Taylor. Scaling of terahertz radiation from large-aperture biased InP photoconductors. *Opt. Lett.* **18**, 1332 (1993).

[148] A. Dreyhaupt, S. Winnerl, T. Dekorsy, and M. Helm. High-intensity terahertz radiation from a microstructured large-area photoconductor. *Appl. Phys. Lett.* **86**, 12 1114 (2005).

[149] X.-C. Zhang, B. B. Hu, J. T. Darrow, and D. H. Auston. Generation of femtosecond electromagnetic pulses from semiconductor surfaces. *Appl. Phys. Lett.* **56**, 1011 (1990).

[150] X.-C. Zhang and D. H. Auston. Optoelectronic measurement of semiconductor surfaces and interfaces with femtosecond optics. *J. Appl. Phys.* **71**, 326 (1992).

[151] S. Izumida, S. Ono, Z. Liu, H. Ohtake, and N. Sarukura. Spectrum control of THz radiation from InAs in a magnetic field by duration and frequency chirp of the excitation pulses. *Appl. Phys. Lett.* **75**, 451 (1999).

[152] G. Grüner. *Millimeter and Submillimeter Wave Spectroscopy of Solids.* Springer-Verlag, Berlin, Heidelberg, New York (1998).

[153] F. C. A. Pockels. *Abhand. d. Ges. d. Wiss. zu Göttingen, Math. Phys. Klasse* **39**, 1 (1893).

[154] H. Němec. *Time-resolved terahertz spectroscopy applied to the investigation of magnetic materials and photonic structures.* Ph.D. thesis, Charles university in Prague (2006).

[155] Q. Wu and X.-C. Zhang. 7 terahertz broadband GaP electro-optic sensor. *Appl. Phys. Lett.* **70**, 1784 (1997).

[156] P. Y. Han, M. Tani, and X.-C. Zhang. Use of the organic crystal DAST for terahertz beam application. *Optics Letters* **25**, 675 (2000).

[157] P. U. Jepsen, C. Winnewisser, M. Schall, V. Schyja, S. R. Keiding, and H. Helm. Detection of THz pulses by phase retardation in lithium tantalate. *Phys. Rev. E* **53**, R3052 (1996).

[158] C. Winnewisser, P. U. Jepsen, M. Schall, V. Schyja, and H. Helm. Electro-optic detection of THz radiation in $LiTaO_3$, $LiNbO_3$ and ZnTe. *Appl. Phys. Lett.* **70**, 3069 (1997).

[159] A. Y. Elezzabi and M. R. Freeman. Ultrafast magneto-optic sampling of picosecond current pulses. *Appl. Phys. Lett.* **68**, 3546 (1996).

[160] J. A. Riordan, F. G. Sun, Z. G. Lu, and X.-C. Zhang. Free-space transient magneto-optic sampling. *Appl. Phys. Lett.* **71**, 1452 (1997).

[161] A. Schneider, I. Biaggio, and P. Günter. Terahertz-induced lensing and its use for the detection of terahertz pulses in a birefringent crystal. *Appl. Phys. Lett.* **84**, 2229 (2004).

[162] Y.-S. Lee. *Principles of Terahertz Science and Technology.* Springer, New York (2009).

[163] J. F. Vetelino, S. S. Mitra, and K. V. Namjoshi. Lattice Dynamics of ZnTe: Phonon Dispersion, Multiphonon Infrared Spectrum, Mode Grüneisen Parameters, and Thermal Expansion. *Phys. Rev. B* **2**, 967 (1970).

[164] H. J. Bakker, G. C. Cho, H. Kurz, Q. Wu, and X.-C. Zhang. Distortion of terahertz pulses in electro-optic sampling. *J. Opt. Soc. Am. B* **15**, 1795 (1998).

[165] Q. Wu, M. Litz, and X.-C. Zhang. Broadband detection capability of ZnTe electro-optic field detectors. *Appl. Phys. Lett.* **68**, 2924 (1996).

[166] L. Duvillaret, F. Garet, and J.-L. Coutaz. A reliable method for extraction of material parameters in terahertz time-domain spectroscopy. *IEEE J. Sel. Top. Quant.* **2**, 739 (1996).

[167] P. Kužel and J. Petzelt. Time-resolved terahertz transmission spectroscopy of dielectrics. *Ferroelectrics* **239**, 949 (2000).

[168] A. Pashkin, E. Buixaderas, P. Kužel, M.-H. Liang, C.-T. Hu, and I.-N. Lin. THz transmission spectroscopy applied to dielectrics and microwave ceramics. *Ferroelectrics* **254**, 113 (2001).

[169] J. Petzelt, P. Kužel, I. Rychetský, A. Pashkin, and T. Ostapchuk. Dielectric Response of Soft Modes in Ferroelectric Thin Films. *Ferroelectrics* **288**, 169 (2003).

[170] A. Pashkin, M. Kempa, H. Němec, F. Kadlec, and P. Kužel. Phase-sensitive time-domain terahertz reflection spectroscopy. *Rev. Sci. Instrum.* **74**, 4711 (2003).

[171] P. Brüesch. *Phonons: Theory and Experiments II.* Springer-Verlag, Berlin, Heidelberg, New York, London, Paris, Tokyo (1986).

[172] F. Gervais. *Infrared and Millimetre Waves.* vol. 8. Academic Press, New York (1983).

[173] J. H. Barrett. Dielectric constant in perovskite type crystals. *Phys. Rev.* **86**, 118 (1952).

[174] R. G. Geyer, B. Riddle, J. Krupka, and L. A. Boatner. Microwave dielectric properties of single-crystal quantum paraelectrics $KTaO_3$ and $SrTiO_3$ at cryogenic temperatures. *J. Appl. Phys.* **97**, 10 4111 (2005).

[175] G. A. Samara. The relaxational properties of compositionally disordered ABO_3 perovskites. *J. Phys.: Condens. Matter* **15**, R367 (2003).

[176] H. Uwe and T. Sakudo. Stress-induced ferroelectricity and soft phonon modes in $SrTiO_3$. *Phys. Rev. B* **13**, 271 (1976).

[177] Y. Ichikawa, M. Nagai, and K. Tanaka. Direct observation of the soft-mode dispersion in the incipient ferroelectric $KTaO_3$. *Phys. Rev. B* **71**, 09 2106 (2005).

[178] Z. X. Chen, X. L. Zhang, and L. E. Cross. Low-Temperature Dielectric Properties of Ceramic Potassium Tantalate ($KTaO_3$). *J. Am. Ceram. Soc.* **66**, 511 (1983).

[179] S. Glinšek, B. Malič, T. Rojac, C. Filipič, B. Budič, and M. Kosec. $KTaO_3$ Ceramics Prepared by the Mechanochemically Activated Solid-State Synthesis. *J. Am. Ceram. Soc.* **94**, 1368 (2011).

[180] A. Tkach, P. M. Vilarinho, and A. Almeida. Role of initial potassium excess on the properties of potassium tantalate ceramics. *J. Eur. Ceram. Soc.* **31**, 2303 (2011).

[181] J. Petzelt. Dielectric Grain-Size Effect in High-Permittivity Ceramics. *Ferroelectrics* **400**, 117 (2010).

[182] J. Petzelt, T. Ostapchuk, I. Gregora, D. Nuzhnyy, I. Rychetsky, K. Maca, and Z. Shen. Grain Boundary and Size Effect on the Dielectric, Infrared and Raman Response of $SrTiO_3$ Nanograin Ceramics. *Ferroelectrics* **363**, 227 (2008).

[183] T. Sakudo and H. Unoki. Dielectric Properties of $SrTiO_3$ at Low Temperatures. *Phys. Rev. Lett.* **26**, 851 (1971).

[184] S. Glinšek, D. Nuzhnyy, J. Petzelt, B. Malič, S. Kamba, V. Bovtun, M. Kempa, V. Skoromets, P. Kužel, I. Gregora, and M. Kosec. Lattice dynamics and broad-band dielectric properties of the $KTaO_3$ ceramics. *J. Appl. Phys.* **111**, 10 4101 (2012).

[185] R. C. Miller and W. G. Spitzer. Far Infrared Dielectric Dispersion in $KTaO_3$. *Phys. Rev.* **129**, 94 (1963).

[186] C. H. Perry and T. F. McNelly. Ferroelectric "Soft" Mode in $KTaO_3$. *Phys. Rev.* **154**, 456 (1967).

[187] H. Vogt. Refined treatment of the model of linearly coupled anharmonic oscillators and its application to the temperature dependence of the zone-center soft-mode frequencies of $KTaO_3$ and $SrTiO_3$. *Phys. Rev. B* **51**, 8046 (1995).

[188] I. M. Buzin, I. V. Ivanov, and V. A. Chistyaev. Mode interaction and dielectric losses in potassium tantalate. *Fiz. Tverd. Tela* **22**, 2848 (1980).

[189] V. Belokopytov, I. V. Ivanov, S. I. Katanov, N. N. Moiseev, and P. P. Syrnikov. Dielectric losses of potassium tantalate crystals at 0.5-115 GHz frequencies. *Fiz. Tverd. Tela* **24**, 1865 (1982).

[190] H. Vogt and H. Uwe. Hyper-Raman scattering from the incipient ferroelectric $KTaO_3$. *Phys. Rev. B* **29**, 1030 (1984).

[191] P. A. Fleury and J. M. Worlock. Electric-Field-Induced Raman Scattering in $SrTiO_3$ and $KTaO_3$. *Phys. Rev.* **174**, 613 (1968).

[192] R. P. Lowndes and A. Rastogi. Stabilization of the paraelectric phase of $KTaO_3$ and $SrTiO_3$ by strong quartic anharmonicity. *J. Phys. C: Solid State Phys.* **16**, 932 (1973).

[193] H.-M. Christen, J. Mannhart, E. J. Williams, and C. Gerber. Dielectric properties of sputtered $SrTiO_3$ films. *Phys. Rev. B* **49**, 12 095 (1994).

[194] J. Dec, W. Kleemann, and B. Westwanski. Scaling behaviour of strontium titanate. *J. Phys. Condens. Matter* **11**, L379 (1999).

[195] A. Eriksson, A. Deleniv, and S. Gevorgian. Orientation and direct current field dependent dielectric properties of bulk single crystal $SrTiO_3$ at microwave frequencies. *J. Appl. Phys.* **93**, 2848 (2012).

[196] C. Kadlec, F. Kadlec, H. Němec, P. Kužel, J. Schubert, and G. Panaitov. High tunability of the soft mode in strained $SrTiO_3/DyScO_3$ multilayers. *J. Phys.:Cond. Matter.* **21**, 11 5902 (2009).

[197] F. Hecht, FreeFem++, Third Edition, Version 3.13. `http://www.freefem.org//ff++`.

[198] A. Yamanaka, M. Kataoka, Y. Inaba, K. Inoue, B. Hehlen, and E. Courtens. Evidence for competing orderings in strontium titanate from hyper-Raman scattering spectroscopy. *Europhys. Lett.* **50**, 688 (2000).

[199] V. Müller, M. Rasp, G. Stefanic, J. Ba, S. Günther, J. Rathousky, M. Niederberger, and D. Fattakhova-Rohlfing. Highly Conducting Nanosized Monodispersed Antimony-Doped Tin Oxide Particles Synthesized via Nonaqueous Sol-Gel Procedure. *Chem. Mater.* **21**, 5229 (2009).

[200] J. Hemberger, P. Lunkenheimer, R. Viana, R. Böhmer, and A. Loidl. Electric-field-dependent dielectric constant and nonlinear susceptibility in $SrTiO_3$. *Phys. Rev. B* **52**, 13 159 (1995).

[201] J. N. Winn, Y. Fink, S. Fan, and J. D. Joannopoulos. Omnidirectional reflection from a one-dimensional photonic crystal. *Opt. Lett.* **23**, 1573 (1998).

[202] N. I. Santha, M. T. Sebastian, P. Mohanan, N. M. Alford, K. Sarma, R. C. Pullar, S. Kamba, A. Pashkin, P. Samukhina, and J. Petzelt. Effect of Doping on the Dielectric Properties of Cerium Oxide in the Microwave and Far-Infrared Frequency Range. *J. Am. Ceram. Soc.* **87**, 1233 (2004).

[203] R. Jacobsson. *Progress in Optics*. Chap. 5. North-Holland (1965).

[204] K. Aso. Residual Stress in Damaged $SrTiO_3$ Single Crystals. *Jpn. J. Appl. Phys.* **15**, 1243 (1976).

[205] A. F. Devonshire. Theory of ferroelectrics. *Phil. Mag. Suppl.* **3**, 85 (1954).

[206] N. A. Pertsev, A. G. Zembilgotov, and A. K. Tagantsev. Effect of mechanical boundary conditions on phase diagrams of epitaxial ferroelectric thin films. *Phys. Rev. Lett.* **80**, 1988 (1998).

[207] P. Irvin, J. Levy, J. H. Haeni, and D. G. Schlom. Localized microwave resonances in strained $SrTiO_3$ thin films. *Appl. Phys. Lett.* **88**, 04 2902 (2006).

[208] W. Chang, J. A. Bellotti, S. W. Kirchoefer, and J. M. Pond. Strain tensor effects on $SrTiO_3$ incipient ferroelectric phase transition. *J. Electroceram* **17**, 487 (2006).

[209] A. Vasudevarao, A. Kumar, L. Tian, J. H. Haeni, Y. L. Li, C.-J. Eklund, Q. X. Jia, R. Uecker, P. Reiche, K. M. Rabe, L. Q. Chen, D. G. Schlom, and V. Gopalan. Multiferroic Domain Dynamics in Strained Strontium Titanate. *Phys. Rev. Lett.* **97**, 25 7602 (2006).

[210] T. Heeg, J. Schubert, C. Buchal, E. Cicerrella, J. Freeouf, W. Tian, Y. Jia, and D. Schlom. Growth and properties of epitaxial rare-earth scandate thin films. *Appl. Phys. A* **83**, 103 (2006).

[211] R. Wördenweber, E. Hollmann, R. Kutzner, and J. Schubert. Induced ferroelectricity in strained epitaxial $SrTiO_3$ films on various substrates. *J. Appl. Phys.* **102**, 04 4119 (2007).

[212] Z. Y. Zhai, X. S. Wu, H. L. Cai, X. M. Lu, J. H. Hao, J. Gao, W. S. Tan, Q. J. Jia, H. H. Wang, and Y. Z. Wang. Dislocation density and strain distribution in $SrTiO_3$ film grown on (110) $DyScO_3$ substrate. *J. Phys. D: Appl. Phys.* **42**, 10 5307 (2009).

[213] L. Beckers, J. Schubert, W. Zander, J. Ziesmann, A. Eckau, P. Leinenbach, and C. Buchal. Structural and optical characterization of epitaxial waveguiding $BaTiO_3$ thin films on MgO. *J. Appl. Phys.* **83**, 3305 (1998).

[214] C. Kadlec, V. Skoromets, F. Kadlec, H. Němec, J. Hlinka, J. Schubert, G. Panaitov, and P. Kužel. Temperature and electric field tuning of the ferroelectric soft mode in a strained $SrTiO_3/DyScO_3$ heterostructure. *Phys. Rev. B* **80**, 17 4116 (2009).

[215] C. Kadlec, F. Kadlec, H. Němec, P. Kužel, J. Schubert, and G. Panaitov. High tunability of the soft mode in strained $SrTiO_3/DyScO_3$ multilayers. *J. Phys.: Condens. Matter* **21**, 11 5902 (2009).

[216] P. Kužel, C. Kadlec, F. Kadlec, J. Schubert, and G. Panaitov. Field-induced soft mode hardening in $SrTiO_3/DyScO_3$ multilayers. *Appl. Phys. Lett.* **93**, 05 2910 (2008).

[217] A. S. Barker and J. J. Hopfield. Coupled-Optical-Phonon-Mode Theory of the Infrared Dispersion in $BaTiO_3$, $SrTiO_3$ and $KTaO_3$. *Phys. Rev.* **135**, A1732 (1964).

[218] Y. Girshberg and Y. Yacoby. Ferroelectric phase transitions in perovskites with off-center ion displacements. *Solid State Commun.* **103**, 425 (1997).

[219] A. Bussmann-Holder, H. Büttner, and A. R. Bishop. Polar-soft-mode-driven structural phase transition in $SrTiO_3$. *Phys. Rev. Lett.* **99**, 16 7603 (2007).

[220] J. Hlinka, T. Ostapchuk, D. Nuzhnyy, J. Petzelt, P. Kužel, C. Kadlec, P. Vaněk, I. Ponomareva, and L. Bellaiche. Coexistence of the phonon and relaxation soft modes in the terahertz dielectric response of tetragonal $BaTiO_3$. *Phys. Rev. Lett.* **101**, 16 7402 (2007).

[221] I. Ponomareva, L. Bellaiche, T. Ostapchuk, J. Hlinka, and J. Petzelt. Terahertz dielectric response of cubic $BaTiO_3$. *Phys. Rev. B* **77**, 01 2102 (2008).

[222] J. Weerasinghe, L. Bellaiche, T. Ostapchuk, P. Kužel, C. Kadlec, S. Lisenkov, I. Ponomareva, and J. Hlinka. Emergence of central mode in the paraelectric phase of ferroelectric perovskites. *MRS Communications* **3**, 41 (2013).

[223] P. Kužel. Oral communication. Unpublished.

[224] D. Fuchs, C. W. Schneider, R. Schneider, and H. Rietschel. High dielectric constant and tunability of epitaxial $SrTiO_3$ thin film capacitors. *J. Appl. Phys.* **85**, 7362 (1999).

[225] W. J. Merz. Double hysteresis loop of $BaTiO_3$ at the Curie point. *Phys. Rev.* **91**, 513 (1953).

[226] C.-H. Lee, V. Skoromets, S. Lei, M. D. Biegalski, M. Bernhagen, R. Uecker, X. Xi, V. Gopalan, X. Martí, S. Kamba, P. Kužel, and D. G. Schlom. Effect of stoichiometry on the dielectric properties and soft mode behavior of strained epitaxial $SrTiO_3$ thin films on $DyScO_3$ substrates. *Appl. Phys. Lett.* **102**, 08 2905 (2013).

[227] M. D. Biegalski, Y. Jia, D. G. Schlom, S. Trolier-McKinstry, S. K. Streiffer, V. Sherman, R. Uecker, and P. Reiche. Relaxor ferroelectricity in strained epitaxial $SrTiO_3$ thin films on $DyScO_3$ substrates. *Appl. Phys. Lett.* **88**, 19 2907 (2006).

[228] M. D. Biegalski, E. Vlahos, G. Sheng, Y. L. Li, M. Bernhagen, P. Reiche, R. Uecker, S. K. Streiffer, L. Q. Chen, V. Gopalan, D. G. Schlom, and S. Trolier-McKinstry. Influence of anisotropic strain on the dielectric and ferroelectric properties of $SrTiO_3$ thin films on $DyScO_3$ substrates. *Phys. Rev. B* **79**, 22 4117 (2009).

[229] H. W. Jang, A. Kumar, S. Denev, M. D. Biegalski, P. Maksymovych, C. Bark, C. T. Nelson, C. M. Folkman, S. H. Baek, N. Balke, C. M. Brooks, D. A. Tenne, D. G. Schlom, L. Q. Chen, X. Q. Pan, S. Kalinin, V. Gopalan, and C. B. Eom. Ferroelectricity in strain-free $SrTiO_3$ thin films. *Phys. Rev. Lett.* **104**, 19 7601 (2010).

[230] C. M. Brooks, L. F. Kourkoutis, T. Heeg, J. Schubert, D. A. Muller, and D. G. Schlom. Growth of homoepitaxial $SrTiO_3$ thin films by molecular-beam epitaxy. *Appl. Phys. Lett.* **94**, 16 2905 (2009).

[231] M. D. Biegalski, D. D. Fong, J. A. Eastman, P. H. Fuoss, S. K. Streiffer, T. Heeg, J. Schubert, W. Tian, C. T. Nelson, X. Q. Pan, M. E. Hawley, M. Bernhagen, P. Reiche, R. Uecker, S. Trolier-McKinstry, and D. G. Schlom. Critical thickness of high structural quality $SrTiO_3$ films grown on orthorhombic (101) $DyScO_3$. *J. Appl. Phys.* **104**, 11 4109 (2008).

[232] Y. L. Li, S. Choudhury, J. H. Haeni, M. D. Biegalski, A. Vasudevarao, A. Sharan, H. Z. Ma, J. Levy, V. Gopalan, S. Trolier-McKinstry, D. G. Schlom, Q. X. Jia, and

L. Q. Chen. Phase transitions and domain structures in strained pseudocubic (100) $SrTiO_3$ thin films. *Phys. Rev. B* **73**, 18 4112 (2006).

[233] R. J. D. Tilley. An electron microscope study of perovskite-related oxides in the Sr-Ti-O system. *J. Solid State Chem.* **21**, 293 (1977).

[234] V. Bovtun, S. Veljko, S. Kamba, J. Petzelt, S. Vakhrushev, Y. Yakymenko, K. Brinkman, and N. Setter. Broad-band dielectric response of $PbMg_{1/3}Nb_{2/3}O_3$ relaxor ferroelectrics: Single crystals, ceramics and thin films. *J. Eur. Ceram. Soc.* **26**, 2867 (2006).

[235] V. Skoromets, S. Glinšek, V. Bovtun, M. Kempa, J. Petzelt, S. Kamba, B. Malič, M. Kosec, and P. Kužel. Ferroelectric phase transition in polycrystalline $KTaO_3$ thin film revealed by terahertz spectroscopy. *Appl. Phys. Lett.* **99**, 05 2908 (2011).

[236] V. Bovtun, V. Pashkov, M. Kempa, S. Kamba, A. Eremenko, V. Molchanov, Y. Poplavko, Y. Yakymenko, J. H. Lee, and D. G. Schlom. An electrode-free method of characterizing the microwave dielectric properties of high-permittivity thin films. *J. Appl. Phys.* **109**, 02 4106 (2011).

[237] M. Tyunina, J. Narkilahti, M. Plekh, R. Oja, R. M. Nieminen, A. Dejneka, and V. Trepakov. Evidence for strain-induced ferroelectric order in epitaxial thin-film $KTaO_3$. *Phys. Rev. Lett.* **104**, 22 7601 (2010).

[238] Železný, J. Buršík, and P. Vaněk. Preparation and infrared characterization of potassium tantalate thin films. *J. Eur. Ceram. Soc.* **25**, 2155 (2005).

[239] H. Vogt. Hyper-Rayleigh scattering from the bulk of nominally pure $KTaO_3$. *Phys. Rev. B* **41**, 1184 (2010).

[240] T. Ostapchuk, J. Petzelt, V. Železný, A. Pashkin, J. Pokorný, I. Drbohlav, R. Kužel, D. Rafaja, B. P. Gorshunov, M. Dressel, C. Ohly, S. Hoffmann-Eifert, and R. Waser. Origin of soft-mode stiffening and reduced dielectric response in $SrTiO_3$ thin films. *Phys. Rev. B* **66**, 23 5406 (2002).

[241] D. Nuzhnyy, J. Petzelt, S. Kamba, P. Kužel, C. Kadlec, V. Bovtun, M. Kempa, J. Schubert, C. M. Brooks, and D. G. Schlom. Soft mode behavior in $SrTiO_3/DyScO_3$ thin films: Evidence of ferroelectric and antiferrodistortive phase transitions. *Appl. Phys. Lett.* **95**, 23 2902 (2009).

[242] I. A. Akimov, A. A. Sirenko, A. M. Clark, J.-H. Hao, and X. X. Xi. Electric-Field-Induced Soft-Mode Hardening in $SrTiO_3$ Films. *Phys. Rev. Lett.* **84**, 4625 (2000).

[243] J. M. Worlock and P. A. Fleury. Electric Field Dependence of Optical-Phonon Frequencies. *Phys. Rev. Lett.* **19**, 1176 (1967).

[244] W. Zhong, R. King-Smith, and D. Vanderbilt. Giant LO-TO Splittings in Perovskite Ferroelectrics. *Phys. Rev. Lett.* **72**, 3618 (1994).

[245] J. Weerasinghe, D. Wang, and L. Bellaiche. Effect of the central mode on the dielectric tunability of ferroelectrics near room temperature: A first-principle-based study. To be unpublished.

List of acronyms

AFD	Antiferrodistortive
BST	$Ba_xSr_{1-x}TiO_3$, $(Ba,Sr)TiO_3$ − barium-strontium titanate
CM	Central mode
DSO	$DyScO_3$ − dysprosium scandate
FIR	Far infrared
FTIR	Fourier transform infrared
IR	Infrared
KTO	$KTaO_3$ − potassium tantalate
MSM	Metal-semiconductor-metal
MW	Microwave
PC	Photonic crystal
PT	Phase transition
RF	Radio frequency
SM	Soft mode
STO	$SrTiO_3$ − strontium titanate
TDTS	Time-domain terahertz spectroscopy
THz	Terahertz
TO	Transverse optical
1D	One-dimensional